CUKUROVA UNIVERSITY
INSTITUTE OF NATURAL AND APPLIED SCIENCES

PhD THESIS

Serdal DAMARSEÇKİN

SEARCH FOR NEW PARTICLES DECAYING TO DIJET AT $\sqrt{s}$ = 13 TeV PROTON-PROTON COLLISIONS WITH DATA SCOUTING TECHNIQUE AT CMS

DEPARTMENT OF PHYSICS

ADANA-2018

CUKUROVA UNIVERSITY
INSTITUTE OF NATURAL AND APPLIED SCIENCES

SEARCH FOR NEW PARTICLES DECAYING TO DIJET AT $\sqrt{s} = 13$ TeV PROTON-PROTON COLLISIONS WITH DATA SCOUTING TECHNIQUE AT CMS

Serdal DAMARSEÇKİN

PhD THESIS

DEPARTMENT OF PHYSICS

We certify that the thesis titled above was reviewed and approved for the award of degree of the Doctor of Philosophy by the board of jury on 02/03/2018.

………………..............	..................................…………	…..…………………
Prof.Dr. İsa DUMANOĞLU SUPERVISOR	Prof.Dr. Aysel KAYIŞ TOPAKSU MEMBER	Prof.Dr. Sefa ERTÜRK MEMBER
...………………............	……….....………………………	
Prof.Dr. Eda EŞKUT MEMBER	Asst.Prof.Dr. Evrim Ersin KANGAL MEMBER	

This PhD Thesis is performed in Department of Physics of Institute of Natural and Applied Sciences of Çukurova University.
Registration Number:

Prof. Dr. Mustafa GÖK
Director
Institute of Basic and Applied Sciences

This Study was supported by Çukurova University Scientific Research Fund.
Project Number : FDK-2015-2655

Not: The usage of the presented specific declarations, tables, figures and photographs either in this thesis or in any other reference without citation is subject to "The Law of Arts and Intellectual Products" numbered 5846 of Turkish Republic.

ABSTRACT

PhD THESIS

SEARCH FOR NEW PARTICLES DECAYING TO DIJET AT $\sqrt{s}$ = 13 TeV PROTON-PROTON COLLISIONS WITH DATA SCOUTING TECHNIQUE AT CMS

Serdal DAMARSEÇKİN

ÇUKUROVA UNIVERSITY
INSTITUTE OF NATURAL AND APPLIED SCIENCES
DEPARTMENT OF PHYSICS

Supervisor : Prof.Dr. İsa DUMANOĞLU
Co-Supervisor : Assoc.Prof.Dr. Sertaç ÖZTÜRK
Year: 2018, Page: 170
Jury : Prof.Dr. İsa DUMANOĞLU
: Prof.Dr. Aysel KAYIŞ TOPAKSU
: Prof.Dr. Sefa ERTÜRK
: Prof.Dr. Eda EŞKUT
: Asst.Prof.Dr. Evrim Ersin KANGAL

A search for narrow dijet resonances and a measurement of the dijet invariant mass spectra are presented in this thesis. The dijet mass data are compared to the QCD predictions from PHYTIA. The data from proton-proton collisions at center-of-mass energy of 13 TeV corresponding to an integrated luminosity of 1.9 fb^{-1}, recorded with the CMS detector at the Large Hadron Collider (LHC) in 2015. It is required that the pseudorapidity separation of the two leading jets are measured with the CMS detector to satisfy $|\Delta\eta_{jj}|$ < 1.3 with each jet inside the region η_{jj} < 2.5. No significant excesses are observed in data. Also, since there is no evidence for dijet resonances, the upper limits on the resonance cross section at 95% Confidence Level are obtained for gluon-gluon, quark-gluon and quark-quark.

Keywords: LHC, CMS, Jets, QCD, Excited Quark, Dijet, Resonance Mass

ÖZ

DOKTORA TEZİ

CMS'DE VERİ TARAMA TEKNİĞİ İLE $\sqrt{s}$ = 13 TeV PROTON-PROTON ÇARPIŞMALARINDA İKİ-JET'E BOZUNAN YENİ PARÇACIKLARIN ARAŞTIRILMASI

Serdal DAMARSEÇKİN

ÇUKUROVA ÜNİVERSİTESİ
FEN BİLİMLERİ ENSTİTÜSÜ
FİZİK ANABİLİM DALI

Danışman	: Prof.Dr. İsa DUMANOĞLU
İkinci Danışman	: Doç.Dr. Sertaç ÖZTÜRK
	Yıl: 2018, Sayfa: 170
Jüri	: Prof.Dr. İsa DUMANOĞLU
	: Prof.Dr. Aysel KAYIŞ TOPAKSU
	: Prof.Dr. Sefa ERTÜRK
	: Prof.Dr. Eda EŞKUT
	: Yrd. Doç. Dr. Evrim Ersin KANGAL

Bu tezde iki-jet değişmez kütle spektrumu ölçümü ve dar iki jet rezonansı için araştırmalar sunulmuştur. İki-jet kütle verileri PYTHIA'dan gelen QCD öngörüsü ile kıyaslanmıştır. 1.9 fb^{-1}' lık toplam ışınlığa karşılık gelen ve kütle merkezi enerjisi 13 TeV olan proton-proton çarpışmasından gelen veri, 2015 yılında Büyük Hadron Çarpıştırıcısı'nda CMS detektörü ile alınmıştır. CMS detektörü tarafından ölçülmekte olan iki ana jet arasındaki pseudorapidite farkının, her bir jetin η_{jj} < 2.5 bölgesinde bulunması kaydıyla, $|\Delta\eta_{jj}|$ < 1.3 olması gerekmektedir. Verilerde belirgin bir aşırılık görülmemektedir. Ayrıca iki-jet resonanslarının varlığına dair herhangi bir kanıt olmadığından gluon-gluon, quark-quark ve quark-gluon için % 95 güvenirlilik düzeyindeki rezonans tesir kesiti için üst limitler elde edilmiştir.

Anahtar Kelimeler: BHÇ, CMS, Jetler, KRD, Uyarılmış Kuark, İki Jet, Resonans Kütlesi.

EXTENDED SUMMARY

High Energy Physics investigate what is the main structure of the matter and how these fundamental particles interact with each other. Many experimental and theoretical studies have been conducted to find answers such questions and these long term studies have led to the formation of a basic theory, which is also called as “Standard Model (SM)”, which have been successfully tested and aims to explain the properties and interactions of the building blocks of the matter.

High Energy Physics is the popular science of this century, which aims to understand the characteristics of the forces governing the interactions of the matter and the energy, the nature of space and time, the properties and the interactions of the subatomic particles. It is not possible to observe subatomic particles by using the low energies. Therefore, high energies are needed to investigate the elementary particles and their interactions. Particle colliders are needed for the collision of the particles at high energies and detectors are needed to understand the properties of the particles.

The Large Hadron Collider (LHC) is the world most powerful and the largest particle accelerator, based at the European particle physics laboratory CERN, built in between Switzerland and France borders. The LHC offers the opportunity to regenerate the conditions existed within a billionth of a second after Big Bang. These conditions are recreated by colliding beams of protons or lead ions at the velocities very close to the speed of light.

The SM, which has consistent estimates for all experimental data, is not a perfect theory, like all other theories, despite it has been developed to describe the basic particles and the interactions between them. Since, there are some questions that this model cannot answer such as dark matter, dark energy, neutrino masses, matter and anti-matter asymmetry. In addition, it does not include general relativity. In order to find answers to these questions, new physics investigations beyond the SM tested by LHC in CERN is suggested. There are theories trying to address these questions and they predicted the existence of very short-lived particles, generally called as “resonance”. In this thesis study, the new particles decaying to two-jets and predicted by the theories beyond the SM were investigated. These new particles were searched in dijet mass distribution. If a dijet resonance exists, it is expected to emerge as a bump in this dijet mass spectrum.

Our study is model-independent due to not being used or depent on any theoretical model. Additionally, the search is sensitive to any resonance creating two-jet, and the analysis technique is robust and simple.

The LHC experiment was restarted, after a long shutdown period between the end of 2012 and the summer of 2015. While the protons were collided with 7 TeV center of mass energy in 2012, collision with about twice energy (13 TeV) was achieved in 2015. Especially for high mass resonances, we will see that this energy increase corresponds much larger cross sections.

The results obtained from the data with a total luminosity of 1.9 fb^{-1} and collected in the CMS experiments in 2015 are presented.

This thesis presents a brief introduction to the SM reminding the elements of Quantum Chromodynamics and its effects on experimental measurements of hadronic interactions. The physics elements of proton-proton interactions in hadron colliders are also introduced.

As it is mentioned above, there are several models such as excited quark, E_6 diquark, axigluon, Randall-Sundrum graviton, string resonance, etc. that predict dijet resonances in the accessible mass region for LHC collisions. The results of CMS dijet analysis presented in this thesis are compared with the expectations of some theoretical models.

A section of the study is devoted to the definition of the detector. The LHC experiment introduced and the Compact Muon Solenoid detector is explained with various sub-detectors.

The main actors of the dijet analysis are hadronic jets. The jets are composite objects and therefore are not uniquely defined. For this reason, the reconstruction of the jets and the procedure for calibrating of the jets energies were also explained in this study.

The main thema of this thesis is searching for dijet resonance using LHC run 2 data from proton-proton collisions with centre-of-mass energy 13 TeV. The QCD prediction from PYTHIA is compared to the measured dijet mass distribution. The observed dijet mass spectrum is fitted by a smooth function to search the dijet resonances. Since there is no evidence of the presence of dijet resonances, the upper limits of the cross-section at the 95% Confidence Level are set.

The description of this analysis, in which the dijet resonance study was conducted, is explained in the last three sections. Data and simulation samples, selection criteria of the data and data quality checks are described in detail in those sections. As a result of these studies, if a dijet resonance exists it will be manifested as a bump in the dijet mass spectrum.

In this thesis, there is also a section where we define the signal models and the fit to data to estimate the background. The fit represents generally a test of smoothness of the dijet mass spectrum and it is the basis of the analysis.

GENİŞLETİLMİŞ ÖZET

Yüksek enerji fiziği, maddenin en temel yapısının neler olduğunu ve bu temel parçacıkların birbirleriyle nasıl etkileştiğini araştımaktadır. Bu araştırmalara yanıt bulmak için birçok deneysel ve kuramsal çalışmalar yapılmış ve birçoğu yıllar süren bu çalışmalar başarıyla test edilen ve maddenin yapı taşlarının özelliklerini ve etkileşimlerini açıklamayı amaçlayan ve aynı zamanda "Standart Model (SM)" olarak da adlandırılan temel bir kuramın oluşmasına yol açmıştır.

Yüksek enerji fiziği, uzayın ve zamanın doğasını, maddenin ve enerjinin etkileşimini yöneten güçlerin özelliklerini ve atom altı parçacıkların özelliklerini ve etkileşimlerini anlamayı amaçlamayan bu yüzyılın popüler bilim dalıdır. Atom altı parçacıkları düşük enerjiler kullanılarak gözlemlemek mümkün değildir. Bundan dolayı, temel parçacıkları ve bunların etkileşimlerini araştırmak için yüksek enerjilere ihtiyaç duyulmaktadır. Parçacıkları yüksek enerjilerde çarpıştırmak için parçacık çarpıştırıcılarına ve parçacıkların özelliklerini anlamak için ise detektörlere ihtiyaç vardır.

Büyük Hadron Çarpıştırıcısı (BHÇ), İsviçre ile Fransa sınırları içerisinde kurulan ve Avrupa parçacık fiziği laboratuarı CERN'de inşa edilen dünyanın en büyük ve en güçlü parçacık hızlandırıcısı ünvanına sahiptir. Büyük patlamadan sonra, milyarda bir saniye içinde var olan koşulları üretme fırsatı sunan BHÇ'de ışık hızına çok yakın hızlarda protonların veya kurşun iyonlarının çarpıştırılması ile bu koşullar yeniden oluşturulmaktadır.

Tüm deneysel veriler için tutarlı tahminlere sahip olan SM, temel parçacıkları ve bu temel parçacıklar arasındaki etkileşimleri tanımlamak için geliştirilmiş olmasına rağmen, elbette her teori gibi, SM de mükemmel bir teori değildir. Çünkü bu modelin; karanlık madde, karanlık enerji, nötrino kütleleri, madde ve anti-madde asimetrisi gibi yanıtlayamadığı bazı sorular vardır. Bununla birlikte, genel göreliliği de içermez. Yanıtlanamayan sorular bu şekilde devam ederken çözüm için CERN'deki BHÇ tarafından test edilen SM ötesi yeni fizik araştırmaları önerilmektedir. Bu soruları ele almaya çalışan kuramlar vardır ve genellikle “rezonans” denilen çok kısa ömürlü parçacıkların varlığını öngörürler. Bu tezde, SM ötesi kuramlar tarafından öngörülen ve iki jet’e bozunan yeni parçacıklar araştırılmıştır. Bu yeni parçacıklar, ikijet kütle dağılımı içinde arandı. Eğer iki-jet rezonansı mevcut ise, bu iki-jet kütle spektrumunda bir tepe olarak ortaya çıkması beklenir.

Herhangi bir teorik modele bağlı kalınmadığı ya da kullanılmadığı için çalışmamız model bağımsızdır. Ancak bir çift jeti oluşturan herhangi bir rezonansa duyarlı, sağlam ve basit bir analitik tekniğe sahibiz.

2012 yılının sonundan 2015 yılının yazına kadar geçen uzun bir kapanma sürecinden sonra BHÇ deneyi yeniden başlatıldı. 2012'de protonlar 7 TeV kütle merkezi enerjiyle çarpıştırılırken, 2015 yılında bu enerjinin yaklaşık iki katı enerji (13 TeV) ile çarpıştırılma sağlandı. Özellikle yüksek kütle rezonansı için, bu enerji artışının çok daha büyük tesir kesitlerine karşılık geldiğini göreceğiz.

2015 yılında CMS deneylerinde toplanan ve toplam ışınlılığı 1.9 fb^{-1} olan veriler ile elde edilen sonuçlar burada sunulmuştur.

Bu tez, Kuantum Kromodinamiğinin unsurlarını ve hadronik etkileşimlerin deneysel ölçümleri üzerine olan etkilerini hatırlatan SM’e kısa bir giriş sunmaktadır. Hadron çarpıştırıcılarındaki proton-proton etkileşiminin fizik elemanları da tanıtılmaktadır.

Yukarıda da bahsettiğimiz gibi, BHÇ çarpışmaları için erişilebilen kütle bölgesinde iki-jet rezonanslarını öngören; uyarılmış kuark, E_6 çiftkuark, axigluon, Randall-Sundrum graviton, sicim rezonans vb. gibi birkaç model bulunmaktadır. Bu tezde sunalacak CMS iki-jet analiz sonuçları bazı kuramsal modellerin beklentileri ile karşılaştırılmaktadır.

Çalışmanın bir bölümü detektörün tanımına ayrılmıştır. Burada BHÇ deneyi tanıtılmış ve Kompakt Müon Solenoid detektörü çeşitli alt detektörleriyle birlikte anlatılmıştır.

İki-jet analizinin ana aktörleri hadronik jetlerdir. Jetler ise kompozit nesnelerdir ve bu nedenle eşsiz bir şekilde tanımlanmamaktadırlar. Bu nedenle bu çalışmada jetlerin yeniden yapılandırılması ve jetlerin enerjilerinin kalibre edilme prosedürü üzerinde de durulmuştur.

Bu tezin ana konusu, BHÇ'de kütle merkezi enerjisi 13 TeV olan proton-proton çarpışmalarında BHÇ veri 2 kullanılarak iki-jet rezonans araştırması yapmaktır. PYTHIA'dan gelen QCD öngörüsü ölçülen iki-jet kütle dağılımı ile kıyaslanmaktadır. İki-jet resonanslarını araştırmak için ölçülen iki-jet kütle dağılımı düz bir fonksiyon ile bağdaştırılmaktadır. İki-jet resonanslarının varlığına dair herhangi bir kanıt olmadığı için de iki-jet rezonans çalışmalarında 95% lik güvenirlik seviyesindeki tesir kesitlerinin üst limitleri hesaplanmaktadır.

İki-jet rezonans araştırmasının yapıldığı bu analizin tarifi, son üç bölüme ayrılmış olup, bunlar; veri ve simülasyon örnekleri, verilerin seçim kriterleri ve veri kalite kontrolleri adı altında detaylı bir şekilde anlatılmaktadırlar. Yapılan bu çalışmalar neticesinde eğer bir iki-jet rezonansı mevcut ise bu iki-jet kütle spektrumunda bir tepe olarak karşımıza çıkacaktır.

Bu tezde arka planı tahmin etmek için sinyal modellerini ve verilere uyumu tanımladığımız bir bölüm de mevcuttur. Fit, temel olarak gözlenen iki-jet kütle spektrumunun düzgünlüğünü gösteren bir testtir ve analizin de temelini oluşturmaktadır.

ACKNOWLEDGMENTS

I would like to thank my supervisor İsa Dumanoğlu for being my model of a brilliant scientist. Thank him for his great encouragement, advice and endless support throughout my studies. It was a great opportunity for me to have him as a supervisor.

I would also like to thank my co-supervisor Sertaç Öztürk for his great encouragement and advice during my graduate studies. He has always showed me the best ways for my carrier. It was a great chance for me to have him as a second supervisor.

I owe a great debt of gratitude to Robert M. Harris for his extraordinary support and guidance throughout the thesis work. He has shared his knowledge and all his experiences with me during my PhD period.

I thank all of the members of the Dijet Resonance Team for their help and friendship, especially Ayşe Bat, Giulia D'Imperio and David Sheffield.

I would like to express my thanks to Cukurova University High Energy Physics group, Aysel Kayış Topaksu, Gülsen Önengüt, Eda Eşkut and Ayşe Polatöz.

I am also grateful to Shuichi Kunori who has shared all his knowledge and experince with me. I have learned a lot of things about HCAL from him.

I wish to thank my dear friends and colleagues Sk. Noor Alam, Ashpreet Kaur Duggal, Ziyafer Gizem Portakal, Sibel Akça, Emine Gürpınar, Yalçın Güler, Çağlar Zorbilmez and Cafer Bayar for their support and contributions to keep my morale and motivation high.

I would like to thank Turkish Atomic Energy Agency, TAEK, for supporting me during the visiting period in CERN (project code: 2014TAEK(CERN)A5.H6.F2-12). Also, I want to thank a lot the Research Funding Projects Unit in Çukurova University for their support to this PhD Thesis under the project number FDK-2015-2655.

My deepest thanks go to my beloved wife Esra Esaf Damarseçkin for her love, support and encouragement which made this journey possible, and my adorable daughters Tuğçe Naz and Dilara Damarseçkin for making everything more meaningful and more beautiful in my life. Without their support and encouragement, it would be hard to pursue my graduate abroad.

CONTENTS **PAGE**

LIST OF TABLES **PAGE**

LIST OF FIGURES **PAGE**

ABBREVIATIONS

ALICE	: A Large Ion Collider Experiment: Angström
ATLAS	: A Toroidal LHC Apparatus
BSM	: Beyond the Standard Model
CDF	: Collider Detector at Fermilab
CERN	: Conceil Europeenne pour la Recherche Nucleaire
CL	: Confidence Level
CMS	: Compact Muon Solenoid
CTEQ	: Coordinated Theoretical-Experimental project on QCD
DAQ	: Data AcQusition
ECAL	: Electromagnetic CALorimeter
FSR	: Final State Radiation
HCAL	: Hadronic CALorimeter
HB	: Hadronic Barrel
HE	: Hadronic Endcap
HF	: Hadronic Forward
HLT	: High Level Trigger
ISR	: Initial State Radiation
JES	: Jet Energy Scale
JER	: Jet Energy Resolution
LEP	: Large Electron Positron Collider
LHC	: Large Hadron Collider
LHCb	: Large Hadron Collider Beauty Experiment
LO	: Leading Order
MC	: Monte Carlo
NLO	: Next-to-Leading Order
PDF	: Parton Density Function

RPC	: Resistive Plate Chambers
QCD	: Quantum Chromo Dynamics
SM	: Standard Model
SPS	: Super Proton Synchrotron
SST	: Silicon Strip Tracker
TEC	:Tracker End Caps
TIB	:Tracker Inner Barrel
TID	:Tracker Inner Disks
TOB	:Tracker Outer Barrel

1. INTRODUCTION

High energy physics searches the ultimate answers of these two questions:

- What are the most basic elements of the matter?
- How are they interacting with each other?

In order to answer these questions both theoretical and experimental studies have been carried out. These studies have led to a basic theory called the "*Standard Model* (SM)", which has been successfully tested for the last 30 years. This model has consistent predictions almost for all experimental data and has been developed to describe the basic particles and interactions between them. Of course, like every theory, SM also is not a perfect theory. Because there are some questions that this model can not answer such as the predominance of matter over antimatter and the origin of the dark matter. However, it also does not include the general relativity. In order to find answers to these questions, the existence of new physics beyond the SM was suggested. Their prediction has been tested at Large Hadron Collider (LHC) since it has built at CERN near Geneva.

There are several models to find answer to these questions and they predict very short-lived particles called the "resonance" at the TeV scale. In this thesis narrow resonances which are predicted by the theories beyond the SM and decay to a pair of quarks or pair of gluons or quark and gluons, have been investigated. The decay products will appear as a pair of back-to-back hadronic jets in the transverse plane. If these new narrow resonance particles, which are searched in the dijet mass distribution, exists then they will emerge as a bump in the dijet mass spectrum as shown in Fig.1.1 below.

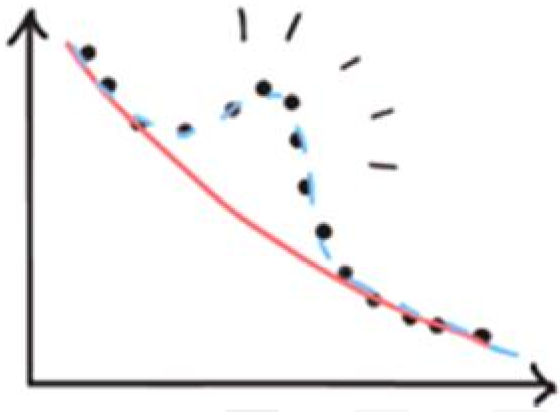

Figure 1.1. A bump in the dijet mass spectrum

Our study is model independent, since we don't assume any theoretical model. But we have a robust and simple analytical technique that is sensitive to any resonance consist of a pair of jets. The LHC run was restarted in summer 2015 at the 13 TeV center of mass energy after a long shutdown at the end of 2012. In 2012, the protons were colliding at 7 TeV center-of-mass energy. Especially for high mass resonances, we will see that this energy increase corresponds to much larger cross sections.

The results obtained from the 1.9 fb^{-1} data collected in the CMS experiments in 2015 are presented here.

The theoretical motivation behind of this analysis will be explained in detail in this Chapter. The Standard Model (SM) jet production, Quantum Chromodynamics (QCD) and two-jet resonance models will be introduced. The physics elements of the proton-proton interaction in hadron colliders have also been introduced. Also, the description of the experimental apparatus is given in this Chapter. The LHC, the Compact Muon Solenoid (CMS) experiment and all the sub-detectors of CMS are introduced in this section.

Hadronic jets are one of the most important elements of dijet analysis. As known, jets are composite objects, and thus they are not fully identifiable.

Recognizing this, in the next Chapter, Chapter 2, in the CMS experiment, jet reconstruction methods are given for calibrating the jet energy.

The dijet resonance study of proton-proton collisions at 13 TeV center-of-mass energy is the subject of this thesis and the analysis process is divided into 3 parts. These parts are given in Chapter 2 as data and simulation examples, selection criteria and quality controls.

Finally, in Chapter 3, signal models and the fit to data for the estimation of the background will be defined. Then, search for new particles, the results and their statistical interpretation will be presented.

1.1. Theoretical Motivation

The theoretical motivation behind of this analysis will be explained in detail in this chapter. This chapter also includes the general and/or specific information about the SM jet production, QCD and two-jet resonance models. The physics elements of the proton-proton interaction in hadron colliders have also been introduced in this chapter.

1.1.1. The Standard Model

The SM is the most extensive theory to describe the properties and interactions of all elementary particles which have been discovered until now. According to the SM, these interactions are weak, strong and electromagnetic forces. Although in nature there are four fundamental forces, gravitational interaction is not described in the SM. It is the weakest of the four interactions for this subject; therefore it is important only for the macroscopic objects. The strong force is responsible for binding of nuclei. The gluons are the force carriers of this strong interaction. The electromagnetic force is the force which exists between all particles which have an electric charge. The photon is the force carriers particle for electromagnetic interaction. The weak force is described as responsible for the radioactive decay of subatomic particles. This interaction takes place by the absorption or emission of the $W^{\pm}$ and Z^0 bosons.

Generally, the SM consists of quarks, leptons called fermions and force carrying bosons. Fermions have spin -1/2 and obey both to the Pauli Exclusion Principle and to the Fermi-Dirac statistic in particle physics. The SM includes 12 fermions; 6 quarks (u, d, s, c, b, t) and 6 leptons (e, μ, τ, ν_e, ν_μ, ν_τ) and there is an anti-particle of each fermion. Looking at their weight, up (u), down (d), strange (s) quarks are light and charm (c), bottom (b), top (t) quarks are heavy. Fig. 1.2 shows the particle information of the SM. As shown in Fig. 1.2 e, μ and τ (three leptons) have negative electric charge and their anti-particles have positive charge. The other three leptons, their neutrinos, are chargeless and pointed out by the symbol ν; ν_e, ν_μ and ν_τ.

The SM is a gauge invariant quantum field theory based on the symmetry group $SU(3)_C \times SU(2)_L \times U(1)_Y$, with the colour group $SU(3)_C$ for the strong interaction described by the QCD and with $SU(2)_L \times U(1)_Y$ for the electroweak interaction described by Electroweak Theory and spontaneously broken by the Higgs mechanism. Table 1.1 shows the gauge bosons of the Standard Model.

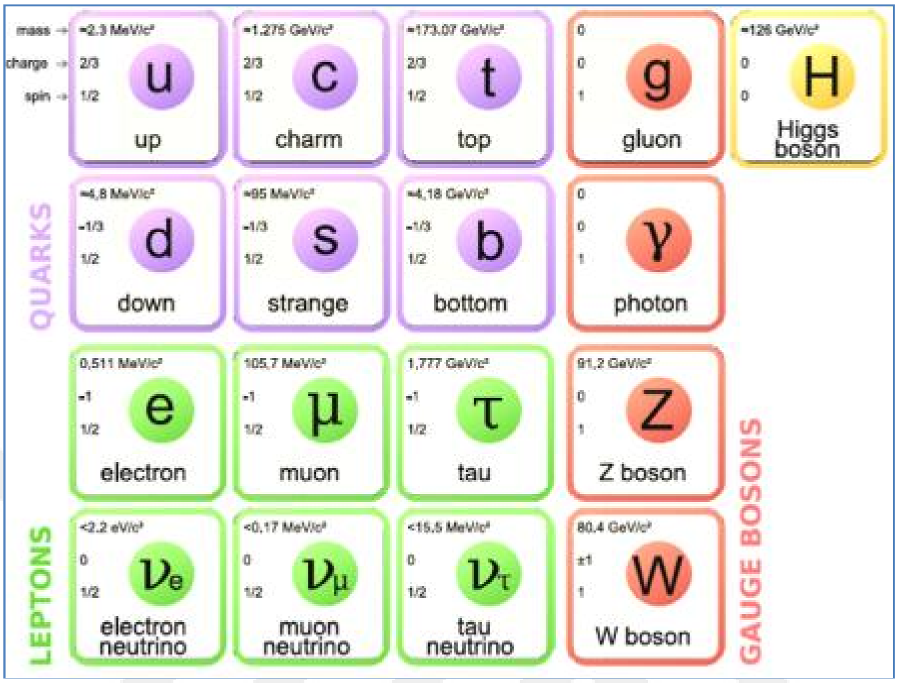

Figure 1.2.The particles in the standard model (https://en.wikipedia.org/wiki/Standard_Model#/media/File:Standard_Model_of_Elementary_Particles.svg)

The masses, charges, and spins of particles can be seen in the table (Table 1.1).

Table 1.1. The gauge bosons of the SM

Gauge Bosons(Force Carrier)	Charge	Spin	Mass (GeV/c^2)
Gluon (g, Strong)	0	1	0
Photon (γ, Electromagnetic)	0	1	0
$W^{\pm}$ (Weak)	±1	1	80.423±0.039
Z^0 (Weak)	0	1	91.1876±0.0021

1.1.2. Quantum Chromodynamics

One of the cornerstones of the SM is QCD (Ellis, 1996, Narrison, 2004) and it is a quantum field theory which describes the strong interaction between quarks and gluons through color charges under $SU(3)_C$ transformations. Also, the QCD theory is a renormalizable non-Abelian gauge theory of $SU(3)_C$ symmetry group (Salam, 2011). According to QCD theory, there are three color charges which are called red (*r*), green (*g*) and blue (*b*) and form a triplet under $SU(3)_C$ and both quarks and gluons have color charge which can have these three degrees of freedom. The color charges are represented as by three-component column vector as following:

$$\text{Red} = \begin{pmatrix} 1 \\ 0 \\ 0 \end{pmatrix}, \ \text{Green} = \begin{pmatrix} 0 \\ 1 \\ 0 \end{pmatrix}, \ \text{Blue} = \begin{pmatrix} 0 \\ 0 \\ 1 \end{pmatrix} \tag{1.1}$$

In nature, however, they exist only color neutral states of quark configurations: $q\bar{q}$ and qqq which are called mesons and baryons respectively and they are both referred to as hadrons. The gluons are colorful objects and they are mixtures of two colors such as blue and anti-green. In terms of the color $SU(3)_C$ symmetry, there should be nine types of them: $r\bar{r}$, $r\bar{b}$, $r\bar{g}$, $b\bar{r}$, $b\bar{b}$, $b\bar{g}$, $g\bar{r}$, $g\bar{b}$, $g\bar{g}$.

A possible representation of these color states as a singlet and an octet is shown in Table 1.2. The color singlet gluon would not couple to colour charge and for this reason it does not contribute to the interaction and it does not exist. The others gluon types which are called color octed have eight independent color states and they are linear combinations of a color and an anti-color charge.

Table 1.2. Color representation of nine possible states (singlet, octet) for gluon

Singlet	$\left(r\bar{r}+b\bar{b}+g\bar{g}\right)/\sqrt{3}$
Octet	$\left(r\bar{b}+b\bar{r}\right)/\sqrt{2}$
	$i\left(r\bar{b}-b\bar{r}\right)/\sqrt{2}$
	$\left(r\bar{r}-b\bar{b}\right)/\sqrt{2}$
	$\left(r\bar{g}+g\bar{r}\right)/\sqrt{2}$
	$i\left(r\bar{g}-g\bar{r}\right)/\sqrt{2}$
	$\left(b\bar{g}+g\bar{b}\right)/\sqrt{2}$
	$i\left(b\bar{g}-g\bar{b}\right)/\sqrt{2}$
	$\left(r\bar{r}+b\bar{b}-2g\bar{g}\right)/\sqrt{6}$

1.1.2.1. The Quantum Chromodynamics Lagrangian

The Lagrangian of the SM is symmetric under the gauge group $SU(3)_C \times SU(2)_L \times U(1)_Y$. The model can be examined in two parts, electroweak (EW) and strong (QCD). And their Lagrangian is written as followings:

$$\mathcal{L}_{SM} = \mathcal{L}_{EW} + \mathcal{L}_{QCD} \tag{1.2}$$

For the analysis presented in this thesis we will focus on the QCD part. The QCD Lagrangian density (Ellis, 1996) has three components and it can be given by

$$\mathcal{L}_{QCD} = \mathcal{L}_{classical} + \mathcal{L}_{gauge-fixing} + \mathcal{L}_{ghost} \tag{1.3}$$

It is known that the full QCD Lagrangian density is the sum of gluon and quark terms. Firstly the quark part of the Lagrangian will be discussed. As mentioned in the previous topic, the quarks are fermionic particles with spin ½ and they must obey the Dirac equation. Also, a quark field that can be described as a Dirac spinor comes with three color states. So, the quark field spinor ψ as a three component column vector is written as,

$$\vec{\psi} = \begin{pmatrix} \psi_1 \\ \psi_2 \\ \psi_3 \end{pmatrix} \tag{1.4}$$

where each term is a 4-component spinor. Then, the quark part of the Lagrangian density can be written as;

$$\mathcal{L}_q = \bar{\Psi}_a \left[\not{\partial}_\mu - M \right] \Psi_b \tag{1.5}$$

where

$$\bar{\Psi}_a = \left(\Psi_1^\dagger \gamma^0, \Psi_2^\dagger \gamma^0, \Psi_3^\dagger \gamma^0 \right) \tag{1.6}$$

$$\not{\partial}_\mu = \begin{pmatrix} \gamma^\mu \partial_\mu & 0 & 0 \\ 0 & \gamma^\mu \partial_\mu & 0 \\ 0 & 0 & \gamma^\mu \partial_\mu \end{pmatrix} \tag{1.7}$$

$$M = \begin{pmatrix} m & 0 & 0 \\ 0 & m & 0 \\ 0 & 0 & m \end{pmatrix} \tag{1.8}$$

In these equations it is assumed that the three diferent color states of a given quark has the same mass. $\bar{\Psi}_a$, $\not{\partial}_\mu$, M values are put into Eq. 1.5 respectively, Lagrangian density can be rewritten as:

$$\mathcal{L}_q = \bar{\Psi}_a \left[i\gamma^{\mu}\partial_{\mu}\delta_{ab} - g_s\gamma^{\mu}t^{C}_{ab}A^{C}_{\mu} - m \right]\Psi_b \tag{1.9}$$

where μ(0,1,2,3) and C (r,b,g) are a Lorentz and a colour index respectively. The γ^{μ} are the Dirac γ-matrices and the A^{C}_{μ} correspond to gluon fields. The g_s is the QCD strong coupling constant. Also the t^{C}_{ab} factor in Eq. 1.9 correspond to eight 3×3 matrices and are the generators of the $SU(3)_C$ group. It is easy to understand the expression $t^{C}_{ab}A^{C}_{\mu}\Psi_b$ in Eq. 1.9, when a gluon interacts with a quark; this gluon ends up with taking away one colour of quark and replacing it with another. It can be said that, quark-gluon interaction repaints the color of quark. Now, the free gluon Lagrangian density must be added to the Lagrangian density for wholeness as the second part of the QCD. This part of the QCD Lagrangian density is gluonic. The free gluon Lagrangian is given as follows;

$$\mathcal{L}_{gluons} = -\frac{1}{4}F_{\mu\nu}F^{\mu\nu} \tag{1.10}$$

where $F_{\mu\nu}$ is the gluon field tensor and it can be given by

$$F^{\mu\nu} = \partial^{\mu}A^{\nu} - \partial^{\nu}A^{\mu} - g[A^{\mu}, A^{\nu}] \tag{1.11}$$

A^{μ} is 3 × 3 gluon potential matrix which has fixed gauge term and it must be chosen to define the gluon propagator. For this reason the free gluon Lagrangian density should have two terms which are called “gauge fixing” and the “Fadeev-Popov ghosts” term. The gauge fixing term is expressed as;

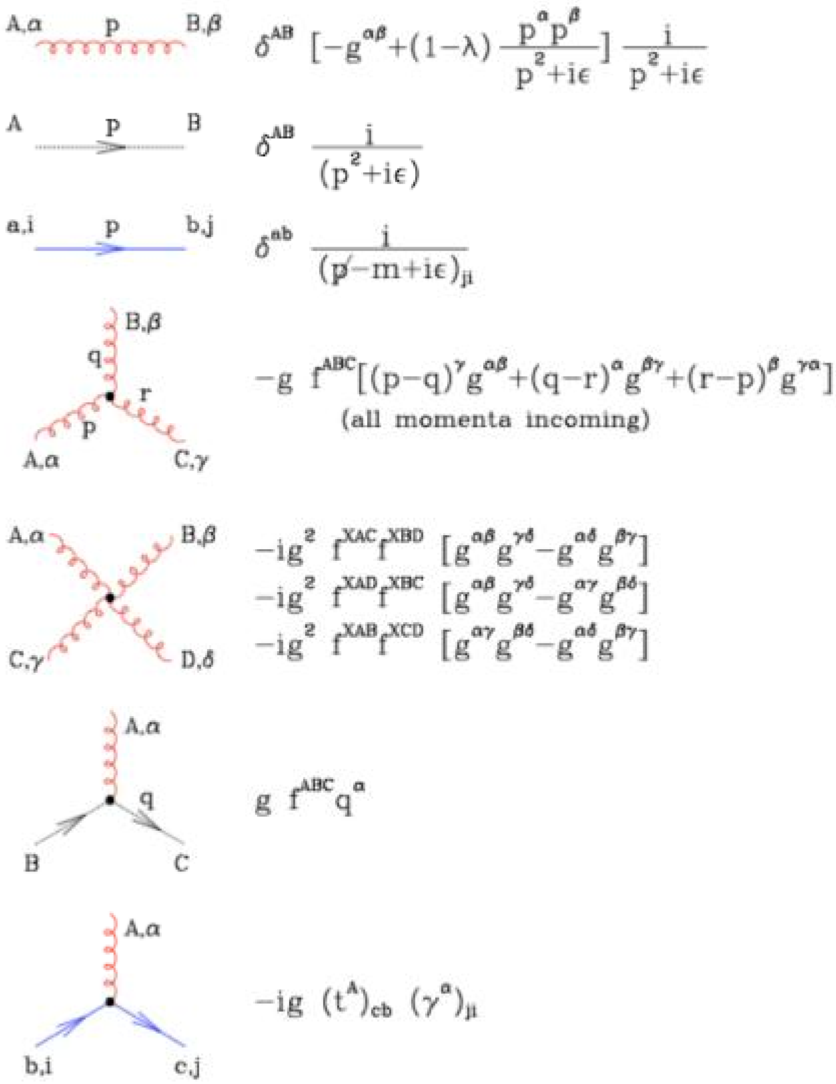

Figure 1.3. QCD Feynman rules (Ellis, 1996)

$$\mathcal{L}_{gauge-fixing} = -\frac{1}{2\lambda}\left(\partial_{\mu}A^{\mu}\right)^2 \tag{1.12}$$

where λ is the gauge parameter. This parameter is given as the generalization class of the Lorenz gauge, which is named "R_{λ} gauge". This covariant fixing term must be supplemented by a ghost Lagrangian which is needed for the non-abelian theory. It is given by

$$\mathcal{L}_{ghost} = \partial_\alpha \eta^{A\dagger} (D^\alpha_{AB} \eta^B) \tag{1.13}$$

where η^A is a complex scalar field and D is the covariant derivative.

1.1.2.2. The Running Coupling Constant

One of the remarkable properties of QCD is running coupling constant. In other words it is called asymptotic freedom. Since, the origin of asymptotic freedom has arisen from this QCD running coupling constant estimation. As mentioned in the previous topic, the g (in Eq. 1.9) is the QCD strong coupling constant. And as known that QCD is a renormalizable field theory and it implies that the coupling constant must be defined by its value at a ***renormalization scale***, and is defined $g(\mu)$. It is commonly expressed in terms of the fine-structure constant of the strong interaction,

$$\alpha_s = \frac{g^2}{4\pi} \tag{1.14}$$

This equation also determines the strength of an interaction. Essentially, g(μ) controls the amplitude which connects any state to another state with one more or one fewer gluon, with the inclusion of quantum corrections which take place over time scales from zero up to $\hbar/\mu$ (if μ is measured in energy units). The QCD Ward IDs given above guarantee that the coupling is the same not only for the quarks but also for the gluons, and in fact it remains the same in all terms in the Lagrangian and ensures that the QCD symmetries are destroyed by renormalization (Sterman, 2005). The running coupling constant α_s is determined by the renormalization group equations with β functions (Ellis, 1996).

$$\frac{\mu^2}{\alpha_s(\mu^2)}\frac{\partial\alpha_s(\mu^2)}{\partial(\mu^2)} = -\frac{\alpha_s(\mu^2)}{4\pi}\beta_0 - (\frac{\alpha_s(\mu^2)}{4\pi})^2\beta_1 - (\frac{\alpha_s(\mu^2)}{4\pi})^3\beta_2 + \cdots \quad (1.15)$$

where β depends on n_f. Fig. 1.4 shows the change of α_s with energy μ. The energy dependence of $\alpha_s(\mu^2)$, retaining only coefficient β_0 and after solving Eq. 1.15, is given to first order by;

$$\alpha_s(\mu^2) = \frac{1}{b\ln\left(\frac{\mu^2}{\Lambda^2}\right)} \quad (1.16)$$

where

$$b = \frac{11N_C-2n_f}{12\pi} = \frac{33-2n_f}{12\pi} \quad (1.17)$$

N_C is the numbers of colors (which is 3: r,b and g) and n_f is the number of different flavour of quarks. Λ (also called Λ_{QCD}) is QCD scaling parameter.

The scale μ of the renormalization is directly proportional to the magnitude of momentum transferred (Q) in the interaction ($\mu \approx$ Q). The results are diverging during the calculation of higher-order loop corrections in the quark-gluon coupling.

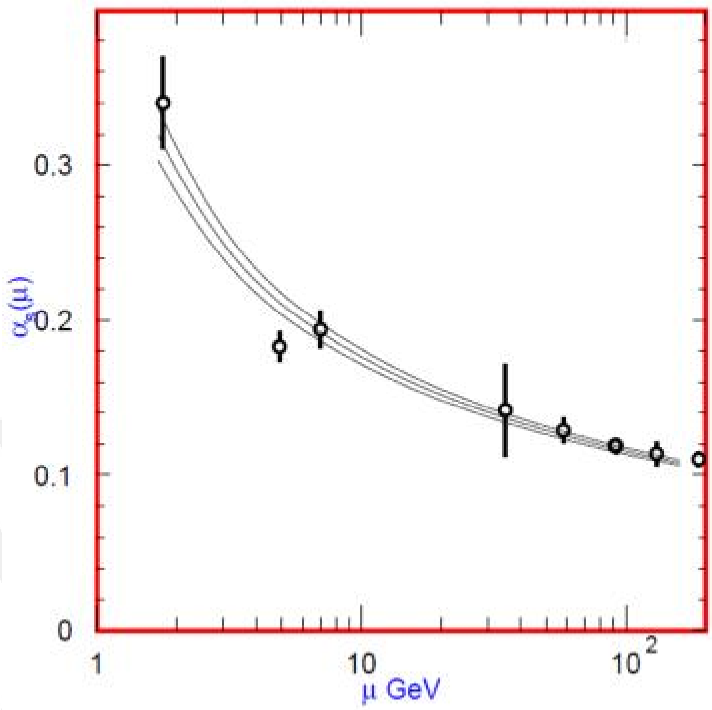

Figure 1.4. Measured values of α_s(μ) against the values of μ (Hinchliffe, 2000)

In order to make up for this divergence, the mass scale, Λ, is brought to the coupling constant. The QCD coupling constant the Eq. 1.16 can be rewritten as,

$$\alpha_s(Q^2) = \frac{12\pi}{(33-2n_f)\ln\left(\frac{Q^2}{\Lambda^2}\right)} \tag{1.18}$$

where

$$\Lambda^2 = \mu^2 exp\left(\frac{-12\pi}{(33-2n_f)\alpha_s(\mu^2)}\right) \tag{1.19}$$

Eq. 1.18 shows the Q^2 dependence of α_s. For large values of Q^2, α_s becomes small. This is the definion of the "**asymtotic freedom**". This emphasize that QCD asymptotically converges to zero at high energies or short distances. And so, when $Q^2 \to \infty$, quarks act as free particles under this approach.

The strong coupling α_s as a function of the Q (the energy scale) is shown in Fig. 1.5a. The current world average value of QCD coupling is $\alpha_s(M_Z^2)$ = 0.1184 ± 0.0007 (Beringer et al., 2012). The summary for values of $\alpha_s(M_Z^2)$ obtained for various subclasses of measurements is also shown in this Fig. 1.5b (Beringer et al., 2012).

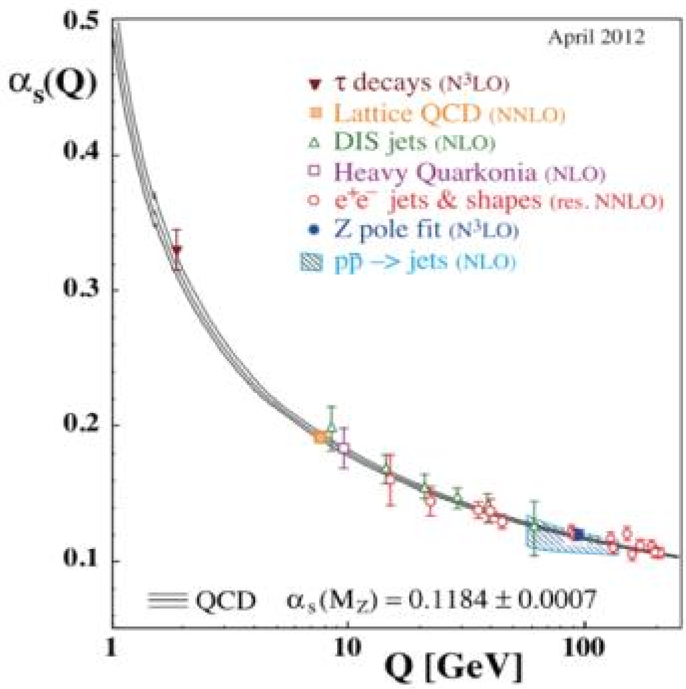

Figure 1.5a. Summary of measurements of α_s as a function of the energy scale Q. The respective degree of QCD perturbation theory used in the extraction of α_s is indicated in brackets (NLO: next to leading order; NNLO: next-to-next-to leading order; res NNLO: NNLO matched with resumed next-to-leading logs; N3LO: next-to-NNLO) (Beringer et al., 2012)

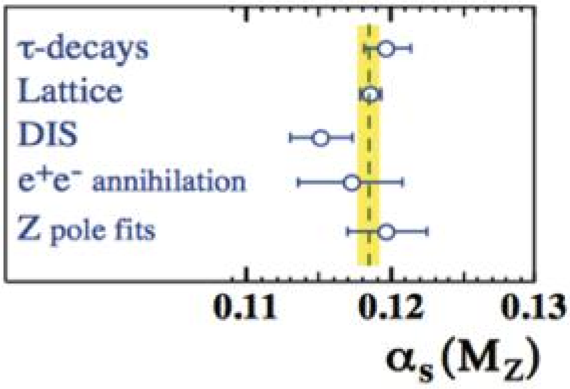

Figure 1.5. b. Summary of values of $\alpha_s(M_Z^2)$ (Beringer et al., 2012)

The smaller Q^2, the stronger "strong" force between two colored particles. This process is called **color confinement** in QCD theory. Depending on the color confinement, the colored particles can not to be observed individually at distances less than 1/**Λ**. On the contrary, if Q^2 gets higher, the strong force between two quarks becomes weaker and two quarks are separated, a new quark-antiquark pair, a meson, spontaneously is created from vacuum. This process of additional quark-antiquark pairs creation by the color force and the reorganization of quarks into hadrons is referred to as **hadronization** or **fragmentation**. The fragmentation of a single gluon or quark causes a tight cone of particles, which is called a "Jet". The description of the jet production in hadron collision is shown Fig. 1.6.

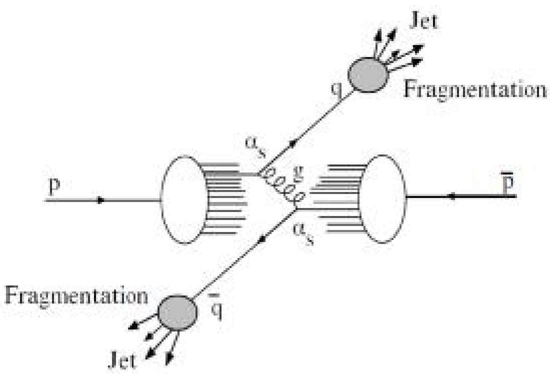

Figure 1.6. Description of the jet production in hadron collision

1.1.2.3. Parton Disribution Functions

The Parton name was suggested by Richard Feynman in 1969 as a generic definition for any particle component within the neutron, proton and other hadrons. These particles are known today as gluons and quarks. The quarks which represent the quantum numbers of hadrons are called valence quarks. According to the Quark-Parton Model, an energetic hadron consists of three valence quarks. For example, A proton consist of three-valence quarks, $u_v u_v d_v$, accompanied by many quark-antiquark pairs (sea quarks) $u_s\bar{u}_s$, $d_s\bar{d}_s$, $s_s\bar{s}_s$ as illustrated in Fig. 1.7.

These valence quarks are imbedded in a sea of virtual quark-antiquark pairs generated by the gluons which binds quarks within the protons. All of these particles (sea quarks, gluons and valence quarks) are called partons. Additionally, the lifetime of the virtual partons are limited by the Heisenberg uncertainty principle.

The momentum distribution functions of the partons within the protons are called Parton Distribution Functions (PDF) when the spin direction of the partons is not taken into consideration.

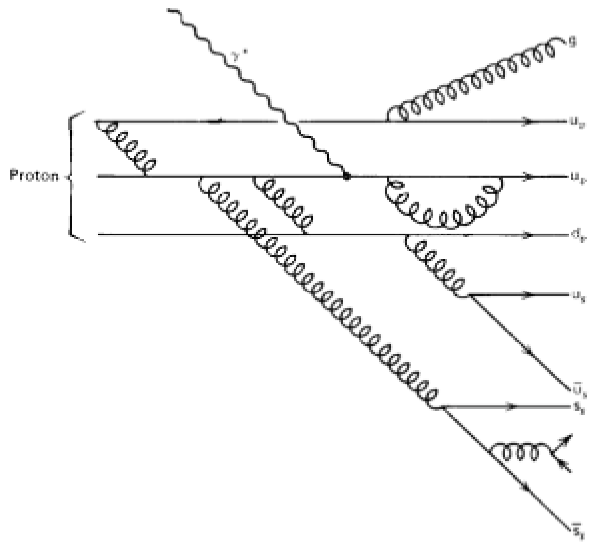

Figure 1.7. An illustration figure for proton made of valence quarks, gluons and sea quarks (Halzen and Martin, 1984)

PDF explains the possibility to find a parton of a given flavor at a certain Bjorken-*x* value (Eq 1.20) in a given hadron. In the Bjorken scaling, the fraction of the overall proton momentum carried by the particular parton is measured in the frame of infinite momentum.

$$x = \frac{Q^2}{2P.q} = \frac{Q^2}{2M\nu} \tag{1.20}$$

where P is the momentum of the parton, which is engaged in the hard interaction. These constituents carry a fraction of total hadron momentum given by parton distribution function (PDF). For example, if a proton travels with momentum of 6.5 TeV as in LHC and if Bjorken-*x* of a quark is equal to 0.1, then this means that this quark carries 650 GeV by itself. The Fig. 1.8 shows the parton distribution functions of the leading proton constituents from ZEUS and H1 experiments at DESY.

1.1.3. Jet Production in a Hadron Collision

According to the Quark-Parton Model, protons are made of point like constituents called *parton*, quarks and gluons, which mean that during the hard scattering process between two hadrons, the real interaction take place between the quarks and gluons, the components of incoming hadrons. A shematic view for hard scattering events can be found in Fig. 1.9 (Ellis, 1996).

The Feynman rules are used to calculate many predictions of QCD, such as, cross section. The cross section is the probability of a given process between an initial state and a final state is denoted by the symbol σ.

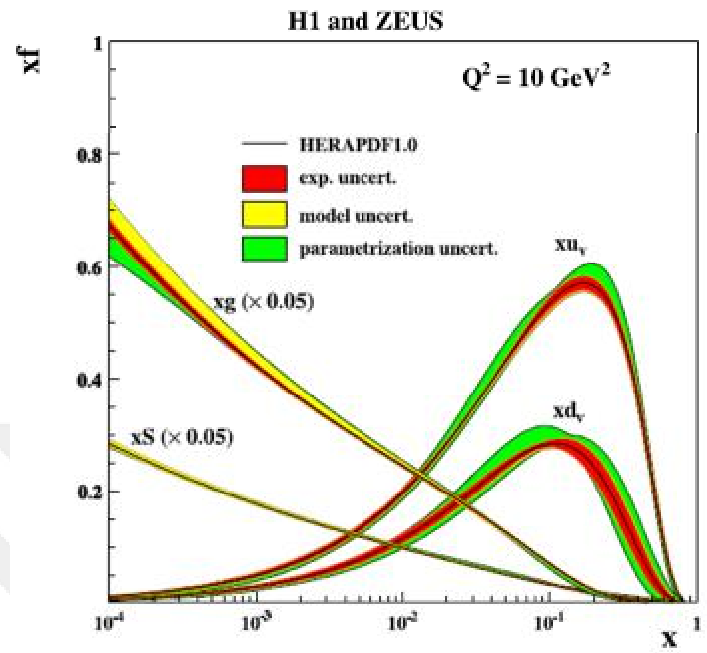

Figure 1.8. The parton distribution functions from the HERAPDF 1.0 at Q^2 = 10 GeV^2 for gluons (g), sea quarks (S), the up valance quarks (u_μ) and the down valance quarks (d_μ). The gluon and sea quarks distributions are scaled down by a factor 20 (Petrukhin, 2010)

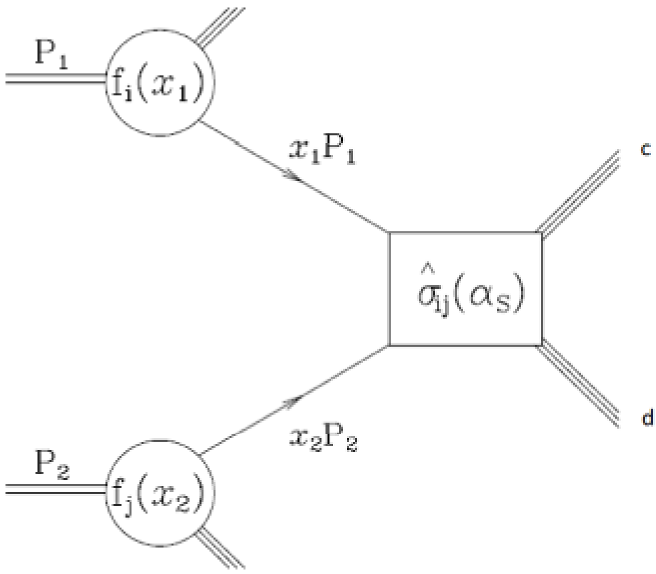

Figure 1.9. Schematic view of a hard scattering process

The cross section for the hard scattering processes initiated by two hadrons with four-momenta, P_1 and P_2 can be expressed as (Francisco, 2007);

$$\sigma(P_1,P_2)=\sum_{i,j}\int dx_1 dx_2\, f_i(x_1,\mu_F^2)\, f_j(x_2,\mu_F^2)\, \hat{\sigma}_{i,j}\left(p_1,p_2,\alpha_s(\mu^2),Q^2/\mu^2\right) \quad (1.21)$$

where $p_1 = x_1P_1$ and $p_2 = x_2P_2$ are the momenta of the partons for hard scattering (Fig. 1.9), x_1 and x_2 are Bjorken scale which are fraction of hadron momentum carried by interacting partons. The functions $f_i(x_1,\mu_F^2), f_j(x_2,\mu_F^2)$ are the quark gluon parton distribution functions (PDF) defined at a factorization scale, μ_F and Q is a hard scattering scale. The short-distance (partonic) cross section for the scattering of partons type ***i*** and ***j*** is represented by $\hat{\sigma}_{ij}$ (Ellis, 1996).

$$\hat{\sigma}_{ij} = \iint f_{q,i}(x_q,Q^2)\, f_{q,j}(x_q,Q^2)\, (\hat{\sigma}_0 + \alpha_s(\mu^2)\hat{\sigma}_1 + \ldots)dx_q dx_q \quad (1.22)$$

1.1.4. Two-Jet Cross Section

When two hadrons collide inelastically, the real interaction takes place in terms of a momentum transfer between two components of the colliding hadrons. As seen in Fig. 1.9 c and d the outgoing partons, are observed as jets since they finally turn into a spray of color singlet particles, namely hadrons. From the conservation of momentum, the momenta of the two final-state partons will be the same in magnitude and opposite direction in the center-of-mass frame. For a 2 → 2 parton scattering process

$$parton_i(p_1^\mu) + parton_j(p_2^\mu) \rightarrow parton_c(p_3^\mu) + parton_d(p_4^\mu) \quad (1.23)$$

described by a matrix element M, the differential cross section is given by (Ellis, 1996)

$$\frac{E_3E_4\, d^6\hat{\sigma}}{d^3p_3\, d^3p_4} = \frac{1}{2\hat{s}}\frac{1}{16\pi^2}\overline{\sum}|M|^2\delta^4(p_1+p_2-p_3-p_4) \quad (1.24)$$

where $\overline{\sum}$ indicates the averaged sum over the initial and the final state spins and colors. The leading-order (LO) and next-to-leading order (NLO) parton-parton contributions can be derived from the diagrams shown in the Fig. 1.10 by including all the crossing symmetries of the given diagrams. The expressions for the total scattering amplitude matrix elements squared, $\overline{\sum}|M|^2$, are given in Table 1.3, where the Mandelstam variables of the process are defined as $\hat{s}=\left(p_1^{\mu}+p_1^{\mu}\right)^2$, $\hat{u}=\left(p_1^{\mu}-p_3^{\mu}\right)^2$ and $\hat{t}=\left(p_2^{\mu}-p_3^{\mu}\right)^2$.

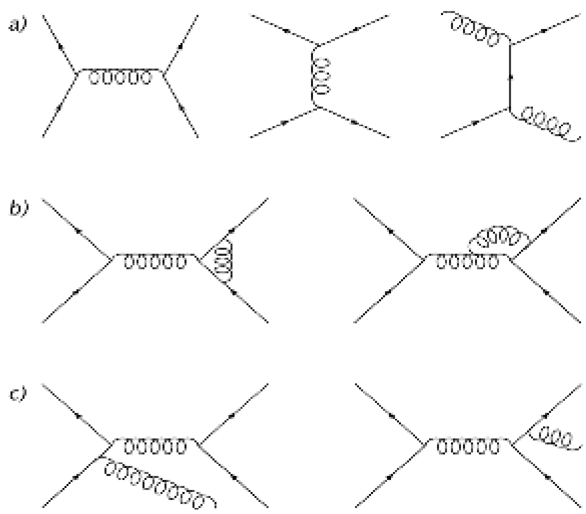

Figure 1.10. Feynman diagrams which contribute to jet production. (a) Leading order (LO) diagrams, (b) next-to-leading order (NLO) diagrams with virtual gluon loops, (c) NLO diagrams with initial state radiation (ISR) and final state radiation (FSR)

The two-jet inclusive cross section from a particular combination of incoming (i, j) and outgoing (k, l) partons can be written using Eq. (1.24);

$$\frac{d^3\sigma}{dy_3 dy_4 dp_T^2}=\frac{1}{16\pi^2 s}\sum_{i,j,k,l=q,\bar{q},g}\frac{f_i(x_1,\mu^2)}{x_1}\frac{f_j(x_2,\mu^2)}{x_2}\overline{\sum}\,|M(ij\rightarrow kl)|^2\frac{1}{1+\delta_{kl}} \quad (1.25)$$

where y_3 and y_4 rapidity of outgoing partons in the laboratory frame, $f_i(x,\mu^2)$ are the distributions for partons of type i (i = $\mathrm{u}, \bar{\mathrm{u}}, \mathrm{d}, \bar{\mathrm{d}}, \mathrm{g}$, ...,etc.) and μ is momentum scale. For the x_1 and x_2 which are momentum fractions are determined by using the transverse momentum conservation

$$x_1 = \frac{1}{2}x_T(e^{y_3}e^{y_4}), \quad x_2 = \frac{1}{2}x_T(e^{-y_3}e^{-y_4}) \tag{1.26}$$

where $x_T = 2P_T/\sqrt{s}$. The equal and opposite rapidities ($\pm y^*$) of the two jets in the parton-parton center of mass frame and the laboratory rapidity ($\bar{y}$) of the two

Table 1.3. Matrix element for the various constituent quark-quark, quark-gluon, and gluon-gluon (2→2) subprocesses (Ellis, 1996)

Process	$\overline{\sum}\lvert M\rvert^2/g^4$
$qq \to qq$	$\frac{4}{9}\frac{\hat{s}^2+\hat{u}^2}{\hat{t}^2}$
$qq' \to qq'$	$\frac{4}{9}\left(\frac{\hat{s}^2+\hat{u}^2}{\hat{t}^2}+\frac{\hat{s}^2+\hat{t}^2}{\hat{u}^2}\right)-\frac{8}{27}\frac{\hat{s}^2}{\hat{u}\hat{t}}$
$q\bar{q}' \to q\bar{q}'$	$\frac{4}{9}\frac{\hat{s}^2+\hat{u}^2}{\hat{t}^2}$
$q\bar{q} \to q\bar{q}$	$\frac{4}{9}\left(\frac{\hat{s}^2+\hat{u}^2}{\hat{t}^2}+\frac{\hat{u}^2+\hat{t}^2}{\hat{s}^2}\right)-\frac{8}{27}\frac{\hat{u}^2}{\hat{s}\hat{t}}$
$qq' \to q'\bar{q}'$	$\frac{4}{9}\frac{\hat{t}^2+\hat{u}^2}{\hat{s}^2}$
$qg \to qg$	$-\frac{4}{9}\frac{\hat{s}^2+\hat{u}^2}{\hat{s}\hat{u}}+\frac{\hat{s}^2+\hat{u}^2}{\hat{t}^2}$
$gg \to gg$	$\frac{2}{9}\left(3-\frac{\hat{t}\hat{u}}{\hat{s}^2}-\frac{\hat{s}\hat{u}}{\hat{t}^2}-\frac{\hat{s}\hat{t}}{\hat{u}^2}\right)$
$q\bar{q} \to gg$	$\frac{32}{27}\frac{\hat{t}^2+\hat{u}^2}{\hat{t}\hat{u}}-\frac{8}{3}\frac{\hat{t}^2+\hat{u}^2}{\hat{s}^2}$
$gg \to q\bar{q}$	$\frac{1}{6}\frac{\hat{t}^2+\hat{u}^2}{\hat{t}\hat{u}}-\frac{8}{3}\frac{\hat{t}^2+\hat{u}^2}{\hat{s}^2}$

parton systems are given in terms of the observed rapidities by

$$y^* = (y_3 - y_4)/2\,, \qquad \bar{y} = (y_3 + y_4)/2 \tag{1.27}$$

For a massless parton the center of mass scattering angle θ^* can be written as

$$cos\theta^* = \frac{P_Z^*}{E^*} = \frac{sinhy^*}{coshy^*} = tanhy^* = tanh\left(\frac{y_3 - y_4}{2}\right) \tag{1.28}$$

and x_1, x_2 are the momentum fractions of the interacting partons given as

$$x_1 = x_T e^{\hat{y}} coshy^*, \quad x_2 = x_T e^{-\hat{y}} coshy^*, \ \hat{y} = \frac{1}{2} ln\left(\frac{x_1}{x_2}\right) \tag{1.29}$$

For massless partons, the Mandelstam variables satisfy the relations are written as follows;

$$\hat{t} = -\frac{1}{2}\hat{s}(1 - cos\theta^*), \quad \hat{u} = -\frac{1}{2}\hat{s}(1 + cos\theta^*) \tag{1.30}$$

where $\hat{t}$ and $\hat{u}$ as a function of $\hat{s}$ and the center of mass scattering angle. Pseudorapidity and rapidity are identical with neglecting parton masses and determined by the following equation.

$$y = -log\left(tan\frac{\theta}{2}\right) \tag{1.31}$$

1.1.5. Dijet Resonances Models

The SM of quarks and leptons and their weak, strong and electromagnetic interactions is a theory that successfully describes a wide range of phenomena in particle physics. Although it's extraordinary success, the theory leaves many questions unanswered, such as: Why do quarks come in different flavors? How to combine gravity with other forces? Why are there four different forces? Why is gravity so weak? …etc

In order to answer such questions that the SM can not explain, many theories have been developed beyond SM, and most of these theories predict the existence of extremely short-lived resonance particles. These new particles can have high interactivity constants with quarks and gluons and in the latter case can be decomposed into two partons that will take place two high-energy jets. This phenomenon is called dijet resonance. These particles are produced as narrow resonances, X, decaying to dijet as shown in Fig. 1.11. The initial state and final state both contain two partons (quarks, antiquarks or gluons) and the intermediate state contains an s-channel resonance X. The properties of the models which are considered in this study are summarized in Table 1.4.

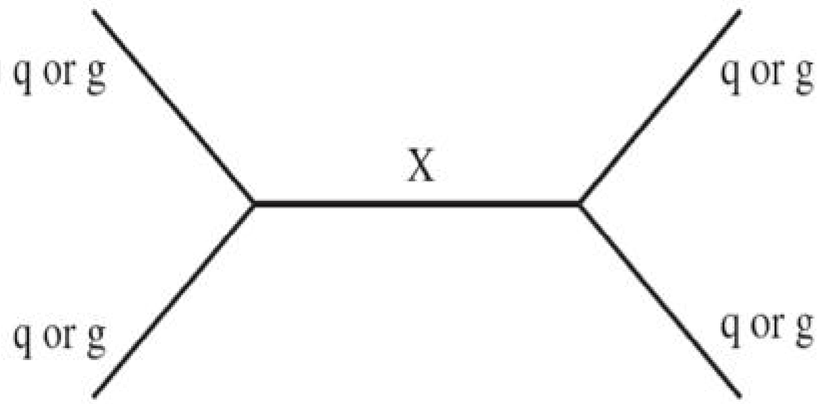

Figure 1.11. Feynman diagram of dijet resonance

Table 1.4. Summary of resonances considered in this study

Model Name	Symbol	Color Multiplet	J^P	$\Gamma/(2M_R)$	Decay Channel
Excited Quark	q^*	Triplet	$1/2^+$	0.02	*qg*
E_6 Diquark	D	Triplet	0^+	0.004	*ud*
Axigluon	A	Octet	1^+	0.05	$q\bar{q}$
Coloron	C	Octet	1^-	0.05	$q\bar{q}$
Color Octet Scalar	S_8	Octet	0^+	0.04	*gg*
Heavy W	W'	Singlet	1^-	0.01	$q_1\bar{q}_2$
Heavy Z	Z'	Singlet	1^-	0.01	$q\bar{q}$
RS Graviton	G	Singlet	2^+	0.01	$q\bar{q}$,*gg*
String	S	various	various	0.003 – 0.037	$q\bar{q}$,*qg*,*gg*

1.1.5.1. Excited Quarks

According to the various theoretical models, ordinary quarks can be composite objects. And if quarks are composite particles then as a natural consequence, excited states are expected. This phenomenon is called simply ***excited quarks*** and indicated by q^*. Depending on the details of the composite models, values of spin and isospin of the excited quark can have various values (Baur et al., 1987 and 1990). In the simplest case, spin and isospin of the excited quark are set to 1/2 to limit the number of parameters at hadron colliders. The assignment of right and left-handed components to isodoublets for the first generation,

$$\begin{bmatrix} u \\ d \end{bmatrix}_L, \begin{matrix} u_R \\ d_R \end{matrix} \begin{bmatrix} u^* \\ d^* \end{bmatrix}_L, \begin{bmatrix} u^* \\ d^* \end{bmatrix}_R \tag{1.32}$$

allows to non-zero masses prior to *SU(2)* × *U(1)* symmetry breaking. The coupling of excited fermion states f^* to gluons, γ, $W^{\pm}$ and Z is given by the Lagrangian (Baur, 1990).

$$\mathscr{L}_{gauge} = \bar{f}^{*}\gamma^{\mu}\left[\mathrm{g}_{s}\frac{\lambda^{a}}{2}G_{\mu}^{a} + \mathrm{g}\frac{\tau}{2}W_{\mu} + \mathrm{g}'\frac{Y}{2}B_{\mu}\right]f^{*} \quad (1.33)$$

The weak hypercharge γ of the excited states in the lepton and quark sector are −1 and 1/3 respectively; g_s, $\mathrm{g} = e/sin\theta_W$ and $\mathrm{g}' = e/cos\theta_W$ are the strong and electroweak gauge couplings. G_{μ}^{a}, W_{μ} and B_{μ} describe the gluon, *SU(2)* and *U(1)* gauge fields. Additionally, gauge bosons can also mediate to the transitions between right-handed (excited) and left-handed (ordinary) fermions. The form of the effective Lagrangian describing these transitions is uniquely fixed by gauge invariance to be of magnetic-moment type

$$\mathscr{L}_{trans} = \frac{1}{2\Lambda}\bar{f}^{*}R^{\sigma^{\mu\nu}}\left[\mathrm{g}_{s}f_{s}\frac{\lambda^{a}}{2}G_{\mu\nu}^{a} + \mathrm{g}f\frac{\tau}{2}W_{\mu\nu} + \mathrm{g}'f'\frac{Y}{2}B_{\mu\nu}\right]f_{L} + h.c \quad (1.34)$$

where λ^{a} and τ are the generators of the color $SU(3)$ and isospin $SU(2)$, $G_{\mu\nu}^{a}$, $W_{\mu\nu}$ and $B_{\mu\nu}$ are the field-strength tensor of the gluons, *SU(2)* and the *U(1)* gauge fields. g_s,g,g' are the gauge couplings, f_s, f, and f' are parameters determined by composite dynamics. For a pure strong interaction these will be set to 1. Λ is the composite scale.

In proton-proton collisions, the production of an excited quark occurs through the quark-gluon fusion. Excited quark would then decays to a quark and a gauge boson (γ, g, W, Z). The most common decay channel is $q^{*} \rightarrow q\mathrm{g}$, appear as resonances in the invariant mass distribution of the decay products. For the decay of excited quark (q^{*}) with mass m^{*} into quark and gluons the partial width is given by (Baur, 1990)

$$\Gamma(q^{*} \rightarrow q\mathrm{g}) = \frac{1}{3}\alpha_{s}f_{s}^{2}\frac{{m^{*}}^{3}}{\Lambda^{2}} \quad (1.35)$$

According to the Eq. (1.35) excited quarks (q^*) decompose predominantly via strong interactions into ordinary quarks and a gluon.

Gluonic excitation, which is one of the many ways of produce excited quarks in the proton-proton collision, has a large branching ratio (Table 1.5) and will produce a peak in the dijet spectrum. The cross section for gluonic excitation of quarks can be given by (Baur, 1990)

Table 1.5. Branching ratios for u^* and d^* (Baur, 1990)

Decay Mode	B.R.(B_G)
$u^* \rightarrow ug$	0.85
$u^* \rightarrow u\gamma$	0.02
$u^* \rightarrow uZ$	0.03
$u^* \rightarrow dW$	0.10
$d^* \rightarrow dg$	0.85
$d^* \rightarrow d\gamma$	0.005
$d^* \rightarrow dZ$	0.05
$d^* \rightarrow uW$	0.10

$$\sigma = \frac{\alpha_s \pi^2}{3\Lambda^2} f_s^2 \tau \frac{d\mathscr{L}^q g}{d\tau} \tag{1.36}$$

with

$$\tau = \frac{{m^*}^2}{s} \tag{1.37}$$

where s is the center-of-mass energy squared and $d\mathscr{L}^q g/d\tau$ indicate the quark-gluon luminosity. If gauge interactions are dominating, the signals for singly produced excited quarks are the large transverse momentum of *jj*, *jγ*, *jZ*, or *jW* pairs with an invariant mass peaking at m^*. For simplicity Λ is identified with m^* and $f_s = f = f' = 1$.

1.1.5.2. E_6 Diquarks

E_6 models are well motivated extensions of the SM. Indeed, supersymmetric (SUSY) models based on the E_6 gauge symmetry or its subgroup can originate from the ten-dimensional heterotic superstring theory (Green, 1987). Within this framework gauge and gravitational anomaly cancellation was found to take place for the gauge group $E_8 \times E_8$. Some models for the compactification of the additional six dimensions, predict that the grand unification symmetry group is E_6 (Candelas, 1985). E_6 models include color-triplet scalar diquarks (Hewett and Rizzo, 1989), D^c and D with charges 1/3 and −1/3 and spins 0 and 1/2 respectively, which couple to the light quarks u,d (Hewett, 1989).

The interaction Lagrangian between the E_6 diquark model the light quarks is given by (Katsilieris, 1992)

$$\mathscr{L}_D = \lambda \mathcal{E}_{ijk} \hat{u}^{ci} \frac{1}{2}(1-\gamma_5) d^j D^k + \frac{1}{2} \lambda_c \mathcal{E}_{ijk} \hat{u}^i \frac{1}{2}(1-\gamma_5) d^{cj} D^{ck} + h.c \quad (1.38)$$

where λ and λ_c are parameters of the hyper-potential of the general E_6 model which are expected to be reasonably small in order to keep the higher order correction under control. i, j and k are color indices. The squared amplitudes $|M|^2$ for the diquark decays of D and D^c to quark pairs are given by (Angelopoulos, 1986)

$$\left|M(D \to \bar{u}\bar{d})\right|^2 = 24\lambda^2 m_D^2,\ |M(D^c \to ud)|^2 = 6\lambda_c^2 m_{Dc}^2 \quad (1.39)$$

The widths corresponding to D and D^c can be written as

$$\Gamma_D = \alpha_\lambda M_D,\ \Gamma_{D^c} = \frac{1}{4} \alpha_{\lambda_c} M_{D^c} \quad (1.40)$$

where $\alpha_\lambda = \lambda^2/4\pi$, $\alpha_{\lambda_c} = \lambda_c^2/4\pi$

1.1.5.3. Axigluons

In chiral color models (Pati, 1975, Frampton, 1987, Bagger, 1988) where the SM color group have been extended to $SU(3)_L \times SU(3)_R$, and which at some energy, the symmetry breaking to the diagonal *SU(3)$_C$* generates the massive axigluon (Frampton and Glashow, 1987), which couples to quarks with a pure axial-vector structure and the same strength as QCD (Paola, 2009). There are many different implementations of chiral color, and all require new particles in varying representations of the gauge groups. The most important model-independent prediction of chiral color is a massive color octet of gauge bosons, the axigluon (Bagger, 1988). The axigluon (Chivukula, 2013) decay to fermions and it has a strong gauge coupling to all quark flavours according to the following interaction Lagrangian (Katsilieris, 1992)

$$\mathscr{L}_{\mathrm{A}} = -i\mathrm{g}_s t^a_{ij}\hat{q}^i\gamma_5\gamma_\mu A^{\mu a}q^j \qquad (1.41)$$

where $\mathrm{g}_s = \sqrt{4\pi\alpha_s}$, t^a_{ij} are the usual *SU(3)* color matrices and $A^{\mu a}$ is the axigluon field. Axigluons can decay to quark-antiquark (fermions) pairs, but note that because of parity conservation, the axigluon cannot decay to a gluon-gluon pair (all gluon-axigluon vertices should contain equal number of axigluons). The width of the axigluon decay is given by

$$\Gamma_A = \frac{N\alpha_s M_A}{6} \qquad (1.42)$$

where M_A is mass of the axigluon, α_s is QCD coupling constant and N refers to the open decay channels which ranges from 6 for known quarks up to 18 for all particles.

The matrix element squared ($|M|^2$) averaged over initial and summed over final spins and color is given by for the axigluon production

$$< |M(q\hat{q} \to A)|^2 > = \frac{16}{9}\pi\alpha_s(Q^2)m_A^2 \tag{1.43}$$

The branching ratio of the axigluon into two-jets includes a correction owing to the top quark. If $M_A < 2M_t$, then the branching ratio to light quarks (u, d, s, c, b) is 1, and if $M_A > 2M_t$, then the branching ratio is given by

$$BR(A \to q\hat{q}) = \frac{1}{5+[1-(2M_t/M_A)^2]^{3/2}} \tag{1.44}$$

1.1.5.4. Colorons

The Colorons (Chivukula, 2013, and Simmons, 1997), like axial color models, have other possibilities for enriching the strong sector of the group structure. This model is the flavor-universal coloron (Chivukula, 1986) that the gauge group expands to $SU(3)_1 \times SU(3)_2$. The suitable gauge couplings defined as ξ_1 and ξ_2 with $\xi_1 \ll \xi_2$. However, the model contains a scalar boson Φ that breaks down the symmetry of the two groups, developing a vacuum expectation that is different from zero. The diagonal sub-group is defined as the color group to which the QCD is familiar and its remains unbroken. The original gauge bosons are combined to form an octet of massless gluons and form an octet of massive colorons. The mass of colorons defined as a function of the basic parameters (Simmons, 1997):

$$M_C = \left(\frac{g_s}{sin\theta cos\theta}\right)f \tag{1.45}$$

where θ is the gauge boson mixing angle with $cot\theta = \frac{\xi_2}{\xi_1}$, and f is the vacuum expectation value of the scalar field. The Lagrangian of the interaction between the quarks and the colorons field $C^{\mu a}$ is similar to QCD:

$$\mathscr{L} = -\mathrm{g}_s cot\theta\left(\sum_{ij} \bar{q}_i \gamma_\mu t_\alpha q_j\right) C^{\mu a} \tag{1.46}$$

The interaction, which is mentioned above, predicts the decay of quarks with kinematically allowed masses of colorons. The decay width can be shown as follow:

$$\Gamma_C \approx \frac{N}{6} \alpha_s cot^2\theta M_C, \tag{1.47}$$

where N is called the number of quark flavors which mass less than $M_C/2$.

1.1.5.5. Color Octet Scalars

The bosonic states may be caused by gluon-gluon fusion, in some theoretical models. The color octet scalar model (S8) forms an example of exotic color resonances. The Lagrangian expression of the coupling of a color octet scalar (Han et al., 2010) field with gluons is given as followings:

$$\mathscr{L} = \mathrm{g}_s \frac{\kappa}{\Lambda} d^{abc} S_8^a G_{\mu\nu}^b G^{c,\mu\nu} \tag{1.48}$$

where g_s is the strong coupling constant, κ is the scalar coupling, Λ is the characteristic scale of the interaction, d^{abc} are the structural constants of the $SU(3)$ group and are described by the relation $\{t^a, t^b\} = \frac{1}{3}\delta^{ab} + d^{abc}t^c$, and S_8 is the color octet scalar field and $G_{\mu\nu}$is the gluon field tensor. The color octet scalar resonance width can be expressed as followings:

$$\Gamma = \frac{5}{6} \alpha_s \kappa^2 \frac{M^3}{\Lambda^2} \tag{1.49}$$

1.1.5.6. W′ and Z′

In the models where the symmetry $SU(2)_L \times U(1)_Y$ of the electro-weak SM sector is widening, new gauge bosons are emerging. Common features in these models are the presence of new gauge coupling constants and new gauge bosons, W' and Z', which are in the same order as the $SU(2)_L$ coupling of the SM. The cross sections of new gauge-bosons are calculated by scaling corresponding SM cross-sections with the acceptance of these particles couple to typical quarks and leptons are similar to SM model equivalents. Especially, the Fermi constant G_F becomes (Eichten, 1984):

$$G_F' = G_F \left(\frac{M}{M'}\right)^2 \tag{1.50}$$

where M is the masses of W or Z (Eichten et al., 1984) and M' is the masses of W′ or Z′.

1.1.5.7. Randall-Sundrum Gravitons

As a solution to the electro-weak vs Planck scale hierarchy problem the gravity model from Randall and Sundrum had been proposed (Randall, 1999 a and b) (RS). According to this model, the hierarchy is produced by an exponential function of the compactification radius of an extra dimension. The metric in the 5-dimensional space can be expressed as:

$$ds^2 = e^{-2kr_c\phi}\eta_{\mu\nu}x^\mu x^\nu + r_c^2 d\phi^2 \tag{1.51}$$

where ϕ is the extra dimension with compactification radius r_c, k is a constant of the same order and related to the 5-dimensional Planck scale M, and x^μ are the usual space-time dimensions. The reduced effective 4-D Planck scale $\overline{M}_{Pl}$ is given by:

$$\bar{M}_{Pl}^2 = \frac{M^3}{k}\left(1 - e^{-2kr_c\pi}\right) \tag{1.52}$$

According to the model, spin-2 gravitons appear as the Kaluza-Klein (KK) excitations of the gravitational field $h^{\mu\nu}$, whose coupling to the SM fields is given by the interaction Lagrangian (Davoudiasl, 2000):

$$\mathscr{L}_1 = -\frac{1}{\Lambda_\pi} h^{\mu\nu} T_{\mu\nu}, \tag{1.53}$$

with $T_{\mu\nu}$ being the energy-momentum tensor of the matter fields. The scale Λ_π and the mass m_n of the KK excitations may be written as a function of the basic constants of the theory as followings:

$$\Lambda_\pi = \bar{M}_{Pl} e^{-kr_c\pi}\ ,\ m_n = kx_n e^{-kr_c\pi} \tag{1.54}$$

For the matter-graviton interaction the coupling constant is the inverse of the scale Λ_π:

$$\mathrm{g} = \frac{1}{\Lambda_\pi} = x_n \frac{(k/\bar{M}_{Pl})}{m_n} \tag{1.55}$$

where x_n called as the n-th root of the the Bessel function of order 1. In fact, the phenomenological results of RS gravitons (Randall, 1999b) determines by their masses and the ratio $k/\bar{M}_{Pl}$. If the basic constants of this model satisfy a relation $kr_c \sim 12$, then $\Lambda_\pi \sim$TeV and RS gravitons can be generated in hadron collisions. RS-gravitons, through the graviton coupling to the matter fields, can decay to partons, leading to a dijet signature. The corresponding partial widths (Bijnens, 2001) for the first KK excitation are expressed as followings:

$$\Gamma(G \to \mathrm{gg}) = \frac{x_1^2}{10\pi}\left(\frac{k}{\bar{M}_{Pl}}\right)^2 m_1 \tag{1.56}$$

and

$$\Gamma(G \to \mathrm{q\bar{q}}) = \frac{3x_1^2}{160\pi}\left(\frac{k}{\bar{M}_{Pl}}\right)^2 m_1 \tag{1.57}$$

1.1.5.8. String Resonances

In the string theory (Anchordoqui et al., 2008; Cullen et al., 2000), particles are produced with mass M_s, by vibrations of relative strings, and they are populating the Regge trajectories, which are related to their masses and spins. Essentially, the mass of the basic strings is of the order of the Planck scale. In addition, it is reasonable that M_s lies in the TeV scale, in the theories with large extra dimensions. In this regards, Regge gluons and excited states of quarks take place in proton-proton collisions. If this string coupling is small, then the fundamental properties of the Regge excitations (production width and cross section) are independent of the model (compactification details are insignificant). This description is true just for parton scattering involving gluons, but four-quark scattering is only approximately true. The Regge excitations effects may be quantified (Anchordoqui et al., 2008; Cullen et al., 2000) through the presence of a common form factor in the 2-to-2 parton scattering amplitudes, which is denoted the *Veneziano form factor* and is written as follows in terms of the Γ-function:

$$V(\hat{s},\hat{t},\hat{u}) = \frac{\Gamma(1-\hat{s}/M_S^2)\Gamma(1-\hat{u}/M_S^2)}{\Gamma(1+\hat{t}/M_S^2)} \tag{1.58}$$

where $\hat{s},\hat{t},\hat{u}$ are the usual Mandelstam variables and these variables are constrained by $\hat{s} + \hat{t} + \hat{u} = 0$. The physical content of the Veneziano form factor appears with an expansion in terms of s-channel poles. Each of these poles is represented the virtual Regge resonance with mass $\sqrt{n}M_s$. For the aim of the resonances in the dijet spectrum, only the first-level (n = 1) excitation is concerned; however, the string mass M_s is the only free parameter. At the same time, the exact values of the cross sections depend on both spin values and color factors of the excited states.

The string resonance model has the largest cross section among the other models. The cross section is about 25 times larger than excited quark since it is there for all the processes: qg, gg, $q\bar{q}$ and $\bar{q}g$. The string resonance decays to qg (74%), $q\bar{q}$ (13%) and gg (13%).

1.1.5.9. Benchmark Models

Each of the above mentioned parton-parton resonance models appears to contain a limited number of free parameters (Harris and Kousouris, 2011). The experimental investigations consider benchmark models, with some parameter assumptions, used to set limits on the masses of the corresponding resonances. A brief summary of the Benchmark models is given below:

- Axigluons: The number of quark flavors that the axigluon can decay is set to the known number of quarks, N = 6.
- Colorons: the number of quark flavors that the coloron can decay and the gauge boson mixing angle are set to N = 6 and cotθ = 1, respectively.
- Excited quarks: SM couplings are considered $(f_s = f = f' = 1)$, compositeness scale is set equal to excited quark mass $\Lambda = M^*$.
- RS graviton: the ratio $k/\overline{M}_{Pl}$ is set equal to 1.
- W', Z': SM couplings are assumed.
- E_6 diquark: the electromagnetic coupling constants are considered equal $\alpha_\lambda = \alpha_{\lambda_C} = \alpha_e$.

- Color octet scalar: the gauge coupling and the characteristic scale of the interaction are set equal to the QCD coupling (κ = 1) and $\Lambda = M$ respectively.

Table 1.4, which we have already mentioned, summarizes the basic properties of the resonances discussed in this study. Especially, for the benchmark models the decay widths are approximate values, since they are also dependent on the running of the α_s, which must be evaluated at a scale equal to the resonance mass. The decay width for string resonances varies considerably depending on the spin and color quantum numbers of the resonances.

1.2. Experimental Apparatus

In this section, firstly general information about CERN is given. Then, information about the LHC accelerator will be given. We will finally discuss the details of both the CMS detector and its most important components with the aim of determining the content of the work.

1.2.1. CERN

The European Organization for Nuclear Research, known as CERN (Conseil Européen pour la Recherche Nucléaire), is where physicists and engineers are probing the fundamental structure of the universe. CERN is currently the largest particle physics laboratory of the world. CERN was founded on the September 29, 1954 and is located at the Switzerland-France border near Geneva. The experiments at CERN shed light on the understanding of basic particles and their interactions. Some of the historic properties are: the discovery of neutral currents in 1973, the discovery of the W and Z bosons in 1983, sensitive measurement of weak interactions in Large Electron Positron (LEP) experiments and investigation of a new state of matter known as the quark-gluon plasma. Moreover, it is also known for its social and cultural relevance. Researchers need remote access to these facilities, therefore the laboratory has historically been a major wide area network hub. In addition to this it is also the birthplace of the World Wide Web (www). Approximately 8,000 visiting scientists, half of the world's particle physicist, come to CERN for their research. It has 22 member states and includes 85 nationalities and 580 universities.

1.2.2. The Large Hadron Collider

The LHC is a 27 km long two-ring superconducting proton accelerator and collider located at CERN, spanning the border between the Jura Mountains situated in France and Lake Leman in Geneva in Switzerland. The LHC is the pinnacle of the accelerator complex at CERN, shown in the Fig. 1.12 and Fig. 1.13. It has the title of the most powerful and the largest accelerator built up to now in the world for High Energy Physics research and it is installed in the $e^{-}e^{+}$ collider LEP tunnel. The LEP tunnel was constructed between 1984 and 1989, 50-175 m below the ground, the radius of the ring approximately 4,3 km. The LHC was built by the European Laboratory to explore the Higgs boson, or the corresponding relic of the mechanism responsible for electroweak symmetry breaking, and search for particles which are predicted by beyond the Standard Model (BSM) theories at the TeV scale, like supersymmetric partners of the SM particles. After the September 2008 accident, the protons of the LHC were collided with 7 TeV center-of-mass energy in 2010 and 2011. In 2012, energy of the proton beam is increased by 1 TeV and protons are collided with 8 TeV center-of-mass energy. The protons of the LHC, which are collided at the center-of-mass energy of 13 TeV in 2016, exceeded the design value of instantaneous luminosity$10^{34}\mathrm{cm}^{-2}\mathrm{s}^{-1}$. Currently the proton-proton beams collide to discover new particles and to investigate new physics which can become visible on a mass scale of the order of 1 TeV at the center of mass energy $\sqrt{s}$ = 14 TeV, which was the design energy for LHC. In order to achieve luminosity of $10^{34}\mathrm{cm}^{-2}\mathrm{s}^{-1}$, the time differences between two proton bunches should be only 25 ns, in other words, the proton bunches are only be 7.5 m apart. There are 2808 proton-proton bunches per beam and nearly 10^{11} protons in each bunch (Fig. 1.14). Therefore, the LHC detectors have to have very fast readout electronics and trigger decisions.

The source of the protons to be accelerated is a bottle of compressed hydrogen gas. With the aid of an electric field, hydrogen atoms are stripped from their electrons, leaving behind a sample of pure protons. There are a number of existing machines that can be used to accelerate these protons to higher energies. The protons, which have been obtained with hydrogen gas, are increased to 50 MeV in a linear accelerator (Linac2), the first accelerator in the chain.

Figure 1.12. The Large Hadron Collider (LHC) at CERN in Geneva, at border of France and Switzerland

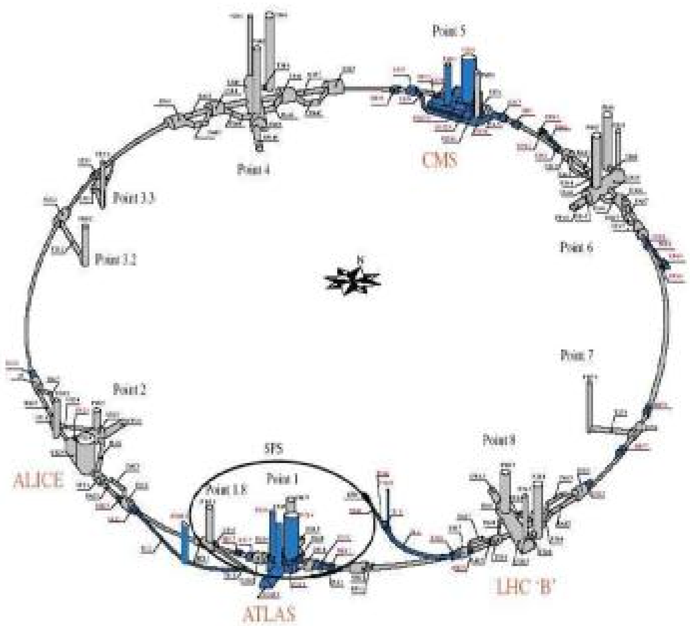

Figure 1.13. A schematic view of LHC Project with its detectors

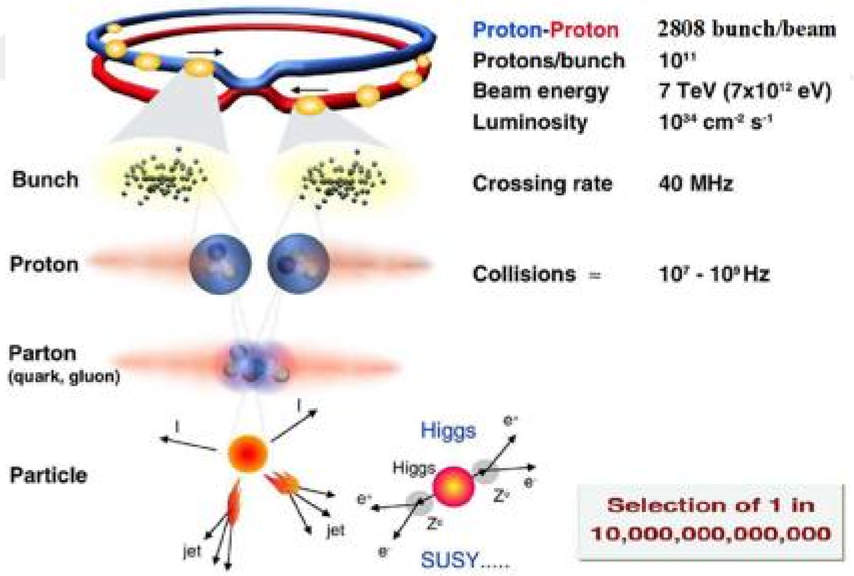

Figure 1.14. CERN LHC collision (Smith, 2008)

Then the beam is injected into the Proton Synchrotron Booster (PSB). The PSB accelerates the protons to energy of 1.4 GeV. Then the beam is sent to other ring of the chain, i.e. Proton Sinkrotron (PS). The PS accelerates the beam up to energy of 25 GeV. Subsequently, the protons are channeled to the Super Proton Synchrotron (SPS) where they accelerated up to 450 GeV. Finally the SPS injects these proton beams into the two beam pipes of the LHC (Fig. 1.15). These two beams move in the opposite direction, one in the clockwise and the other in the anticlockwise. Since the designed center of mass energy is $14\ \mathrm{TeV}$, each beam is accelerated maximaly up to 7 TeV energy and then directed to LHC's detectors for collision. The LHC is the last ring in a complex chain of particle accelerators. It is supplied with protons from the injector chain LINAC2 → Booster → PS → SPS (Bawa, 2007). A short summary of the accelerator chain and the corresponding proton beams energies in each of the different acceleration steps shown in Table 1.6.

There are four big experiment at the LHC: A Toroidal LHC Apparatus (ATLAS), A Large Ion Collider Experiment (ALICE), The CMS and the Large Hadron Collider beauty (LHCb).Two of these four detectors, ATLAS (Aad et al., 2008) and CMS (Chatrchyan et al., 2008a), are the general purpose experiments. The other two detectors, ALICE (Aamodt et al., 2008) and LHCb (Augusto Alves et al., 2008) focuse on more specific topics: heavy ion physics and Charge-Parity (CP) violation measurements, respectively.

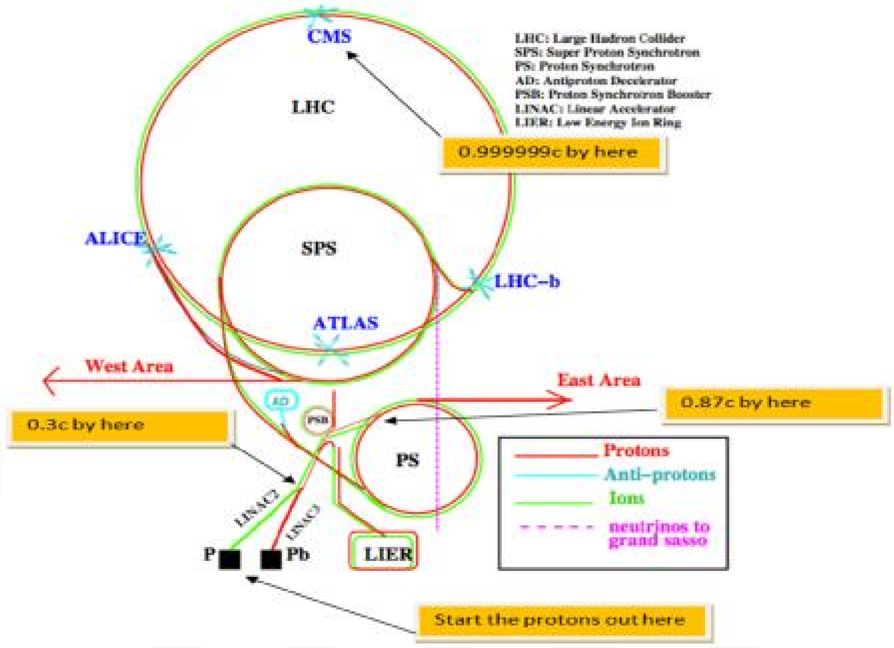

Figure 1.15. Overview of the Accelerator chain

Table 1.6. Accelerating steps (Scheurer, 2008)

Accelerator	Injection Energy	Final Energy
LINAC2	750 keV	50 MeV
PSB	50 MeV	1.4 GeV
PS	1.4 GeV	25 GeV
SPS	25 GeV	450 GeV
LHC	450 GeV	7 TeV

Due to the acceleration of particles having same electrical charge, are needed two different magnetic field configurations and two separate acceleration cavities. The LHC is constituted of 1232 super-conducting Niobium- Titanium dipole magnets, each of which is 30 tonnes and 14,2 m long, cooled up to 1.9 K (- 271.3°C) through 37 million kg super-fluid liquid Helium and create a bending magnetic field of about 8.33 Tesla. This magnetic field needed to keep to the proton beams on orbit during the acceleration in the LHC. Also there are 392 quadrupole magnets, which are used to keep the proton beams focused. The LHC dipole magnet scheme is shown in Fig. 1.16. The most important LHC parameters are listed in Table 1.8 (Bruning et al., 2004).

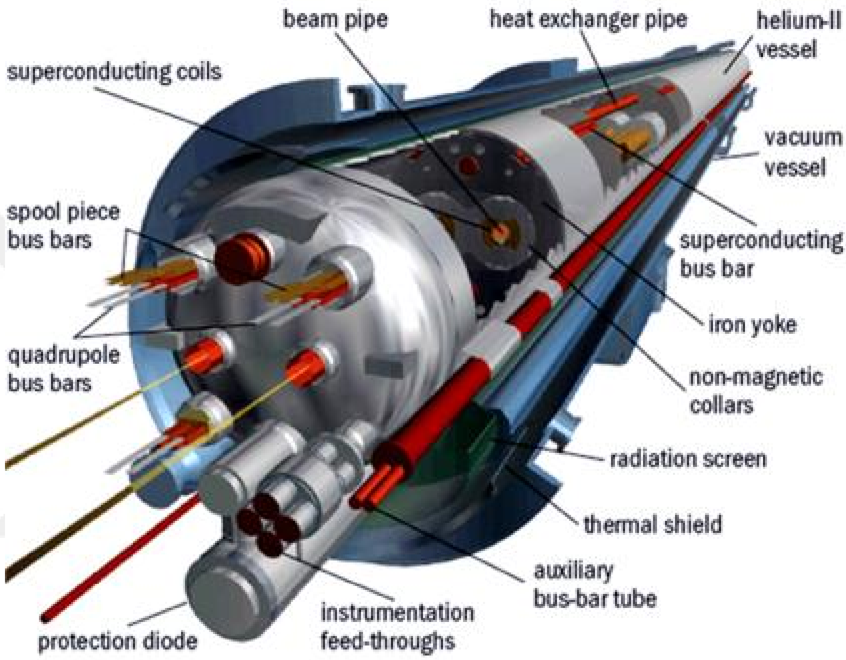

Figure 1.16. Picture of super-conducting dipole magnets installed at LHC (http://cerncourier.com/cws/article/cern/29723)

Table 1.7. Comparison between the LHC design and achived parameters in 2012, 2015, and 2016 respectively (IP1 is ATLAS and IP5 is CMS)

Parameter	**Design**	**Achieved (2012)**	**Achieved (2015)**	**Achieved (2016)**
Proton energy [GeV]	7000	4000	6500	6500
Relativistic gamma factor γ_r	7461	4263	6928	6928
Number of particles per bunch N_b	$1.15 \text{ x}10^{11}$	$1.6 - 1.7 \text{ x}10^{11}$	$1.15 \text{ x}10^{11}$	$1.3 \text{ x}10^{11}$
Number of bunches n_b	2808	1374	2244	2220
Bunch spacing [ns]	25	50	25	25
Transverse normalized emittance $\mathcal{E}_n$ [μm rad]	3.75	2.5	2.5	1.4
β^* at IP1 and IP5 [m]	0.55	0.6	0.8	0.4
Half crossing angle at IP1 and IP5 $\theta_c/2$[μrad]	±142.5	±145.0	±185.0	
Peak luminosity in IP1 and IP5 $[cm^{-1}s^{-1}]$	$1.0 \text{ x}10^{34}$	$7.7 \text{ x}10^{33}$	$5.2 \text{ x}10^{33}$	$1.3 \text{ x}10^{34}$
Max. mean number of events per bunch crossing	19	40	17	43

Table 1.8. Design parameters of the LHC (Bruning et al., 2004)

Parameter	Value	Unit
Momentum at Collision	7	TeV
Dipole field at 7 TeV	8.33	T
Quadrupole gradient	220	T/m
Circumference	26659	m
Design Luminosity	10^{34}	$cm^{-1}s^{-1}$
Number of bunches	2808	
Particles per bunch	$1.15\text{x}10^{11}$	
DC beam current	0.56	A
Stored energy per beam	362	MJ
Ultimate Dipole Field	9	T
Injection Dipole Field	0.4	T
Ramp Time	20	min
Magnet Coil inner diameter	56	mm
Distance between beams	194	mm

As is known, accelerated motion of charged particles result in an electromagnetic wave radiation. Therefore, protons emit radiation when circulating in a circular orbit in the LHC. And as a result, the proton beams lose energy. The maximum energy of the proton beams is limited by the amount of energy loss due to synchrotron radiation given by

$$-\Delta E = \frac{4\pi\alpha}{3r}\beta^3\gamma^4 \tag{1.59}$$

where r is the radius of accelerator, $\gamma = E/mc^2$ where m is mass of the accelerated particles and $\beta = v/c \approx 1$ because the particle velocity is close to the velocity of the light. The most effective way to increase center-of-mass energy is to increase the mass of accelerated particles. As is known, the mass of a proton is about 2000 times the mass of an electron. Therefore the energy loss due to synchrotron radiation for protons will decreased by a factor of $(2000)^4 \approx 10^{13}$ compared to electrons.

Protons are not elementary particles and they are composed out of partons (quarks and gluons). Because of these sub-structures, proton-proton collisions phenomenologies are very different from lepton collisions. So that the quarks and gluons, which are the components of the proton, interact with only a fraction of the proton energy given by

$$\sqrt{\hat{s}} = \sqrt{x_1 x_2 s} \tag{1.60}$$

where, whereas $\sqrt{\hat{s}}$ is the effective center-of-mass energy of the hard scattering, $\sqrt{s}$ is center-of-mass energy of the proton beams, x_1 and x_2 refer to the energy-fractions carried by the interacting partons. Thus, the center of mass energy must be greater when compared to an electron-electron machine. Each collision will lead to a different type of event determined by the cross section of possible interactions because the fraction of momentum carried by interacting partons will be different. The total cross section for the colliding partons (hard scattering) is given by Eq. 1.21. The cross section and the event rate at the LHC design luminosity for different processes as a function of the center-of-mass energy $\sqrt{s}$ is illustrated in Fig. 1.17.

In LHC collisions, the number of events generated per seconds is given by:

$$N_{event} = L\sigma_{event} \tag{1.61}$$

where σ_{event} is the cross section and L is luminosity, $L = \int L(t)dt$. It is clear that high luminosity is needed to observe interesting rare physics events, such as the Higgs boson production, which have small cross sections.

The luminosity depends only on the beam parameters and can be written for a Gaussian beam distribution as (Evans, 2008):

$$L = \frac{N_b^2 n_b f_{rev} \gamma_r}{4\pi \varepsilon_n \beta^*} F \qquad (1.62)$$

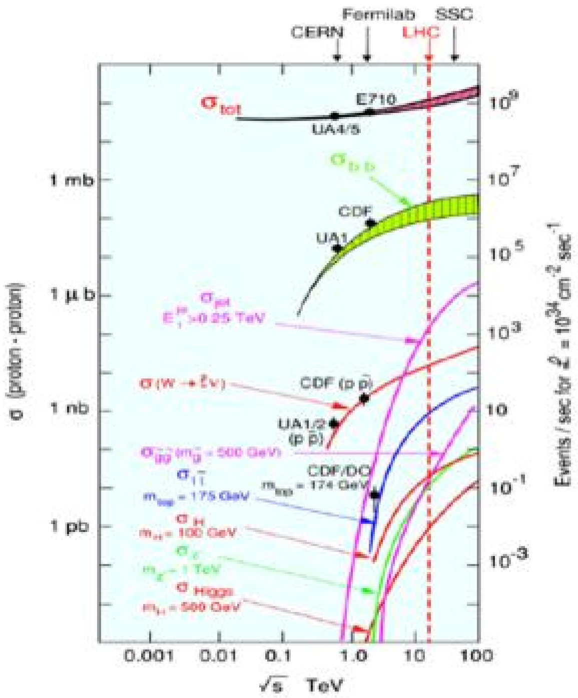

Figure 1.17. Hadronic cross sections and event rates for different physics processes as a function of the centre-of-mass energy $\sqrt{s}$ at proton-proton colliders (Bayatian et al., 2000)

where N_b is the number of particles per bunch, n_b is the number of bunches per beam, f_{rev} is the revolution frequency, γ_r is the relativistic gamma factor, ε_n is the normalized transverse beam emittance, β^* is the beta function at the collision point, and F is the geometric luminosity reduction factor due to the crossing angle at the interaction point (IP):

$$F = \left(1 + \left(\frac{\theta_c \sigma_Z}{2\sigma^*}\right)^2\right)^{-1/2} \tag{1.63}$$

where θ_c is the full crossing angle, σ_Z is the RMS bunch length, and σ^* is the RMS beam size at the IP.

The integrated luminosity of proton-proton collisions delivered by the LHC to the CMS experiment versus the time between 2010 and 2016 years is given by Fig. 1.18. This is shown for 2010 (green), 2011 (red), 2012 (blue), 2015 (purple), and 2016 (orange) data-taking (CMS Collaboration, 2013a). Also, the LHC provides lead-proton and lead-lead collisions for experiments for one month each year.

1.2.3. The Compact Muon Solenoid

The Compact Muon Solenoid (CMS) (Chatrchyan et al., 2008a) detector is a multi-purpose apparatus used to explore the physics at the TeV scale due to proton-proton, lead-lead, and proton-lead collisions provided by the LHC at CERN. It is located at Point5 of the LHC near Cessy, France. The CMS detector contains different subsystems that can measure the energy and momentum of particles such as electrons, photons, tauses, muons, and hadrons. It has many goals such as the searches for physics beyond the SM, the search for the Higgs boson, the precision measurements of already known particles and phenomena. CMS is the heaviest detector at the LHC and has 21.5 m length, a diameter of 14.6 m and weight of about 14000 tonnes which is about twice the weight of ATLAS detector. A schematic view of the CMS detector in Fig. 1.19 shows all of these subdetectors. From the interaction point, the incoming particles encounter the following subdetectors, respectively.

- the tracking system,
- the electromagnetic calorimeter,

- the hadronic calorimeter,
- the return yoke of the superconductive magnet (this is not a “sub-detector”, but acts also as a filter, allowing only muons and weakly interacting particles such as neutrinos to pass through and access the muon chambers),
- the muon system.

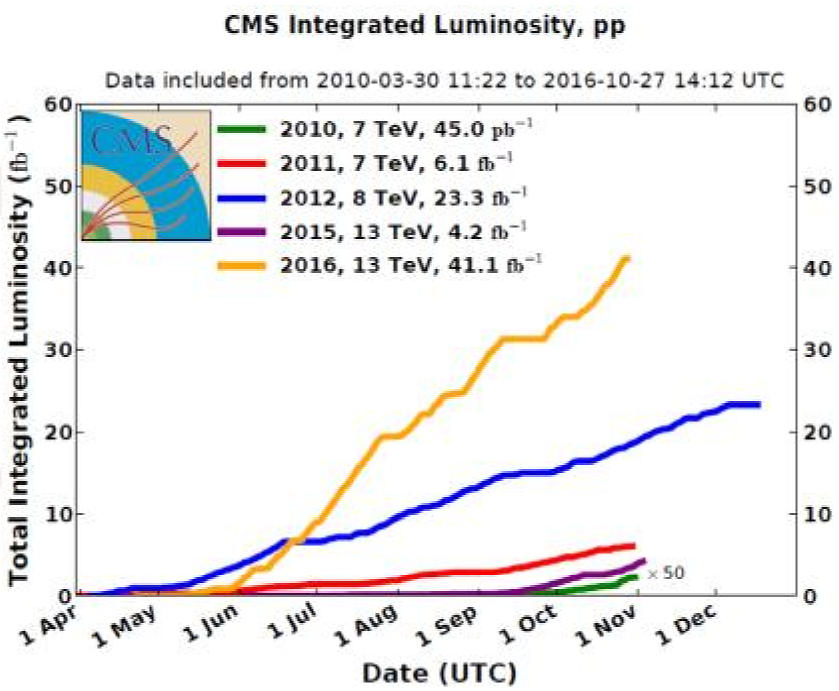

Figure 1.18. Cumulative luminosity versus day delivered to CMS during stable beams for pp collisions

The CMS detector requirements for the goals of the LHC physics programme can be summarized as following (Chatrchyan et al., 2008a):

- Good charged particle momentum resolution and reconstruction efficiency in the inner tracker part and high granularity especially near the interaction point,

- Good electromagnetic energy resolution, wide geometric coverage, efficient photon and lepton isolation at high luminosities,
- Hadron calorimeters with hermetic coverage, with optimal missing transverse energy and dijet mass resolution,
- Good muon definition, charge determination and momentum resolution over a wide range of momenta and angles.

The design of the CMS detector is similar to the structure of the onion. This detector consists of several layers each of which is extremely sensitive to measure and identify classes of particles. In the innermost part of CMS there is the silicon tracking detector, which measures the momentum of charged particles in the magnetic field. This silicon tracker is covered by the electromagnetic calorimeter measuring the energy of electrons and photons. Behind the electromagnetic calorimeter there is the hadron calorimeter that records energy of strongly interacting particles. And then there is the bobbin of the superconducting solenoid magnet, which is also covers the previous subdetectors. At the outermost part of the CMS there are four stations of the muon chambers, which are embedded in the iron yoke of the magnet. Each muon station consists of several layers of aluminum drift tubes (DT) in the barrel region and cathode strip chambers (CSC) in the endcap region, which are completed by resistive plate chambers (RPC). Fig. 1.20 shows the trajectories of different particles as they pass through the detector. In the following sections, the CMS coordinate frame and each sub-detector corresponding to CMS detector layers are briefly discussed.

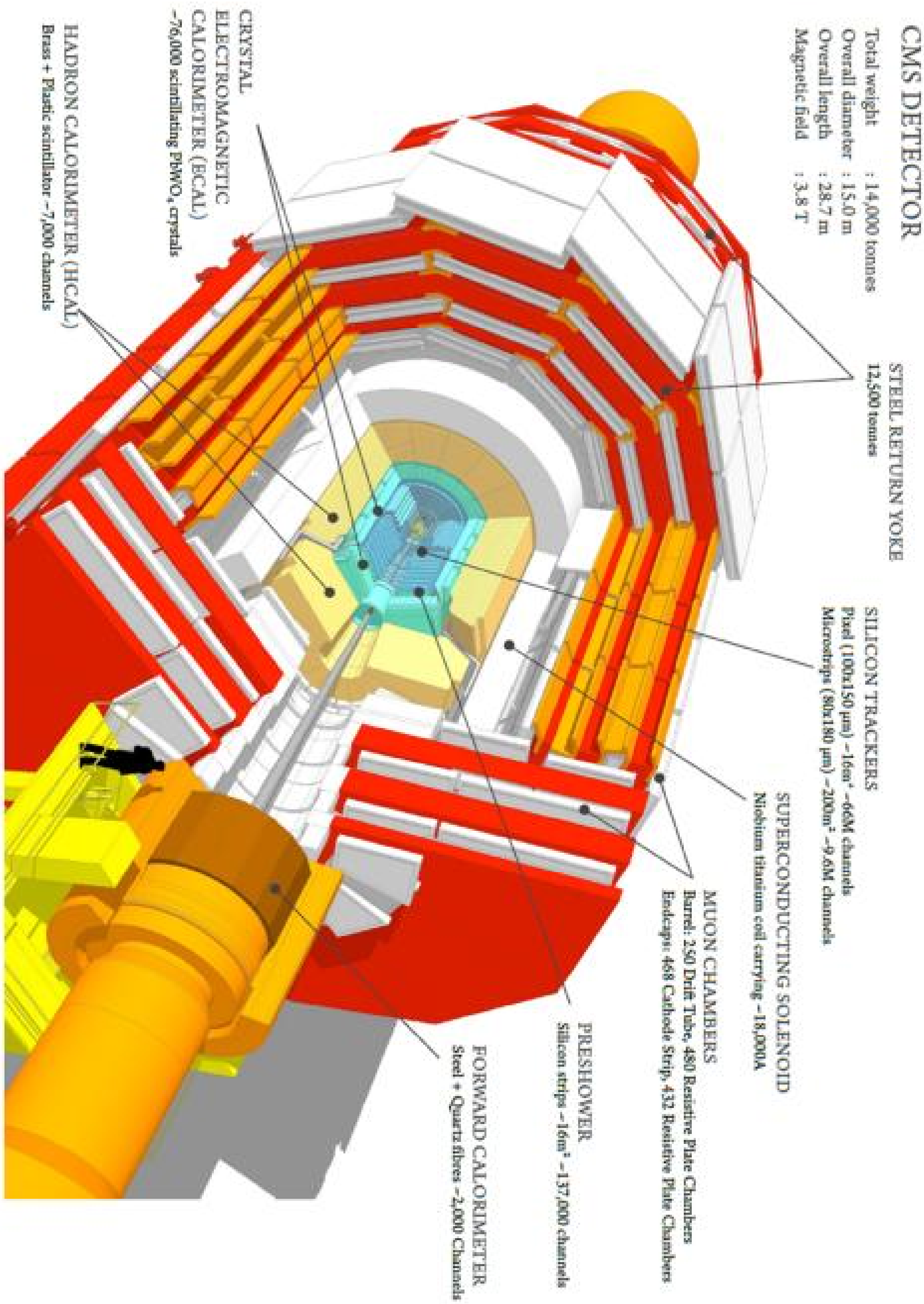

Figure 1.19. A full view of Inner structure of the CMS detector

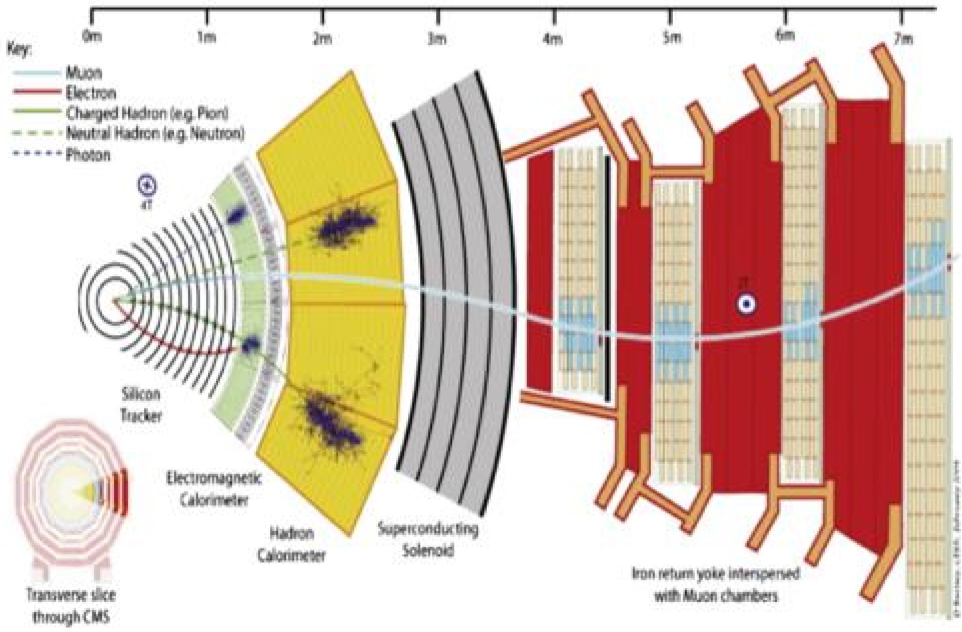

Figure 1.20. Transverse slice of the CMS detector and particles traces in different subdetectors (Lazaridis, 2011)

1.2.3.1. The CMS Coordinate Frame

The CMS uses a right-handed cartesian coordinate system; the origin is located at the nominal interaction point in the center of the detector. In the coordinate system of the CMS, the *y*-axis points vertically upward, the *x*-axis points to the center of the LHC ring radially and the z-axis along the anticlockwise-beam direction, namely the *z* axis is parallel to the beam line. The CMS coordinate system is illustrated in Fig. 1.21. If the cylindrical system is taken into consideration, it also would be useful to define some variables in the angular reference system. The polar angle, θ, is measured from the positive z-axis and the azimuthal angle, which is lies in the x-y plane and denoted by Φ.

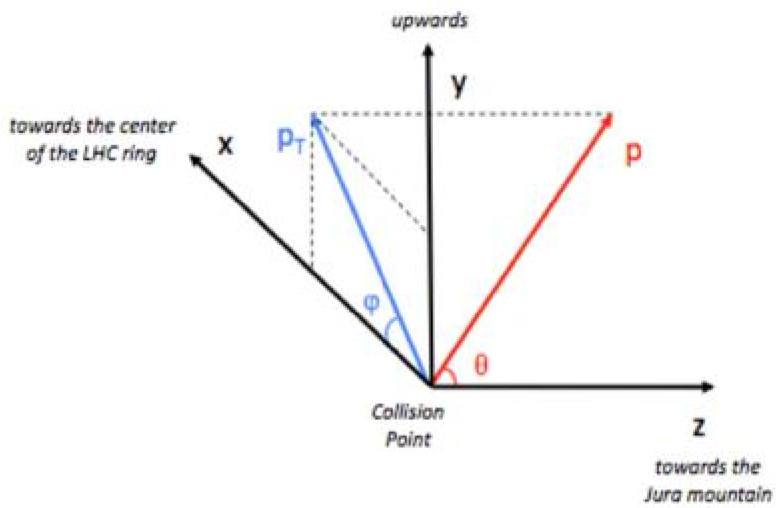

Figure 1.21. The CMS coordinate system (Martelli, 2012)

The transverse energy and the transverse momentum (denoted respectively by E_T and P_T), which represent the energies and momentums of particles in the transverse plane, are defined as $E_T = Esin(\theta)$ and $P_T = Psin(\theta)$.

A variable commonly used in hadron collisions is ***pseudorapidity (η)*** and is defined as:

$$\eta = -\ln tan\frac{\theta}{2} \quad (1.64)$$

The pseudorapidity, as a function of three-momentum ***p*** can be written as:

$$\eta = \frac{1}{2}ln\left(\frac{|p|+p_L}{|p|-p_L}\right) = \text{arctanh}\left(\frac{p_L}{|p|}\right) \quad (1.65)$$

where p_L is the component of the momentum trough the beam axis. The pseudorapidity can be rewritten as a function of the θ and looking at Eq. 1.66 it is zero for $\theta = \pi/2$ (central part of the detector), and ±inf for $\theta = 0, \pi$. It is shown in

Fig. 1.22. The angle of $\theta = 0$ is in the axis of the beam, which lies on the horizontal line and corresponds to $\eta = \infty$.

$$\eta = -\ln tan\frac{\theta}{2} \tag{1.66}$$

At the limit where the particle velocity is close to the speed of light, in which case the mass of the particle is insignificant, one can make the substitution $m \ll p \Rightarrow E \approx P \Rightarrow \eta \approx y$, and therefore the defination of the pseudorapidity converges to the definition of rapidity used in experimental particle physics:

$$y = \frac{1}{2} ln\left(\frac{E+P_L}{E-P_L}\right) \tag{1.67}$$

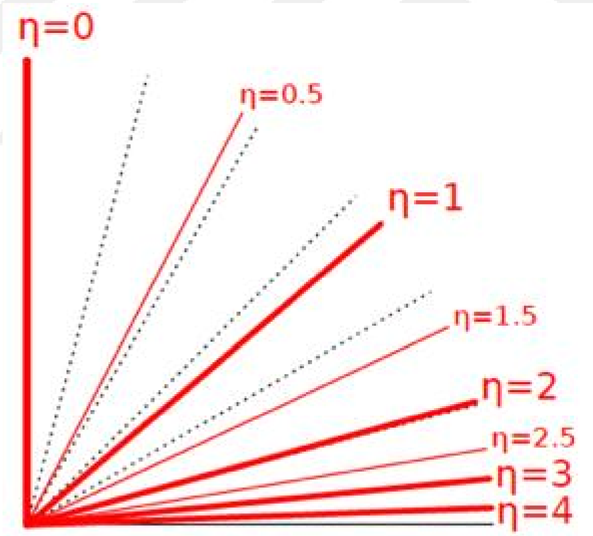

Figure 1.22. Pseudorapidity values illustrate on a polar plot

The pseudorapidity does not depend to the longitudinal component of the momentum p_L which is generally unknown for the colliding partons. Then it is advantage to use it.

Also, in high energy approximation intervals of the pseudorapidity do not change with Lorentz boosts, as for rapidity, along the beam direction. The Lorentz invariant angular distance, $\Delta\eta$, can also be written as a function of the scattering angle θ^{*}:

$$cos\theta^{*} = tanh\left(\frac{\Delta\eta}{2}\right) \tag{1.68}$$

The angular separation, $\Delta R^{2} = (\Delta\eta)^{2} + (\Delta\Phi)^{2}$, which is the Lorentz-invariant can also be defined using the pseudorapidity.

1.2.3.2. The Tracker

The main requirements of the inner tracking system of the CMS detector are to provide a precise measurement of the trajectories of charged particles coming from the interaction point, and also precise reconstruction of secondary vertices. The design goal of the central tracking system is to reconstruct the paths of isolated high-energy muons, electrons and charged hadrons with an efficiency better than 95%, and tracks of particles within jets with efficiency greater than 90%, within a pseudorapidity coverage of $|\eta| < 2.5$, as well as to see tracks coming from the decay of very short-lived particles such as b-quark, with high momentum resolution and efficiency. It provides absolute, efficient measurement of charged particles trajectories coming from the interaction points. However, the tracker is the closest sub-detector to the beam axis where the collisions take place. A homogeneous 4 T magnetic field is provided by the CMS solenoid, over the full volume of the tracker.

A schematic drawing of the CMS tracker system is given in Fig. 1.23. Each line represents a detector module. Double lines indicate back-to-back modules (Chatrchyan et al., 2008a). The length and diameter of the tracker, which surrounds the interaction point and is a cylindric structure, is 5.8 m and 2.5 m, respectively. At LHC luminosity of $10^{34}\mathrm{cm}^{-2}\mathrm{s}^{-1}$ approximately 1000 particles will be created for each bunch crossing that occur every 25 ns. Hence, the tracker detector is expected to have high granularity and fast response. In addition, due to the fact that the large number of particles occurs at each collision, the tracking system is exposed to severe radiation. The inner tracking system consists of two main silicon sub-detectors. The first one, the pixel detector as the innermost structure, comprises of 3 barrel layers at a radius between 4.4 cm and 10.2 cm. The second detector is the strip tracker with 10 barrel detection layers extending outwards to a radius of 1.1 m. Each system is completed by endcaps, which consist of 2 pixel layers in the pixel detector, 3 inner and 9 outer forward disks.

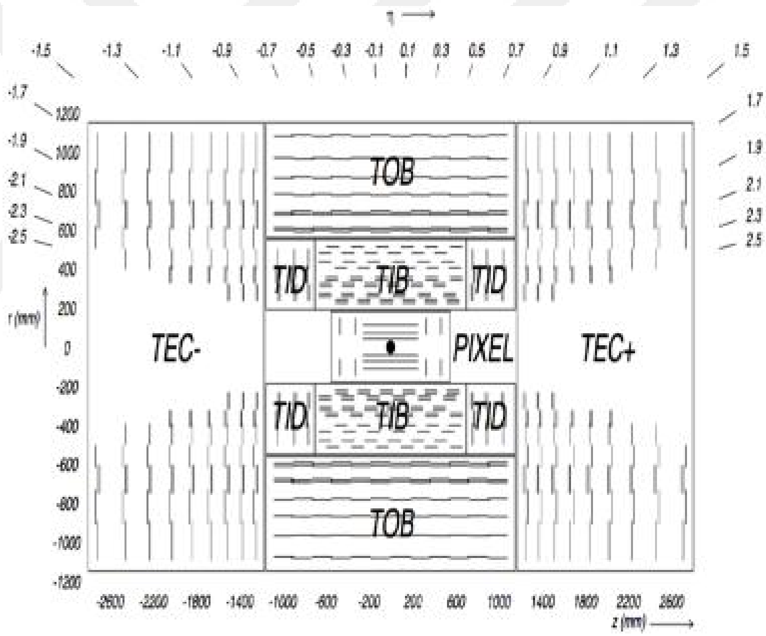

Figure 1.23. Schematic cross section through the CMS tracker

The Tracker Inner Barrel (TIB) and the Tracker Inner Disk (TID) extends up to a radius of 55 cm and consists of 4 barrel layers that supplemented by 3 disks at each end. The Tracker End Caps (TEC) covers the region 22.5 < |r| < 113.5 cm and they are consisting of 9 disks. The outer radius of the Tracker Outher Barel (TOB) is 116 cm and consists of 6 barrels. For high momentum muon tracks

(100 GeV), the transverse momentum resolution is about 1-2% in the central region $|\eta|$=1.6, beyond that the transverse momentum resolution is degrades because of the reduced lever arm.

In the following section, some information is given about the pixel detectors at the very core of the detector dealing with the highest intensity of particles and the silicon microstrip detectors that surround it.

1.2.3.2.(1). The Pixel Detectors

The Pixel Detector is the closest part of the tracking system to the collison point. Precise tracking points in the 3D space with a spatial resolution in the range of 15-20 μm are provided by this detector and it is required for accurately reconstruction of the charged track. It has an ability to determine the impact parameters of the charged particles due to its high position resolution. In addition, reconstruction of the secondary vertices in three dimensions allows efficient identification of b and τ-jets. It consists of three barrel layers (BPix), which has two end cap disks (FPix) on each side of them. The three barrel layers, BPix, are located at mean radii of 4.4 cm, 7.3 cm, respectively and 10.2 cm, and have a length of 53 cm. The two end cap disks, FPix, are extending from 6 to 15 cm in radius and are placed on each side at |z| = 34.5 cm and |z| = 46.5 cm from the interaction point. The spatial resolution is about 15-20 µm for the z-direction and 10 µm for measurements in the r-Q plane, and each pixel is $125 \times 125\ \mu m^2$. The pixel detector covers a pseudorapitiy range $|\eta|$=2.5, matching the acceptance of the central tracker as seen in Fig. 1.24. All the pixel system consists of about 1440 pieces of silicon modules with a total of 66 million readout channels allowing it to track the paths of particles emerging from the LHC collision.

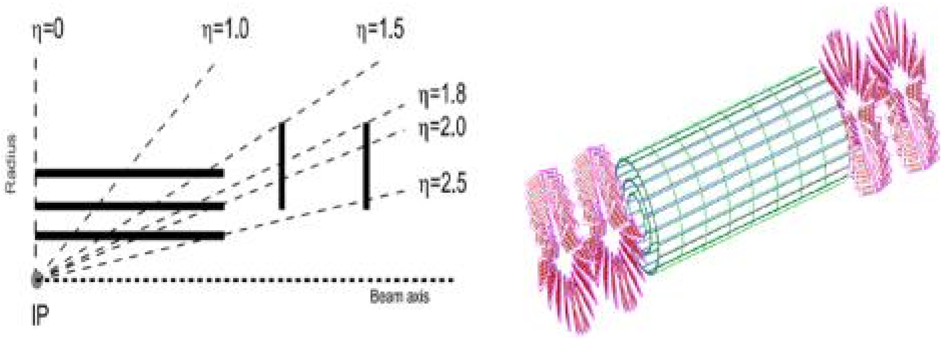

Figure 1.24. Geometrical layout of the Pixel detector (Bayatian et al., 2006)

There is a very high track rate and particle fluences around the interaction point so pixel detector needs to have a radiation tolerant design. A *n*+ pixel on the *n*-substrate detector design allows it to work even at very high particle flows. Because of the high radiation environment in the CMS, pixel detectors should be replaced throughout the experiment period.

1.2.3.2.(2). The Silicon Strip Detectors

The silicon strip detector is a subdetector, based on micro-strip silicon devices and located at the intermediate region of the tracking system. The micro-strip silicon detectors were used between 20 and 130 cm, of the inner detector. The particle flux is reduced significantly in the intermediate region compared to the innermost region. The minimum cell size is 10 cm ´ 80 μm and the occupancy rate per LHC crossing is about 2-3%. The strip detector along with the Pixel Detector is used for pattern recognition, track reconstruction and momentum measurement for all tracks above 2 GeV/c transverse momentum originating from high luminosity interactions at $\sqrt{s} = 14$ TeV.

The silicon strip tracker is consists of 15148 detector modules distributed among the four different subsystems (TIB, TID, TOB, TEC). Each module contains either one thin (320 μm) or two thick (500 μm) silicon sensors. In addition, the silicon strip detector consists of 25000 strips. Moreover, this detector composed of 4 inner layers (TIB) and 6 outer barrel layers (TOB). On each side of the TIB, there are three mini disks (TID). Each endcap region composed of 9 disks (TEC). Fig. 1.25 indicates longitudinal view of the silicon strip tracker (one quarter).

1.2.3.3. The Calorimeters

The calorimeters are experimental apparatus used to measure the energy of particles. The calorimeters of the CMS play an important role in the use of physical potential. The CMS calorimeters design goal is to identify and measure precisely the energy of photons, electrons and hadrons (jets) and to provide hermetic coverage for measuring missing transverse energy, E^T_{miss}. Additional requirements for the calorimeters are include good efficiency for photon and electron identification, good separation of TT-Hadronic decays from normal QCD jets, and excellent background rejection for hadrons and jets. After entering the calorimeter, most particles start a particle shower, and their energy is completely absorbed and converted to a measurable signal. Basically, the CMS calorimeter system has two layers. The first layer is the electromagnetic calorimeter called ECAL.

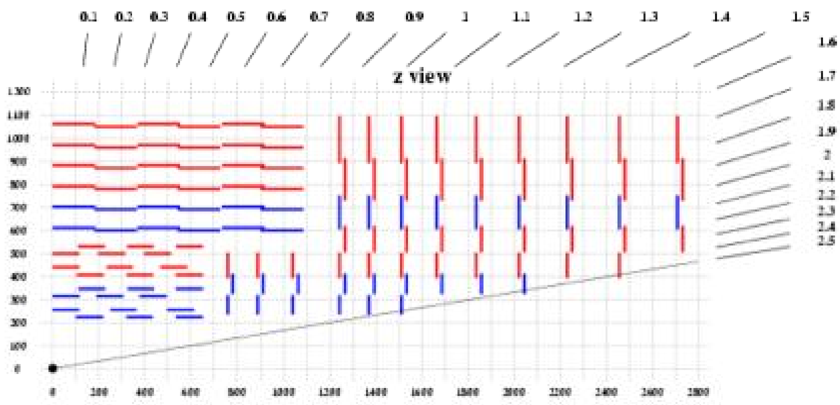

Figure 1.25. Longitudinal view of the silicon strip tracker (one quarter) (Moortgat, 2004)

The ECAL is used to measure the energy of particles which interact electromagnetically such as photons and electrons. The second layer is hadronic calorimeter, also called HCAL. This calorimeter used to measure the energy of strongly interacting particles, hadrons (e.g. p, n, π^0, $\pi^\pm$, K etc.).

The neutrinos interact only via weak interaction and their interaction cross section is so small. They escape all CMS without interacting with matter. These particles can be observed indirectly as imbalanced event energy in the transverse plane. This imbalanced event energy in the transverse plane is called missing transverse energy and it is denoted by E_{miss}^{T}. This energy plays an important role for new physics searches like SUSY. Fig. 1.26 is illustrated the locations of the ECAL and HCAL (quarter slice-longitudinal cross section) in and around the CMS magnet.

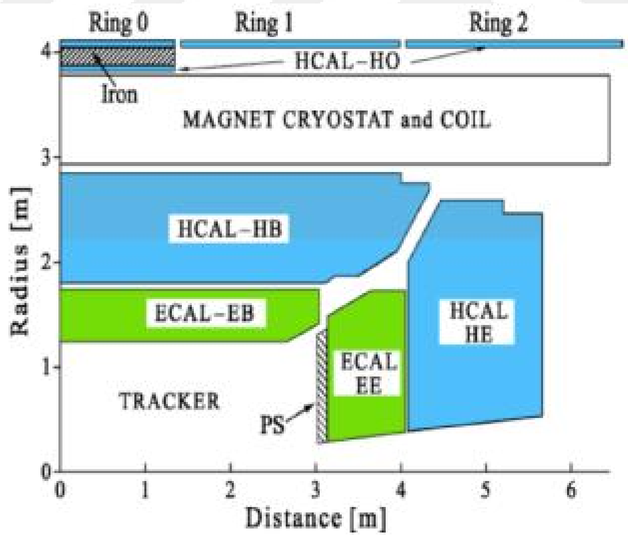

Figure 1.26. Location of the ECAL and the HCAL detectors in and around the CMS magnet (Abdullin et al., 2009)

1.2.3.3.(1). The Electromagnetic Calorimeter

The ECAL (The CMS Collaboration, 1997b) is the sub-detector of CMS detector, used to the measure the energy and position of electrons and photons. The ECAL detector is of course very important also in the measurement the energy and position of hadronic jets since hadrons begin showering and lose some of their energy in ECAL. Especially, the ECAL have been designed for the measurement of a low-mass Higgs boson in the decay channel $H \rightarrow \gamma\gamma$, and it played very an important role in the Higgs boson's discovery. The solution chosen to achieve the required energy resolution is the hermetic, homogeneous ECAL, consist of 75848 lead tungstate ($\mathrm{PbWO_4}$) crystals with about $2.2 \times 2.2 \times 23\ \mathrm{cm}^3$ in size. 61200 of these crystals are in the barrel part and 7324 crystals are in the two endcaps. The $\mathrm{PbWO_4}$ have a short radiation length (0.89 cm), a high density (8.28 $\mathrm{g/cm^3}$) and a small Moliere radius (2.2 cm), these features let to design a fine-grained and compact calorimeter.

The structure of ECAL is divided in a central cylindrical part (the barrel) and two endcaps. İt remains between the tracker and the HCAL. An additional preshower detector is placed in front of the endcaps. A 3D view of the ECAL detector is given in Fig. 1.27a: preshower, endcap and barrel are visible and a $H \rightarrow \gamma\gamma$ event is shown for illustrative purpose. Fig. 1.27b illustrates a geometric view of one quarter of the ECAL in the longitudinal section.

The pseudorapidity coverage of geometrical crystal extends to $|\eta| < 3$. The transverse granularity of $\Delta\eta\ \times\ \Delta\Phi = 0.0175\ \times\ 0.0175$, corresponding to a $\mathrm{PbWO_4}$ crystal face of 2.2×2.2 cm, matches the $\mathrm{PbWO_4}$ Moliere radius of 2.2 cm. The small Moliere radius, by reducing the area over which the energy is summed, reduces the effect of pile up contributions to the energy measurement of particles.

In the endcaps, $(1.48 < |\eta| < 3.0)$, the granularity increases progressively to a maximum value of $\Delta\eta\ \times\ \Delta\Phi = 0.05\ \times\ 0.05$. A $\mathrm{PbWO_4}$ crystal has a length of 23 cm in the barrel region and 22 cm in the endcaps. Because of the existence of a preshower in the endcap region, slightly shorter crystals are used.

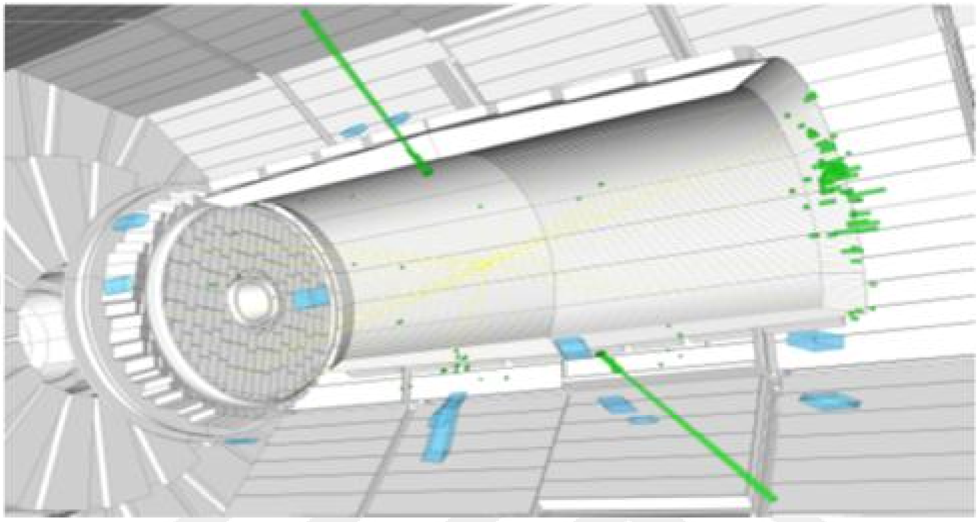

Figure 1.27a. The ECAL in a 3D view with candidate Higgs boson decaying into two photons (large green towers)

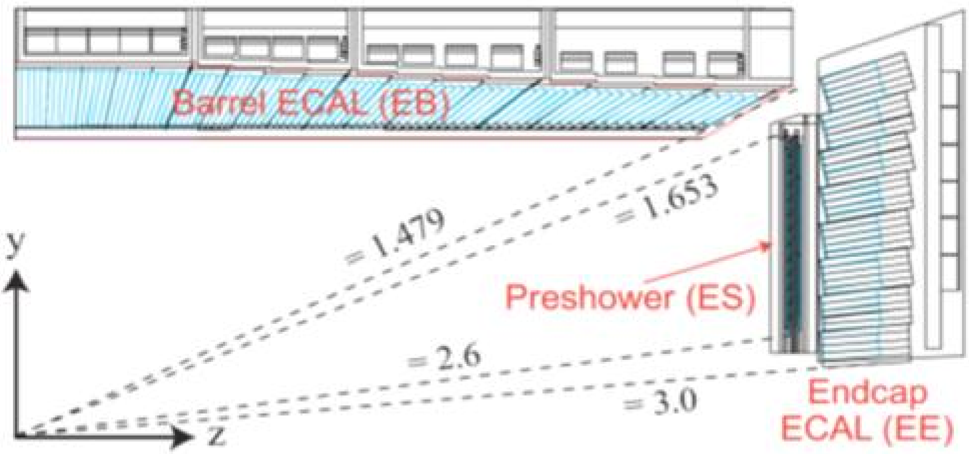

Figure 1.27b. A geometric view of one quarter of the ECAL in the longitudinal section (Bayatian et al., 1997a)

For the energies between 25 GeV and 500 GeV, the energy resolution of a homogeneous calorimeter for photons (these photons are coming from the H→γγ decay) and electrons can be parameterized as a squared sum of three terms (Chatrchyan, 2008a):

$$\left(\frac{\sigma}{E}\right)^2 = \left(\frac{S}{\sqrt{E}}\right)^2 + \left(\frac{N}{E}\right) + c^2 \quad (1.69)$$

where s is the stochastic term and it depends on fluctuations of the number of detected photons. N is the noise term and it contains the contributions from electronic noise and pile-up energy. c is the constant term and this term depends on lateral containment, non uniformity of response and intercalibration. Also, Energy (E) is expressed in GeV. The different contributions expected for the energy resolution summarized in Fig. 1.28. The endcap preshower detector covers a pseudorapidity range of 1.65 < $|\eta|$ < 2.61, and they are placed in front of the ECAL crystals. The main goal of design of the preshower detectors is to provide $\pi^0 - \gamma$ separation.

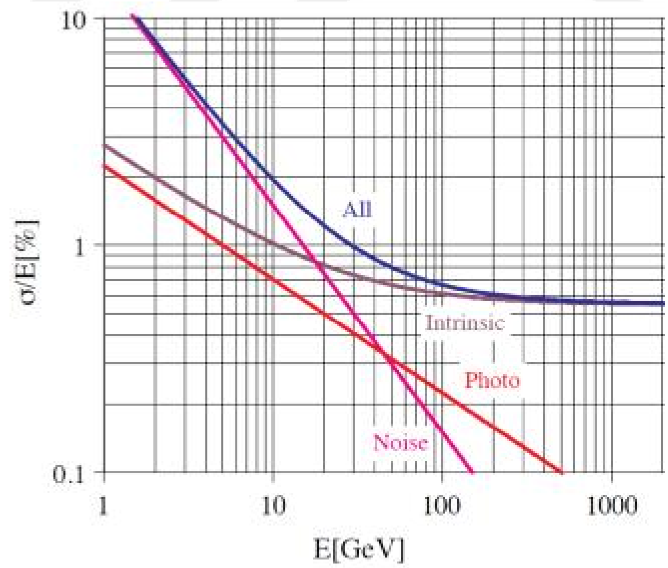

Figure 1.28. Different contributions to the energy resolution of the ECAL calorimeter (Chatrchyan et al., 2008a)

1.2.3.3.(2). The Hadronic Calorimeter

The ECAL is surrounded by the HCAL (Bayatian et al., 1997b) inside solenoid magnet, and measure quark, gluon and neutrino directions and energies by measuring jets and missing transverse energy, E_{miss}^{T}, together with ECAL. The determination of the jets and missing energy with this way will be very important for discovery of new particles (like SUSY partners of quarks and gluons) and their phenomena. The HCAL calorimeter finds a particle's energy, position and arrival time using alternating layers of absorber and fluorescent scintillator materials that produce a rapid light pulse when the particle passes through. Special optical fibres collect up this light and sends to read-out boxes where the photo-detectors amplify the signal. When the amount of light in a particular region is summed over a layer of many tiles at a depth, called a tower, this total amount of light is a measure of the energy of a particle. The HCAL extends radially from the outer surface of the ECAL to the inner surface of the magnet from 1.77 m to 2.95 m.

In order to provide the most important requirements (hermeticity, good transverse granularity, good containment of the hadron shower), the HCAL consists of four sub-detector which are barrel (HB and HO), endcap (HE) and forward (HF) sections:

- There are 36 barrel wedges which have 26 tons weight. While these constitute the final layer of the detector inside the magnet coil, a few additional layers, the outer barrel (HO), sit outside the magnet coil, ensuring no energy leaks out of the back of the HB.
- The HE consists of a 36 endcap wedges and is used to measure the energies of the particles that emerge along the ends of the solenoid magnet.
- The two hadronic forward calorimeters (HF) are located at either end of the CMS, for collecting the myriad particles coming out of the interaction point from narrow angles relative to the beam line. These receive the bulk

of the proton beams energies contained in the collision, so they must be very resistant to radiation and use different materials for the other parts of the HCAL calorimeter.

A longitudinal view of a quadrant of HCAL is illustrated in Fig. 1.29. All of the HCAL calorimeter components are visible: HB, HE, HO and HF.

The hadron barrel part of the HCAL (HB) covers the pseudorapidity range $|\eta| < 1.3$ and is located inside the magnetic coil. It consists of 2304 towers. Each tower consists of alternating layers of non-magnetic brass absorbers and plastic scintillators material. The reason why the absorber material is not magnetic should be that it does not affect the magnetic field. Also, HB is divided into two half-barrels, (HB+ and HB-) and each section consists of 18 identical azimuthal wedges, resulting in a segmentation of $\Delta\eta \times \Delta\Phi = 0.087 \times 0.087$.

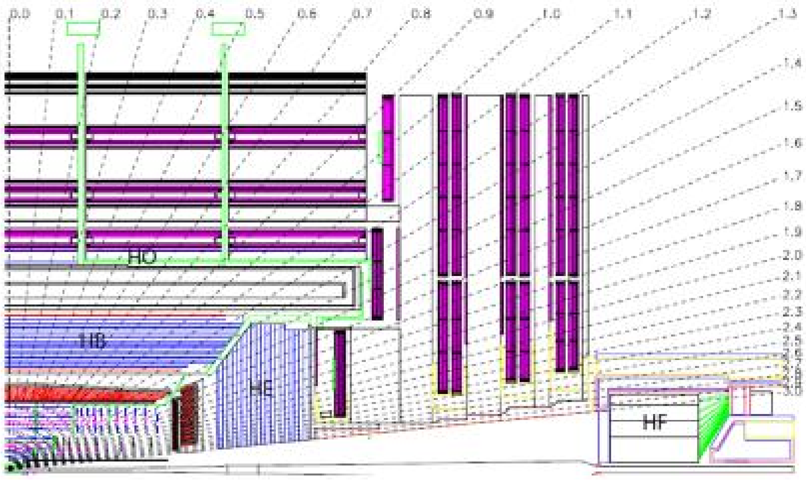

Figure 1.29. Longitudinal view of one quarter of the detector in the rη-plane, showing the positions of the HCAL parts: hadron barrel (HB), hadron outer (HO), hadron endcap (HE) and hadron forward (HF) (Chatrchyan et al., 2008a)

The two HE cover the pseudorapidity range $1.3 < |\eta| < 3.0$. They are placed at the end of the CMS detector and so that it is allowed to contain magnetic material. The brass is used here as an absorber material. The granularity of HE begins from $\Delta\eta \times \Delta\Phi = 0.087 \times 0.087$ at $|\eta| < 1.6$ up to $\Delta\eta \times \Delta\Phi = 0.17 \times 0.17$ at $1.6 < |\eta| < 3.0$.

The combination of EB and HB doesn't have enough stopping power for the hadron showers in the central pseudorapidity region. Hence, the HCAL calorimeter is extended outside the solenoid coil with a tail catcher which covers the pseudorapidity range of $|\eta| < 1.3$. This part of the HCAL is called the hadron outer calorimeter, denoted as HO. Namely, HO is located outside of the magnet and it has the task to absorb escaping hadron showers from particles with transverse energies above 500 GeV. Without the HO calorimeter, these particles would cause a large missing transverse energy which is not suitable for many physics analysis purposes. The granularity and pseudorapidity range, $|\eta|$, of HO is the same as the HB.

The HF iron-quartz calorimeters are the forward detectors of the HCAL. These calorimeters are positioned 11.2 m away from the interaction point to cover the pseudorapidity region $3.0 < |\eta| < 5.0$. They are located at the both ends of the CMS. The HF located outside the CMS magnetic coil. This calorimeter is a cylindrical steel structure and made of iron absorbers and radiation hard quartz fibres to provide a fast collection of Cherenkov light as the active medium. The goal of the HF is to improve measurement of missing transverse energies and to enable identification and reconstruction of very forward jets which are distinguishing characteristic of several important physics processes. When the velocity of a charged particle is bigger than the speed of light in the same quartz, it causes Cherenkov radiation. This radiation produces a signal in HF. Particles that enter the absorber of a calorimeter initiate showers of particles. The embedded quartz fibers have two different lengths to distinguish differences between shower processes. Short and long quartz fibers places separately and readout with phototubes. Longer fibers (1.65 m) provide light from EM and hadronic showers in the absorber while shorter fibers (1.43 m) provide light from the hadronic showers (Chatrchyan, 2008a). Each HF module has 18 wedges in a non-projective geometry; quartz fibers extend parallel to the axis of the beam along the length of the iron absorbers as seen in Fig. 1.30a. The detectors are divided into exactly a tower geometry. There are 13 towers in η and η segmentations are shown in Fig. 1.30b for HF. The iron absorber has 10 nuclear interaction lengths. Fig. 1.31 presents a cross sectional view of the HF.

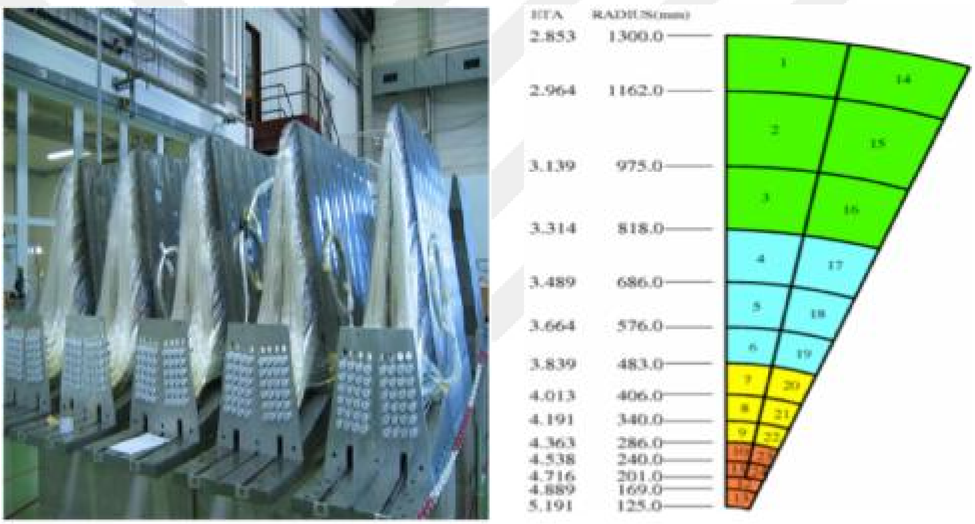

(a) (b)

Figure 1.30. a) CMS HF calorimeter production wedges, b) η segmentation and size increase in HF (Bayatian et al., 2006)

The energy resolution of the HCAL is

$$\frac{\sigma}{E} = \frac{100\%}{E(GeV)} + 8\% \qquad (1.70)$$

where σ is the uncertainty on the measured energy and E is in GeV. It is worse than the ECAL resolution, so the energy resolution of the combined calorimeters is dominated by HCAL.

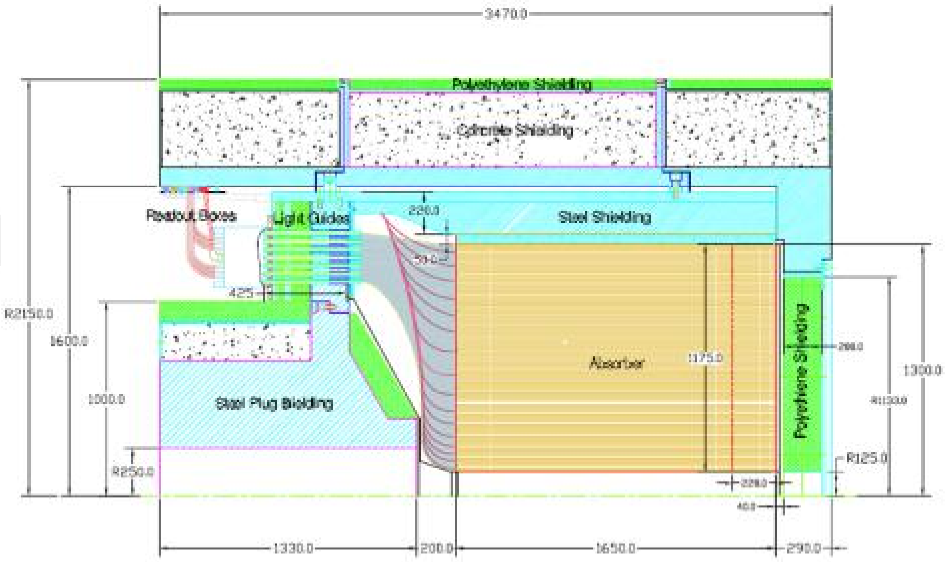

Figure 1.31. The cross sectional view of the HF calorimeter (Chatrchyan et al., 2008a)

1.2.3.4. Solenoid Magnet

In the CMS experiment, a solenoid superconducting coil is used to create a 4 T magnetic field over the entire tracking region (Bayatian et al., 1997c). The tracking system, ECAL and HCAL calorimeters (except HO) are surrounded by the coil. The 4 T magnetic field that produced by the superconducting magnet system, is provide precise measurements of transverse momentum by bending the tracks of charged particles.

The CMS superconducting solenoid as shows in Fig. 1.32 has an inner diameter of 5.9 m and is 13 m long. The length/radius ratio of the solenoid and the high field allows efficient to muon detection and measurement up to pseudorapidity of 2.4. The magnetic flux generated by the superconducting coil is returned with a 1.5 m thick saturated iron yoke (Return Yoke) where the field is 1.8 Tesla. The Return Yoke is divided into two main components, barrel and endcap yoke. The barrel yoke, which is 13.2 m long, is designed as a 12 sided cylindrical structure. The End Cap Yoke is designed to provide access to the forward muon stations.

The transverse momentum (P_T) of a charged particle in a magnetic field is expressed as:

$$P_T = 0.3 \times B \times R \tag{1.71}$$

where, the radius of curvature of the charged particle and the magnetic field are denoted by R and B, respectively. The distance from the collision point to the ECAL surface is nearly 1.3 m. The CMS detector requires a minimum transverse momentum of $P_T = (0.3 \times 4 \times 1.3)/2 = 0.78\, GeV$ to allow charged particles to reach the ECAL surface.

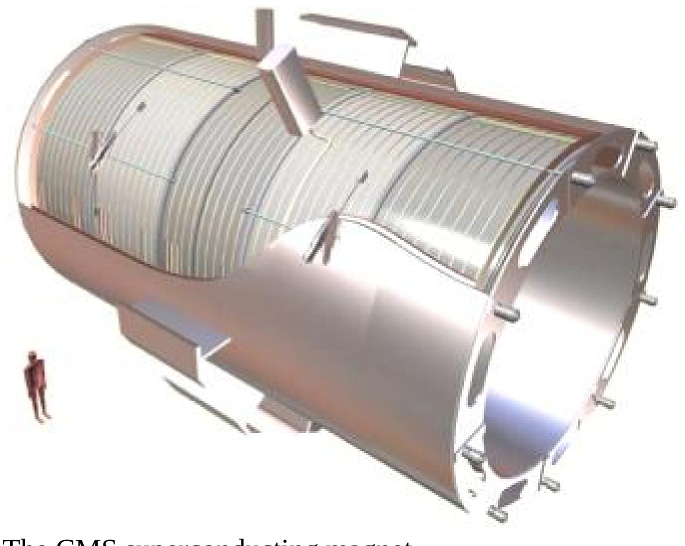

Figure 1.32. The CMS superconducting magnet

1.2.3.5. The Muon System

The muon system (The CMS Collaboration, 1997a) or spectrometer is located the outermost of the CMS sub-detectors. This detector, which CMS also takes its name from, is designed to provide robust muon identification and precise momentum measurement because muons have an effective role in physics studies. Although the muons are charged particles like electrons and positrons, they are 200 times heavier than these particles and are the only charged particles that can be able to pass through the calorimeters without being absorbed at the same time. They don’t interact much with the atoms because of their heavy mass. For this reason, they don’t generate electromagnetic showers. High-energy muons (e.g. 5 GeV) can pass through materials such as copper and steel without losing much energy. Therefore, the muon detector is placed out of the CMS by covering the tracker, ECAL, HCAL and bobbin, respectively. Muons are expected to be produced in the decay of some potential new particles; For example, one of the clearest “signatures” of Higgs Bozon is the four muon decay. This decay process called “golden channel” and it is in the form of $H \rightarrow ZZ \rightarrow 4\mu$ or $H \rightarrow ZZ' \rightarrow 4\mu$.

The muon detector covers the pseudorapidity range of $|\eta| < 2.4$. The muon detector chambers have three purposes: muon identification, muon momentum measurement, muon trigger and this detector chambers are designed to reconstruct momentum and charge of muons over the entire kinematic range of the LHC (Chatrchyan et al., 2008a). Due to the shapes of the sub-detectors of the CMS, the muon system is naturally made to have a cylindrical shape. The system is divided into a cylindrical barrel region and two endcaps. The muon system also consists of three different gaseous detector systems such as Aluminum Drift Tubes (DT), Resistive Plate Chambers (RPC) and Cathode Strip Chambers (CSC), respectively. In the barrel region, the magnetic field (4 T) is uniform, the muon rate is low and muon system uses DT. In the two endcaps regions, the muon rate is high, the magnetic field is large and non-uniform and the muon system uses CSC.

DT chambers and CSC detect muons in the regions $|\eta|<1.2$ and $0.9<|\eta|<2.4$, respectively, are complemented by a system of RPC covering the pseudorapidity range $|\eta| < 1.6$. Also, drift tube (DT) chambers are organized into 4 stations. The first 3 stations contain 8 chambers each of which measure the muon coordinate in the $r - \Phi$ bending plane and in the z direction, through the beam line. The fourth station, which does not contain the z-measuring planes, is used to achieve the best angular resolution. The Fig. 1.33 shows layout of the CMS muon systems and the Fig. 1.34 shows a transverse view of the CMS barrel muon DT.

1.2.3.6. The Data Acquisition and Trigger System

The proton-proton and lead-lead (heavy-ion) collisions occurs at high interaction rates as mentioned of section 1.2.2 at the LHC. The beam crossing interval is 25 ns for the protons, and this corresponding to a frequency of 40 MHz. Several collisions are expected during each crossing of the proton beams, which vary depending on the luminosity. It is expected that an average of 20 simultaneous inelastic proton-proton collisions occuring at a nominal design luminosity of $10^{34}\text{cm}^{-2}\text{s}^{-1}$ at the $\sqrt{s}$ = 14 TeV. This corresponds to about 10^9 collisions per second. Since the nominal event size is about 2 MB, this is also corresponding about 100 TB per second. Due to the high rate of p-p interactions, it is practically impossible to store and process the large amount of data. Hence, an extreme rate reduction has to be achieved. This task is performed by the CMS Trigger system and is known as the start of the physics event selection process. The goal of the CMS trigger systems is to lower the event rate from 10^9 Hz down to of 10^3 Hz, the maximum rate that can be archived by the online computer farm. Reduction of the event rate is performed in two steps by the CMS Trigger system:

- Level-1 (L1) Trigger,
- High-Level Trigger (HLT).

Schematic view of the CMS trigger and DAQ system is shown in Fig. 1.35.

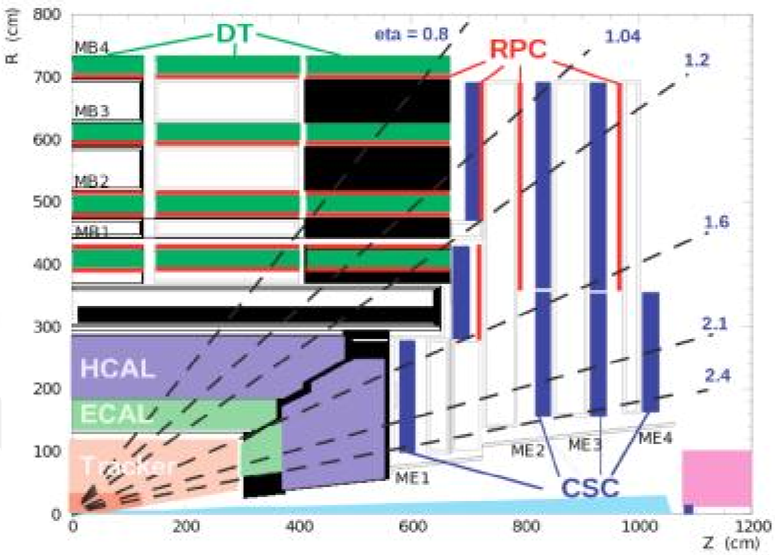

Figure 1.33. The Layout of the CMS muon system (CMS Collaboration, 2012)

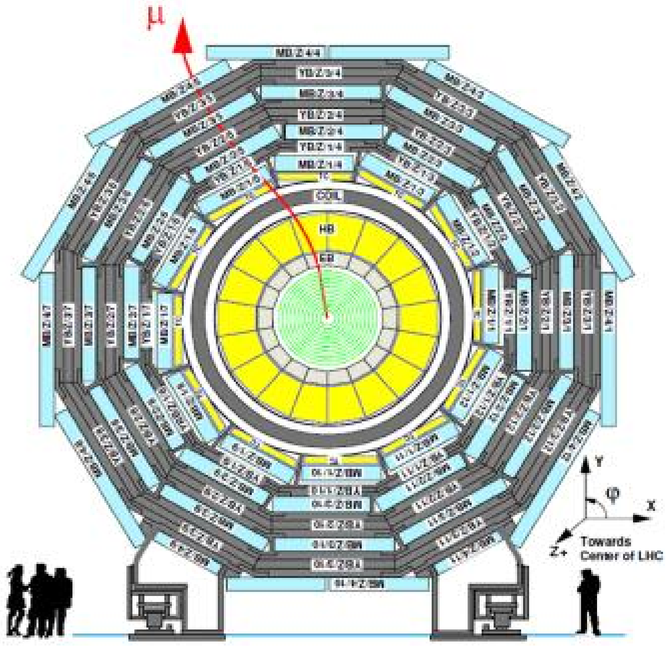

Figure 1.34. A transverse view of the CMS barrel muon DT chambers

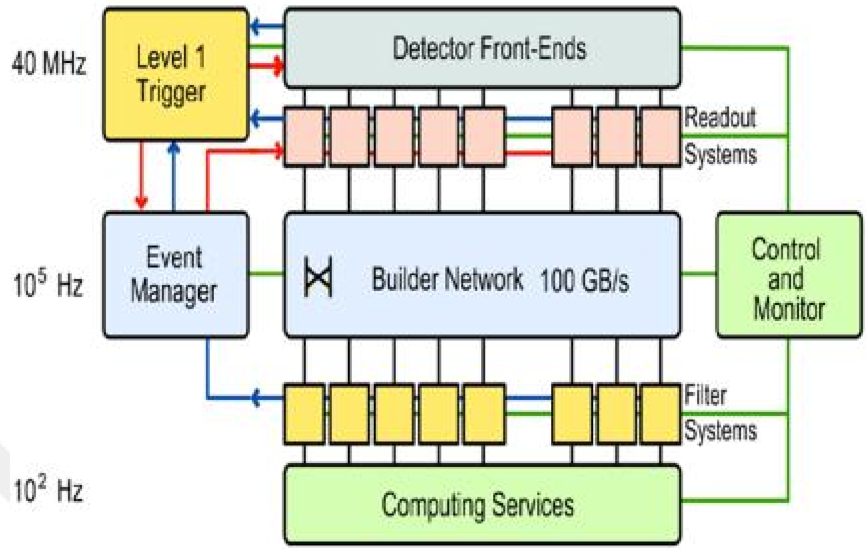

Figure 1.35. CMS trigger and DAQ system (Bayatian et al., 2006)

1.2.3.6.(1). The Level-1 Trigger

The Level-1 (L1) triggers include the muon systems and calorimetry and some correlations of information between these systems and is designed to keep or delete the data and consists of custom-designed hardware processors, mostly programmable electronics. The maximum rate of the trigger is 100 kHz, and this rate limited by the speed of the detector readout programmable electronics. The L1 decision depends on the subsistence of “trigger primitive” local objects like electrons, muons, photons and jets above set E_T or P_T thresholds. At the same time it is using global sums of E^{miss} and E_T (Chatrchyan et al., 2008a). Calorimeter and muon system, which are analysis the data locally, are working in parallel. They then combine the data and generate output that is passed on to DAQ. Because of the L1 trigger system is positioned outside the detector (about 90 m), there is a latency of 3.2×10^{-6}s between the bunch crossings. The purpose of the L1 trigger system is to analyse the every 40 MHz proton-proton collision and to reduce the data rate passed on to the HLT to 100 kHz. As shown in Fig. 1.36, the L1 trigger is separated to three basic subsystems because of its high efficiency.

· L1 Calorimeter Trigger,
· L1 Muon Trigger,
· L1 Global Trigger.

As shown in Fig. 1.36 the L1 Global Trigger combines the outputs of two triggers (L1 Calorimeter Trigger and L1 Muon Trigger). However, the L1 Muon Trigger is known as the L1 Global Muon Trigger, which combines specific triggers from RPC, CSC and DT. After the decision whether taking or discarding data from a particular bunch crossing the data is sent to the HLT system at 100 kHz output rate for further evaluation.

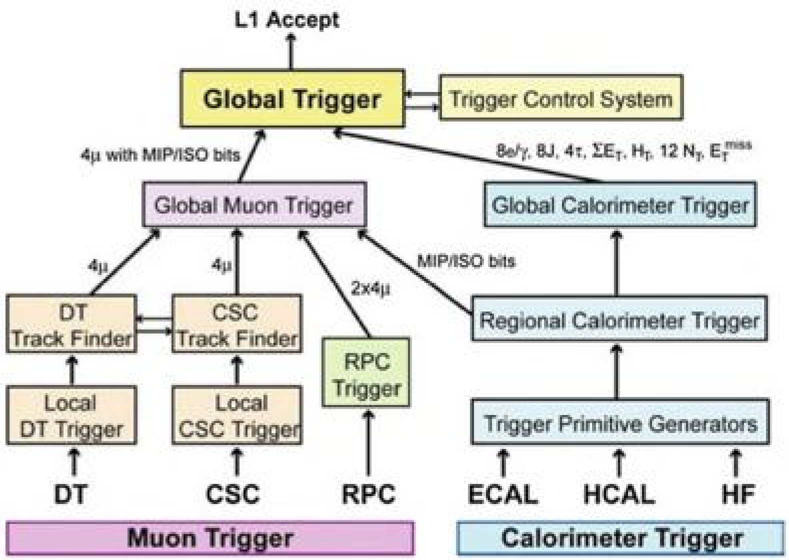

Figure 1.36. Level-1 Trigger architecture (Chatrchyan et al., 2008a)

1.2.3.6.(2). The High Level Trigger

The High Level Trigger (HLT) system is a customizable software system that can be implemented in a filter farm containing about one thousand commercial processors and uses the detector signals passing through the L1 trigger. However, the HLT is responsible for reducing the L1 output ratio to 100 Hz. It can run at high resolution and ensure precisely reconstruction of the event. The HLT decisions are based on the information of all sub-detectors, in which includes the data from the tracker and the full granularity of the calorimeters. The HLT Trigger receives an average event every 10 μs. Since this time is long enough, algorithms can be used for offline reconstruction of the events.

1.2.3.7. The Software and Computing

The CMS software and computing systems must have a wide variety of functions including construction, design, calibration, and evaluation of the detector. Supporting the storage, transfer and manipulation of the received and recorded collision data during the experiment are of the important tasks. The system retrieves detector information from the DAQ system and ensures that the raw data is safely prepared. In addition, the system, which performs model recognition, event filtering and data reduction, supports the physics analysis studies of the CMS collaboration. The system must also supports production and distribution of the simulated data, and access to conditions, calibration information and other non-event data.

The CMS software system performs various event processing, selection and analysis tasks. The software should be developed taking into account factors such as performance, sustainability, modularity, flexibility, documentation and quality assurance. The CMS adopts object-oriented development method which is based on the C ++ programming language.

The aims of the CMS Framework and Event Data Model (EDM) are to facilitate the development and use of analysis software and reconstruction. The central concept of the CMS EDM is the event. The events that enable access to the recorded data are stored as physically persistent ROOT files. The event is used by various physics modules. These modules can read the data from the event or automatically add new data with provenance information. The modules aim to allow independent development and validation of separate components of reconstruction, simulation, triggering and analysis. The modules operate independently of each other, but they communicate only through the event. The CMS Application Framework is shown in Fig. 1.37.

The CMS computing system has various event formats such as RAW, RECO (Reconstructed) and AOD (Analysis Object Data). These event formats have different detail and precision levels to achieve the required level of data reduction.

The RAW Event format does not only contain information that is full-recorded from the detector but also includes a record of the trigger decision.

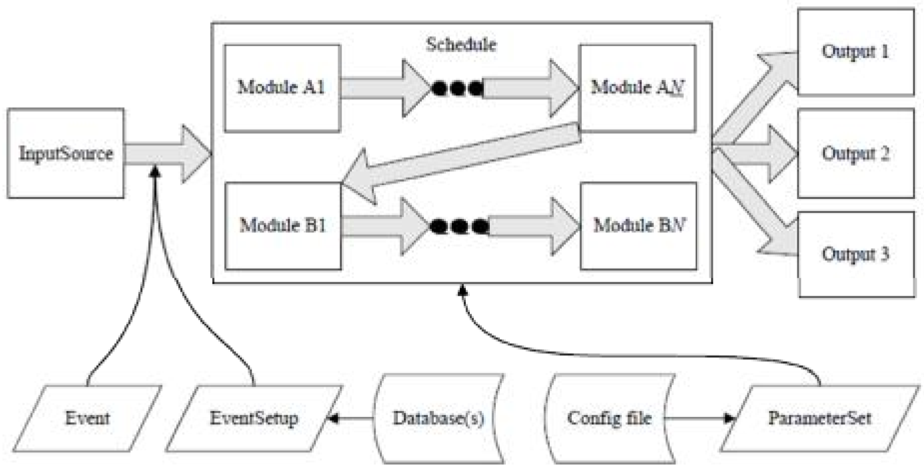

Figure 1.37. The CMS Application Framework with modules

However, the RAW root files also contain raw form information such as hit and energy deposits on the recorded event. While the RAW data is stored permanently and securely at approximately *1.5 MB/event* size, the RAW format size is to approximately *2 MB/event* when MC real information is added to these data. The biggest contribution to this RAW data is expected from the silicon strip detector.

RECO data is generated by applying a few level pattern recognition and compression algorithms to the RAW data, including detector specific filtering and correction of digitized data such as cluster- and trackfinding, primary and secondary vertex reconstruction, and particle ID (Chatrchyan, 2008b). RECO contains high-level physics objects such as jets, muons, electrons, b-jets, etc. objects selected from reconstruction modules, and it is quite large, at the level of 500 kB/event. After these arrangements, it is important that RECO data have access to reconstructed physics objects in a format suitable for physics analysis.

AOD is containing only high-level objects and is the compact analysis format which is produced by filtering of RECO data. The size of the AOD data format is about 50 kB/event after filtering the RECO data.

A computing system with such a scale has arranged the CMS offline computing system in four tiers in order to entirely hosted at one site the AOD events. These tiers are Tier-0, Tier-1, Tier-2 and Tier-3 respectively and each of them providing several resources and services. The raw data passing through the HLT trigger and CMS Online DAQ system is stored in storage facility at CERN, known as Tier-0 and there is only one Tier-0. The Tier-0 centre achieves prompt first pass reconstruction and then it distributes RAW and processed data to a set of large Tier-1 centers in CMS collaborating countries. There are seven centers and they are responsible for the safe keeping of a copy of the RAW data. At the beginning of the data, 2 copies of the reconstructed data are kept in the Tier-1 centers, but then this number decreases to 1 owing to the amount of data increases. These centers must have enough CPU power to be able to perform large scale reconstruction steps. However, these centers offer services for skimming, calibration and other data-intensive analysis tasks. A more numerous set of Tier-2 centers provide analysis activities and specialized activities such as offline calibration, and detector studies and production of MC simulation. The Tier-3 centers, which are providing best effort computing capacity for the collaboration, interactive resources for local groups are provided. The CMS users usually rely on Tier-2 or Tier-3 resources as their base for analysis with the Tier-1 centers which are providing the large-scale facilities (Bayatian et al., 2005). The data flow between CMS Computing Centers is shown in Fig. 1.38 (Chatrchyan et al., 2008a).

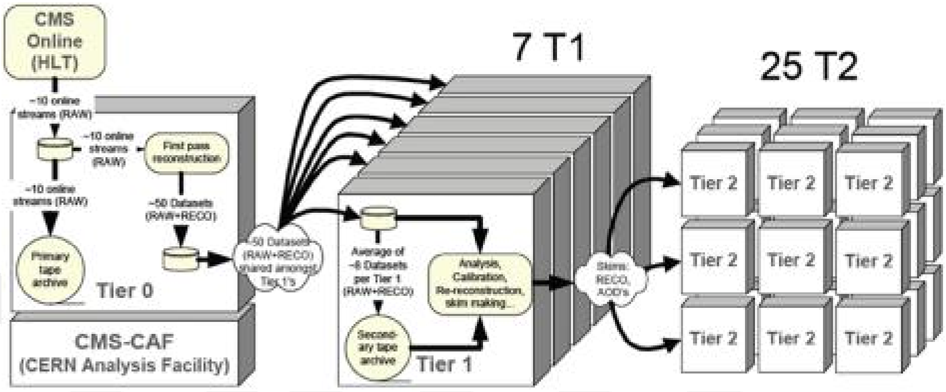

Figure 1.38. The data flow between CMS Computing Centers

2. MATERIAL AND METHOD

2.1. Jet Reconstruction at CMS

Parton model is successful in describing many features of the strong interactions that are observed in hard scattering processes. For example, the Bjorken scaling observed in deep inelastic regime for the scattering of electrons off nucleons, the dynamics of the Drell-Yan processes and the physics of jets can be easily understood in the context of the parton model. The main processes that could provide clear experimental tests for the theory of hadronic interactions - QCD – are the $qq, q\bar{q}, qg$ … etc. scatterings. These processes can be studied in the production of large transverse momentum jets in hadron-hadron collisions. In this chapter we will define appropriate kinematical variables for the studying jets which simplifies most the calculations and theoretical analyses. Further details on theoretical background and also a comprehensive review of the CMS experiments along with many features which are interesting from the experimental side may be found in (Ellis, 1996).

2.1.1. Theoretical Background

The high energy scattering of two hadrons is a result of a more fundamental interaction between their constituents, i.e. quarks and gluons. This is the most common case of hard interaction at hadron colliders which takes place by the scattering of one of the partons of the proton and one of the partons of the (anti)proton, respectively. As already defined in Eq. 1.21 these constituents may have an arbitrary momentum inside the hadrons and since they are confined into the parent hadrons, then, the total cross section of the scattering initiated by two hadrons with 4-momenta P_1 and P_2 was given by

$$\sigma(P_1,P_2)=\sum_{i,j}\int dx_1 dx_2\, f_i\left(x_1,\mu_F^2\right) f_j\left(x_2,\mu_F^2\right)\hat{\sigma}_{i,j}\left(p_1,p_2,\alpha_s\left(\mu^2\right),Q^2/\mu^2\right) \quad (2.1)$$

The partons involved in the hard scattering carry a fraction of the proton momentum. The fraction of the total momentum of the proton is commonly called x. In the above formula, we have used the notation $p_1 = x_1 P_1$ and $p_2 = x_2 P_2$ for the participating partons. Also, Q is the characteristic scale of the hard scattering which could be, for example, the mass of a weak boson or a heavy quark, or the transverse momentum of a jet. The functions $f(x_i, p_i)$ are the usual QCD parton distributions, defined at a factorization scale μ. The main quantity of interest here is the fundamental cross section for the scattering of partons of types i and j which we have denoted by $\hat{\sigma}_{ij}$. On the other hand, due to the coupling strength for the strong interaction is small at high energies, the fundamental cross section can be calculated by using a perturbation series in the running coupling α_s. Note that for the LO Feynman diagrams for qq, the resulting cross sections are proportional to α_s^2. When protons and antiprotons collide to each other, in most of the cases, only two of the partons interact in a hard scattering process while the remnants of the protons and (anti)-proton hadronise to form jets and scattered in a very small angle to the initial beam direction.

2.1.2. Coordinate Systems and the Kinematics

Quarks and gluons cannot be observed in free form because of QCD confinement. The confinement results in hadronization of jets into hadrons. Therefore, a proton is a manifestation of a jet in the fundamental level which has been materialized as a spray of energetic hadrons. Fig. 2.1 shows the evolution of a jet in its simplest form (Salam, 2006).

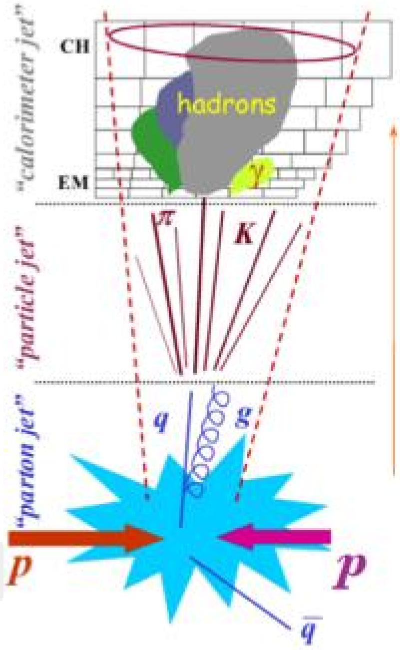

Figure 2.1. Evolution of a Jet

Events in which jets are created are used to understand the hadronic interaction. They can also be used to search for signatures of new physics in strongly interacting systems. A right handed coordinate system can be used to describe the kinematics of the jets. It is useful to take the z axis along the beam pipe. The origin of this system is chosen in the centre of the detector. An alternative coordinate system can be also used at hadrons colliders. This system exploits the cylindrical symmetry of the detector. The polar angle in this coordinate system is θ, the azimuthal angle is Φ, and the distance from the beam pipe is called r. More commonly, the direction of particles is given in Φ, y or η which respectively are called the rapidity or pseudorapidity and are defined as

$$y = \frac{1}{2} ln\left(\frac{E+P_z}{E-P_z}\right) \qquad (2.2)$$

$$\eta = -ln\left(tan\left(\frac{\theta}{2}\right)\right) \quad (E \approx p \gg m) \tag{2.3}$$

This variable is used instead of θ because $\Delta\eta$ is invariant under Lorentz transformations along the z-axis. This is very convenient, since the momentum along the z-axis is not always zero in the p-p centre-of-mass system. On the other hand, Φ does not depend on z. Another appropriate observable is the transverse momentum $P_T = \sqrt{P_x^2 + P_y^2}$ which is commonly used in jet physics calculations. The four components of momenta can be written as (Ellis, 1996)

$$P^{\mu} = \left(\sqrt{P_t^2 + m^2}\cosh(y), P_t \sin\Phi, \sqrt{P_t^2 + m^2}\sinh(y)\right) \tag{2.4}$$

A jet may be defined as a cluster of transverse energy E_T in a cone size ΔR which is given by (Ellis, 1996)

$$\Delta R = \sqrt{(\Delta\eta)^2 + (\Delta\Phi)^2} \tag{2.5}$$

and

$$E_{T_{jet}} = \sum_{i\in jet} E_{T_i} \tag{2.6}$$

$$\eta_{jet} = \frac{1}{E_{T_{jet}}}\sum_{i\in jet} E_{T_i}\eta_i \tag{2.7}$$

$$\Phi_{jet} = \frac{1}{E_{T_{jet}}}\sum_{i\in jet} E_{T_i}\Phi_i \tag{2.8}$$

2.1.3. Jet Types at CMS

As known at the moment there are 4 types of reconstructed jets at CMS depending on the utilized subdetectors. These jets differently combine individual contributions from sub-detectors to form the inputs to the jet clustering algorithm. These jet types are: Calorimeter jets (Calojets), Jet- Plus-Track jets, Track Jets and Particle-Flow jets, respectively.

2.1.3.1. Calorimeter Jets

These jets are depending on the reconstruction of energy deposits in the ECAL and HCAL cells to combine into calorimeter tower (Zielinski et al., 2010). The towers of each calorimeter, which are consists of one or more HCAL cells and the geometrically corresponding ECAL crystals, are the input into jet reconstruction algorithms. The structure of calorimeter tower which depends on η region of the CMS calorimeters, is built of unweighted sum of one single HCAL cell and 5 × 5 ECAL crystals in the barrel region ($|\eta| < 1.4$), while it is more complex in the endcap regions ($1.4 < |\eta| < 3.0$) of ECAL. Energy thresholds have been applied to the energy deposits in the cells to suppress the contribution from calorimeter readout electronics noise when building calorimeter towers. These threshold values are shown in Table 2.1 (Zielinski, 2010). In addition, to suppress contribution from p-p interactions in the same bunch crossing (pile-up) calorimeter towers with the transverse energy of $E_T^{towers} < 0.3\ GeV$ are not used in jet reconstruction. In Fig. 2.2 a sketch of the so-called “calorimeter towers” for the barrel region is shown. 5× 5 ECAL-cells and one HCAL tower are logically combined to form a calorimeter tower in the barrel region (Kirschenmann, 2010). In the mean time calorimeter segmentation in η and φ with energy deposition in calorimeter towers for dijet event is shown in Fig. 2.3 using event display. The red part and blue part, respectively shows energy deposition in ECAL and HCAL. The red part and blue part shows energy deposition in ECAL and HCAL, respectively.

Table 2.1. Threshold values of Calorimeter cell (Zielinski et al., 2010)

Section	Threshold (GeV)
HB	0.7
HE HO	0.8 1.1 / 3.5 (Ring 0 / Ring 1,2)
HF (Long)	0.5
HF (Short)	0.85
EB	0.07 (per crystal, double sided)
EE	0.3 (per crystal, double sided)
EB Sum	0.2
EE Sum	0.45

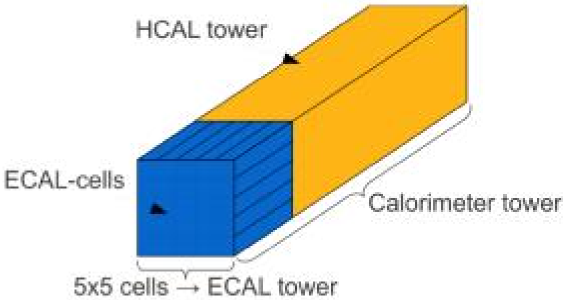

Figure 2.2. Sketch of calorimeter towers used for jet clustering

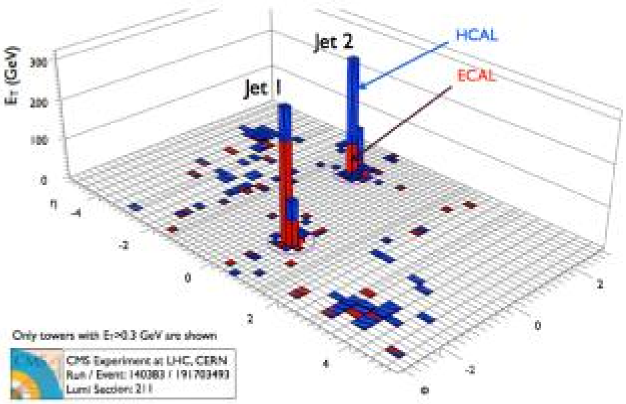

Figure 2.3. Observed dijet event in the CMS calorimeters

2.1.3.2. Jet-Plus-Track Jets

In this jets algorithm, jets are reconstructed using energy deposits in calorimeter towers and their energy are corrected using information of the calorimeter jets and the momentum of charged particles measured in the tracker (Nikitenko, 2009). In addition, the algorithms have been provided an improvement on the p_T response and resolutions of calorimeter jets at low p_T.

2.1.3.3. Track Jets

Track jets are reconstructed only from track of the charged particles measured in the CMS central trackers. These jets are completely independent from the calorimetric jet measurement (Azzurri et al., 2010). These jets also have been provided a very reliable way to find jets of any energy, even down to very low p_T of a few GeV/c.

2.1.3.4. Particle Flow Jets and Reconstruction

The Particle Flow (PF) (The CMS Collaboration, 2009) is a full event reconstruction technique which aims to reconstruct all stable particles, such as muons, electrons, photons, charged hadrons and neutral hadrons, produced in a given proton-proton collision. To accomplish this, it uses all of the CMS sub-detectors with all the details and associates the information contained in them to optimize particle reconstruction and identification performance. The design of the CMS detector is very suitable for the event reconstruction. The large silicon tracker and immersed 3.8 T magnetic field allows precise and efficient charged particle detection for transverse momenta such as 150 MeV, and the crystal electromagnetic calorimeter provides excellent resolution when measuring photon and electron energies. Charged particles, hadrons and photons constitute an average of 85% of one jet energy, so only 15% will be reconstructed individually in the hadronic calorimeter.

First, the PF algorithm collects the reconstructed hits separately for each sub-detector and then creates a list of basic reconstructed elements (blocks), ie charged tracks in the tracker, clusters of energy deposits in the calorimeters. Once the blocks have been constructed, a connection algorithm directs the particles that are topologically compatible to the particle flow particle candidates. Because of the type of blocks involved in their reconstruction, PF candidates may be of different types:

- electrons originate from the connection between a charged track and one or more ECAL clusters, provided that an electron identification set of criteria is satisfied;
- charged tracks that are not defined as electrons and are linked to any number of calorimeters (HCAL or ECAL) are reconstructed as charged hadron candidates;
- ECAL energy deposits that are incompatible with charged tracks give way to photon candidates;
- the energy deposits in the HF calorimeters are reconstructed as HF electromagnetic or hadronic particle candidates on the basis of the depth that the energies emerge in the HF quartz fibers;
- lastly muons are reconstructed and identified with a great efficiency and purity from the combination of the tracker and muon chamber information.

The creation of the PF candidate list represents the PF description of a proton-proton collision given in the CMS, as it attempts to best reflect the actual particle composition of the event. PF jet reconfiguration is a matter of choosing the jet algorithm on which PF candidates can be clustered, as it is discussed in the next topic.

The PF jet spatial resolution and momentum have been greatly improved in terms of calorimetric jets because the use of tracking detectors and the high granularity of the ECAL provide the resolution and measurement of the charged hadron and photons in a jet, which accounts for 85% of the jet energy. However, the non uniformity of the jet response as a function of p_T and η requires that jet energy be corrected as described in Sec. 2.1.5.

2.1.4. Jet Clustering Algorithms

Jet clustering algorithms are one of the most important tools for analyzing data from hadronic collisions in LHC. Clustering algorithms of jet are form a jet from a single hard-isolated particle composed of hadronic collisions. Jet reconstruction algorithms are used to provide a set of rules for clustering particles or calorimeter towers based on proximity into jets to reconstruct the jets. A “good” jet clustering algorithm must satisfy the some criteria which are decided by experimenters and theorists as listed below with the same features (Salam et al., 2010).

- It should be independent of detector structure and should be simple to implement in an experimental analysis,
- It should be simple to implement in the theoretical calculation,
- It should be defined at any order of perturbation theory,
- It should yield finite cross sections at any order of perturbation theory,
- It should producing a cross section that is relatively insensitive to hadronization effects,
- It should satisfy infrared and collinear safety.

One of the basic requirements for jet algorithms is Infrared and Collinear (IRC) security. According to the definition of “infrared safety”, the addition of a soft gluon should not change the results of the jet clustering. Collinear safety is that splitting one parton into two partons or a gluon splitting in two quarks should not change the results of the jet clustering (Salam, 2007). The configurations of non-infrared and non-collinear safe algorithms are shown separately in Fig. 2.4. A whole family of collinear-safe algorithms and infrared-safe algorithms are the k_T algorithms.

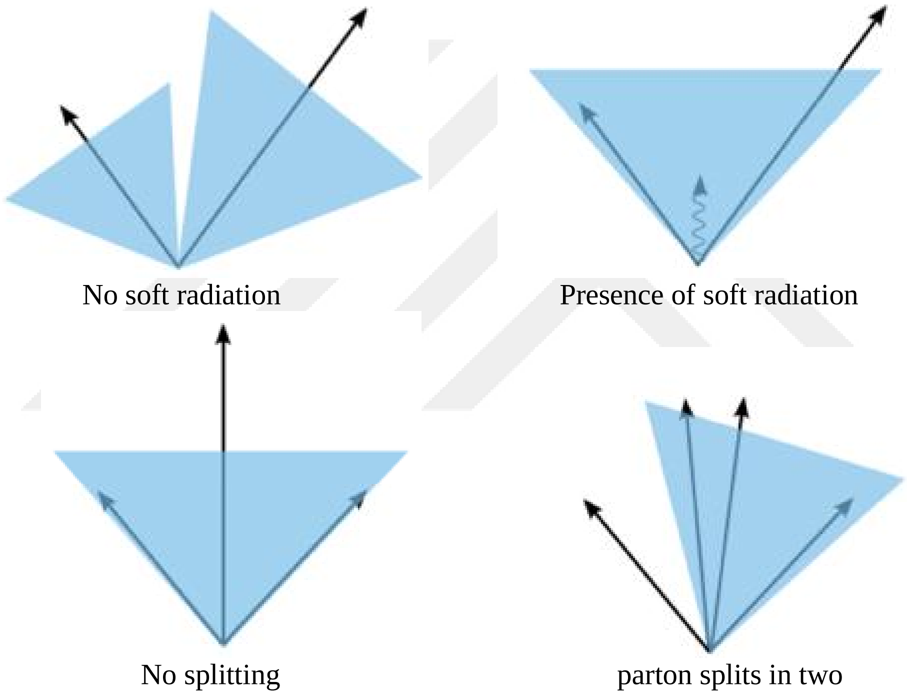

Figure 2.4. Infrared safety (top): adding a soft gluon not changing the jet clustering results, Collinear safety (bottom): splitting one parton into two collinear partons not changing the jet clustering results

There are three types of jet reconstruction algorithms generally used by the CMS experiment. These are Iterative Cone Algorithm, Seedless Infrared Stable Cone (SISCone) Algorithm and Anti-k_T Algorithm, respectively. These jet algorithms are discussed below.

2.1.4.1. Iterative Cone Algorithm

This algorithm is a simple cone-based algorithm that has a quick response and is often used for triggering purposes. Namely, it is not collinear or infrared safe algorithm. It is used by the CMS in the HLT because there is a short decision time (Schieferdecker, 2008). This simple algorithm combines the energy deposits located in a cone with radius R (given by Eq. 2.9 and R is a dimensionless parameter and is called the radius of the jet) around the most energetic calorimeter towers. In this algorithm, one starts to set a seed particle i (or calorimeter tower) with energy at least 1 GeV, and sums the momenta of all particles j within a cone. The cone's radius, R, is defined in terms of rapidity y and azimuthal angle Φ as following:

$$\Delta R_{ij} = \sqrt{\left(y_i - y_j\right)^2 + \left(\Phi_i - \Phi_j\right)^2} < R \tag{2.9}$$

where y_i is the rapidity and Φ_i is the azimuth of particle i. This process is repeated until a stable cone is found. When a stable cone is found it is added to proto jet list and its components are removed from the inputs list. CMS uses iterative cone algorithm with cone radius of R = 0.5.

2.1.4.2. Seedless Infrared Stable Cone Algorithm

Existing cone jet algorithms, e.g. the iterative cone algorithm, commonly used in hadron collisions, takes the all particles as a seed to search for stable cones. An important problem with cone jet algorithms is infra-red unsafety created by the addition of a soft particle between two hard particles. This soft particle may behave like a “seed” and then a third stable cone can be found (Salam, 2007). The solution of infrared unsafety in such algorithms is usually obtained by adding extra “midpoint” seeds as shown in Fig. 2.5. Firstly, these algorithms find the stable cones with true seed particles more clearly in this assumption of the solution. Then counterfeit midpoint seeds are added between the pairs of the stable cones. Finally, new stable cones are investigated. The time takes to find jets among the N particles goes as $N \times 2^N$. To solve this problem properly, the cone jet algorithm goes to the full seedless cone algorithm and the "midpoint" assumption is generalized to 2-dimensions (2D). Two degrees of freedom have been used to determine the position of the circle. A dimension has a single degree of freedom (y or η), and two dimensions have two degrees of freedom (y, Φ). The surrounding of the circle has a pair of particles as shown in Fig. 2.6 (Salam, 2007).

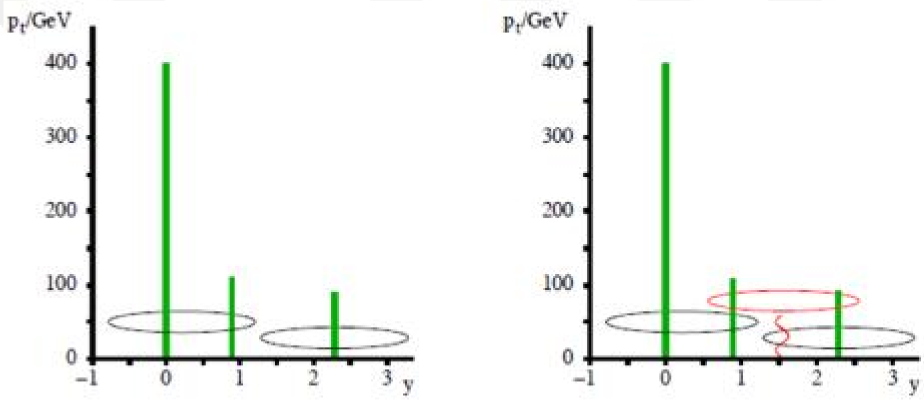

Figure 2.5. Configuration illustrating one of the IR unsafety problems of the midpoint jet algorithm (R= 1); (left) the stable cones (ellipses) found in the midpoint algorithm; (right) with the addition of an arbitrarily soft seed particle (red wavy line) being found an extra stable cone (Salam et al., 2007)

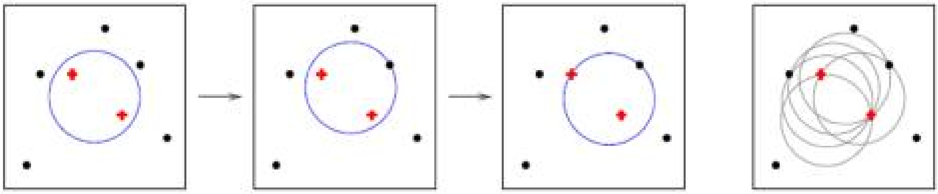
(a) (b) (c) (d)

Figure 2.6. Some initial circular enclosure (a); moving the circle in a random direction until some enclosed or external point touches the edge of the circle (b); pivoting the circle around the edge point until a second point touches the edge (c); all circles defined by pairs of edge points leading to the same circular enclosure (d) (Salam et al., 2007)

The time goes as $N^2.\ln(N)$ in this seedless cone algorithm, which is acceptable for hadron, parton and detector level. In this way, it is provided an acceptable IR safe cone algorithm called the SISCone algorithm. This algorithm doesn’t work for the events with high pile-up activity and it is not CPU efficient. Therefore, SISCone is not suitable for the CMS experiment and it is not recommended as default jet finding algoritm in CMS experiment, but the SISCone algorithm with R = 0.5 and R = 0.7 cone sizes is still supported by the CMS experiment.

2.1.4.3. Anti-k_T Algorithm

Cambridge-Aachen, k_T, anti-k_T algorithms may be given in a single type, the generalized k_T algorithm. A whole family of collinear-safe algorithms and infrared algorithms are the generalized k_T algorithms and these algorithms depending on a continuous parameter, denoted as p (Cacciari et al., 2008). The generalized k_T algorithm is based on a pair-wise recombination and it merges two particles (or calorimeter towers) if their relative P_T is less than a given value. The distance d_{ij} between the particle (or calorimeter tower) i and j, and d_{iB} between i and beam (B) are defined as

$$d_{ij} = min\left(p_{T_i}^2, p_{T_j}^2\right)\frac{\Delta R_{ij}^2}{R^2} \tag{2.10}$$

$$d_{iB} = p_{T_i}^2 \tag{2.11}$$

$$\Delta R_{ij}^2 = \left(y_i - y_j\right)^2 + \left(\Phi_i - \Phi_j\right)^2 \tag{2.12}$$

As can be seen from here, R has a similar role as the cone algorithm and k_T is the momentum of the particle. The following steps illustrate the work steps of the k_T:

I. Make a list of particles.
II. Distances of the d_{ij} and d_{iB} are calculated.
III. If the d_{ij} is the smallest, merge i and j into a single new particle and go back to step I.
IV. Otherwise, if d_{iB} is the smallest, then remove i from the list and go back to step I.
V. Repeat the process until no particles left (Fig. 2.7).

The distance measurement of the d_{ij} and d_{iB} can be generalized as

$$d_{ij} = min\left(p_{T_i}^{2p}, p_{T_j}^{2p}\right)\frac{\Delta R_{ij}^2}{R^2} \tag{2.13}$$

$$d_{iB} = p_{T_i}^{2p} \tag{2.14}$$

where values of p are - 1; 0; 1. These values represent anti-k_T, Cambridge-Aachen and k_T, respectively. The k_T algorithm with p = 1 means that soft particles are clustered firstly (Ellis, 1993). For the p = - 1, anti-k_T algorithm is obtained and hard particles are clustered initially rather than soft particles (Cacciari et al., 2008). If p = 0, as the third and final value, than an energy dependent clustering algorithm called Cambridge/Aachen (CA) algorithm (Dokshitzer, 1997). Fig. 2.8 shows the behavior of the different jet algorithms. The anti-k_T jet algorithm, which can be also seen from the Fig. 2.8, gives the best shape of jets. In addition, the k_T algorithm with cone sizes $\boldsymbol{R}$ = 0.4 and $\boldsymbol{R}$ = 0.6 and the anti-k_T algorithm with cone sizes $\boldsymbol{R}$ = 0.5 and $\boldsymbol{R}$ = 0.7 are supported by CMS.

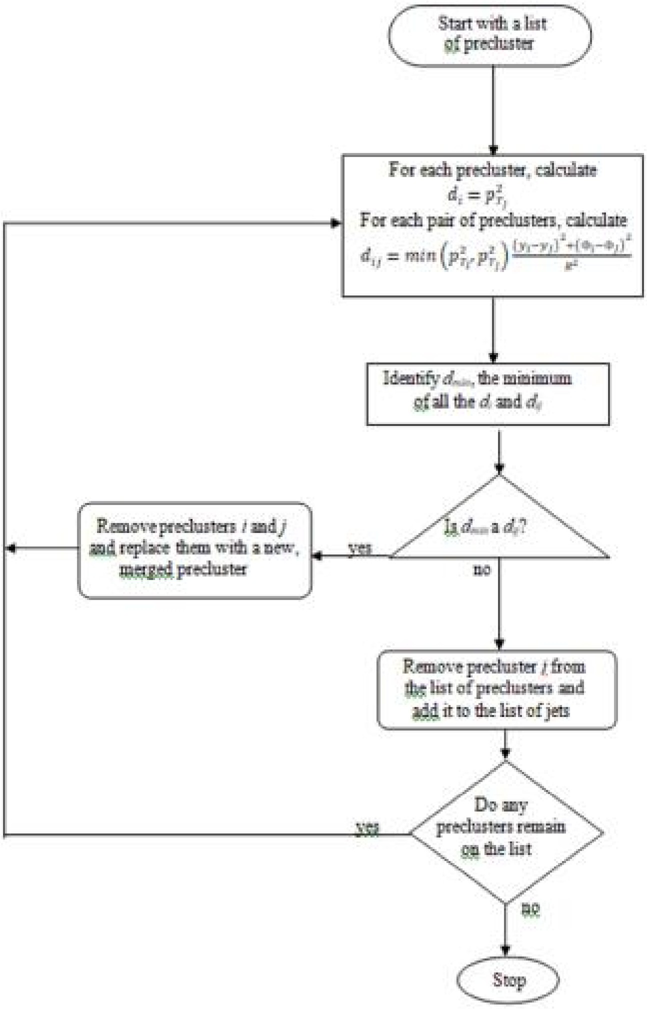

Figure 2.7. A flow chart for the k_T algorithm

2.1.5. Jet Energy Calibration

As discussed previously, the detector jets are reconstructed and measured from the detector inputs, and the energies are different from the particle jets. The difference is coming from non-uniformity of event pileup, detector response and electronicsnoise. The purpose of jet energy calibration is to relate, on average, the measurement of the detector jet to the energy of the corresponding particle jet (Chatrchyan, 2010).

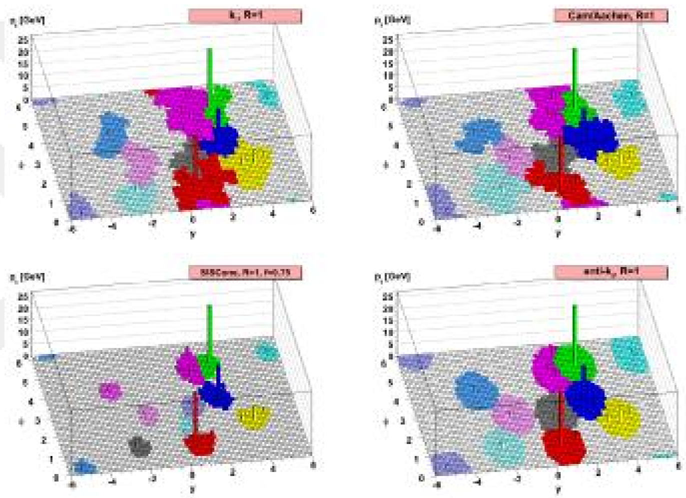

Figure 2.8. Illustration of the behaviors of different jet algorithms at parton level (Cacciari et al., 2008)

The Jet Energy Correction (JEC) scheme which is used at CMS is based on a factorized approach (Chatrchyan et al., 2011). Different sets of correction are defined to study different physical aspects. They are derived in a consecutive way and, as a rule; they could not be completely interrelated and therefore must be applied in the correct order.

The levels (L1, L2, and L3) of corrections defined in the CMS are (Harris, 2007):

- **Level 1 offset corrections,** which requires correction for pile-up and electronic noise;
- **Level 2 relative corrections,** which requires correction for jet response versus η relative to a control region;
- **Level 3 absolute corrections,** which requires correction for jet response versus p_T in the control region;
- **L2L3 residual corrections** that corrects the residual difference between simulation and data after the application levels of L1, L2, L3.

As shown in Fig. 2.9, there is a diagram summarizing the jet energy correction technique in CMS. Starting from the reconstructed raw jets, the order of correction is shown.

The L1 offset corrections are first level correction derived from the MC and applied to both the MC and the data. L1 offset corrections for the data include an additional scale factor which was derived from data driven techniques. L1, L2, and L3 corrections, which represent bulk of the jet energy corrections (JECs), are derived from MC and at the same time are applied to both MC and data. The benefit of relying heavily on simulation to derive the jet energy response is that we can cover corners of phase space that are not easily accessible in data. In Sec. 2.1.5.1.(1), a more detailed description of MC corrections can be found.

After applying these corrections, the comparison between simulation and data shows a residual disagreement. For this reason, an additional set of "Residual corrections" will only be applied to the data to obtain a good data-MC closure. These corrections have been derived using different techniques and different data sets such as multijet, dijet, Z + jets, photon + jets. Subsequently, the results are merged with a global fit to derive the final residual correction factors as a function of η and p_T. Since residual corrections, such as L2 and L3 MC corrections, are aimed to correct the uniformity and absolute energy scale of the response in the detector respectively, L2 is relative and L3 is also referred to as absolute. Further information on the residual JEC will be given in section 2.1.5.1.(2).

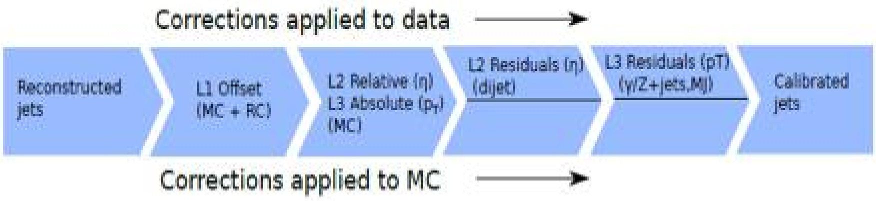

Figure 2.9. The schema of the JEC method in CMS

2.1.5.1 Corrections from Simulation

2.1.5.1.(1) Level 1 Offset Corrections

Pile-up corrections are the most important in terms of "*size*" of the corrections. The purpose of the offset correction is to estimate and deduct the unwanted energy from the jet as an average. In other words, purpose is to subtract the additional energy which is irradiated inside of a jet cone by secondary proton-proton collisions (the pile-up), on an event-by-event basis. However, the method used in CMS subtracts also the additional energy coming from the remnants of the colliding protons, defined as *underlying event* (UE).

In order to do this, a technique called "*jet area method*" is used. This algorithm uses the average energy density by multiplying the effective area in the jets to calculate the offset energy which is deducted with the jets.

The original method uses only the energy density ρ and jet area A_j. At the same time, log (p_T)-dependent and η-dependent terms also have been added to the correction to model better the pile-up and underlying event contribution in different parts of the detector and for different jet energies. The exact correction formula used in CMS is as follows:

$$C_{L1}\left(P_T^{uncorr},\eta,A_{j\rho}\right) = 1 - \frac{\left[\rho_0(\eta)+\rho.\beta(\eta).\left(1+\gamma(\eta).\log(P_T^{uncorr})\right)\right].A_j}{P_T^{uncorr}} \qquad (2.15)$$

where P_T^{uncorr} , η , A_j , ρ are the uncorrected reconstructed jet transverse momentum, jet pseudorapidity, jet area, and the p_T offset density per-event respectively and they are input parameters. Correction of the underlying event intensity is not clearly present in the Eq. 2.15, but is effectively absorbed in $\rho_0(\eta)$. The parameter $\beta(\eta)$, which is called multiplicative factor, corrects for the non-uniformity of the Level-1(offset) versus η and the other parameter $\gamma(\eta)$, which is called the residual correction, adds the logarithmic dependence from jet p_T.

The simulated true offset is determined from the $\gamma(\eta)$, $\rho_0(\eta)$ and $\beta(\eta)$ parameters. The jet *active area* is multiplied by the *effective* energy intensity in square brackets present in Eq. 2.15 (equal to πR^2 in case of anti-k_T jets) and the results is subtracted from the jet's energies. Fig. 2.10 shows pile-up offset before and after L1-Fastjet corrections for *Charged Hadron Subtraction* (CHS) with PF AK4 jets.

After these operations, it will be necessary to add scale factor data/simulation for the corrections to be applied to the data. The scale factor, given in Eq. 2.16, is obtained building a *Random Cone Centered* at (η, Φ) and dividing the mean energy density in the cone in data sample by the actual mean offset in simulation. By the way, data sample is a zero-bias data. Because this data does not contain energy deposition from hard interactions and noise contribution is small.

$$SF = \frac{O_{data}^{RC}(\eta,\langle\rho\rangle_{data})}{O_{MC}^{RC}(\eta,\langle\rho\rangle_{MC})} \tag{2.16}$$

2.1.5.1.(2) Level 2 Relative (η dependence) and Level 3 Absolute (p_T dependence) Corrections

The R_{ptcl}, which is simulated particle response, is defined as the ratio of arithmetic means of matched reconstructed and generated particle-level jets p_T (which is the transverse momentum of the reconstructed jet), in bins of reconstructed η and particle-level transverse momenta.

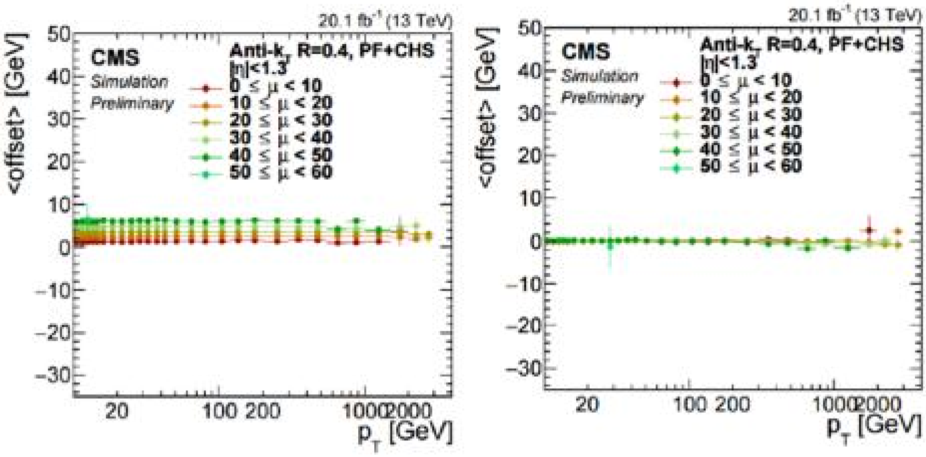

Figure 2.10. Simulated pile-up offset before (Left) and after (Right) L1-Fastjet corrections for CHS with PF ak4 jets in the barrel (|η| < 1.3)

$$R_{ptcl}(\langle p_T\rangle, \eta) = \frac{\langle p_{T,reco}\rangle}{\langle p_{T,ptcl}\rangle}[p_{T,ptcl}, \eta] \quad (2.17)$$

The process of jet matching is done by radial distance, with maximum at half the cone size (for $R = 0.4$ is $\Delta R = 0.2$). This provides highest matching efficiency for anti-k_T jets with unique matches.

The corrections called Level 2 “relative corrections” (L2), are derived first versus η, to uniform the response in the detector. After that, level 3 “absolute corrections” (L3) are derived versus jet p_T after the implementation of the L2 corrections. Fig. 2.11 shows correction factors of MC corrections for different p_T and η values. Fig. 2.12 shows the response after the implementation of L1+L2+L3 corrections for anti-k_T jets with $\boldsymbol{R}$ = 0.4 and CHS.

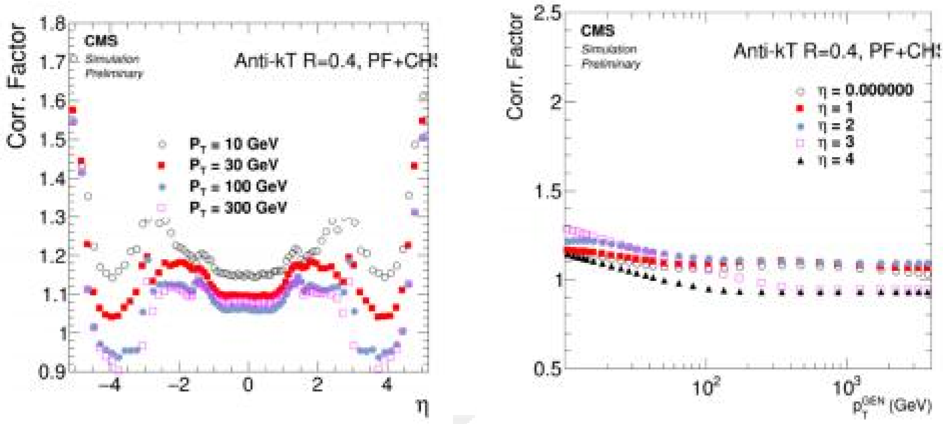

Figure 2.11. L2 Relative jet energy correction (left) and L3 absolute jet energy correction (right) as a function of pseudorapidity

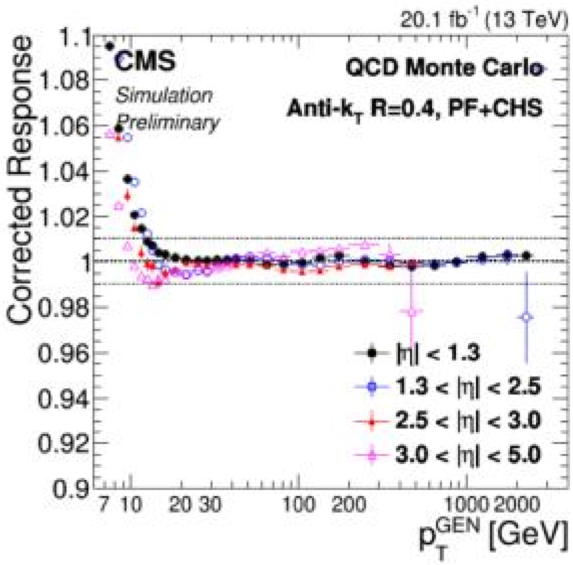

Figure 2.12. Corrected jet response for anti-k_T jets with CHS and R = 0.4 versus jet p_T

2.1.5.2. Corrections from Data

After the jets for pile-up and simulated particle response are corrected, the remaining data/simulation scale factors for JEC are determined (The CMS Collaboration, 2017). At the same time, corrections need to be propagated to missing p_T and E_T. These corrections for data are first determined with low statistical uncertainty dijet sample relative to |η|<1.3 over a wide range of p_T. This case gives a relative scale factor, and hence characterizes the L2 relative corrections, as a function of jet pseudorapidity. The scale of L3 absolute residual corrections is obtained from a combination of Z → μμ + jet, Z → ee + jet, γ + jet and multijet events for jets with |η| <1.3 in a more limited range of p_T from around 30 GeV and 1 TeV. The fundamental idea is to use the transverse momentum balance at the hard-scattering level, between the reference object and the jet to be calibrated: a jet energy scale that is different from the unity produces imbalance at the reconstruction level.

The jet energy response was investigated by using the MPF (Missing transverse momentum Projection Fraction) and p_T balance methods. According to the p_T balancing technique, absolute jet energy correction is considering the balance in the transverse plane between the photon and the recoiling jet. The photon that used as a reference object is precisely measured in the ECAL calorimeter. Additionally, according to MPF technique which is the fundamental technique for absolute jet energy correction of CMS, considers that the γ + jet events have no real missing E_T and therefore there is a perfect balance between the photon and the hadronic recoil in the transverse plane:

$$\vec{P}_T^{\gamma} + \vec{P}_T^{recoil} = 0 \tag{2.18}$$

This equation can be rewritten for the reconstructed objects as below,

$$R_{\gamma}\vec{P}_T^{\gamma} + R_{recoil}\vec{P}_T^{recoil} = -\vec{E}_T^{miss} \tag{2.19}$$

where R_{recoil} and R_{γ} are response of detector to the hadronic recoil and response of detector to the photon, respectively. If the photons are well calibrated, $R\gamma$ =1, after solving of the above two equations R_{recoil} gives the definition of the MPF response that principal technique for the absolute correction.

$$R_{recoil} = 1 + \frac{\vec{E}_T^{miss}.\vec{P}_T^{\gamma}}{(\vec{P}_T^{\gamma})^2} = \frac{R_{recoil}}{R_{\gamma}} = R_{MPF} \tag{2.20}$$

Fig. 2.13 shows MPF response and response of $< p_T / p_\gamma >$, in data and MC for PF jets as a function of photon p_T. Fig. 2.13 also shows the one-parameter linear fit function and Data/MC ratios, at the bottom plots. The bottom plot shows the one-parameter linear fit function and Data/MC ratio (CMS Collaboration, 2010).

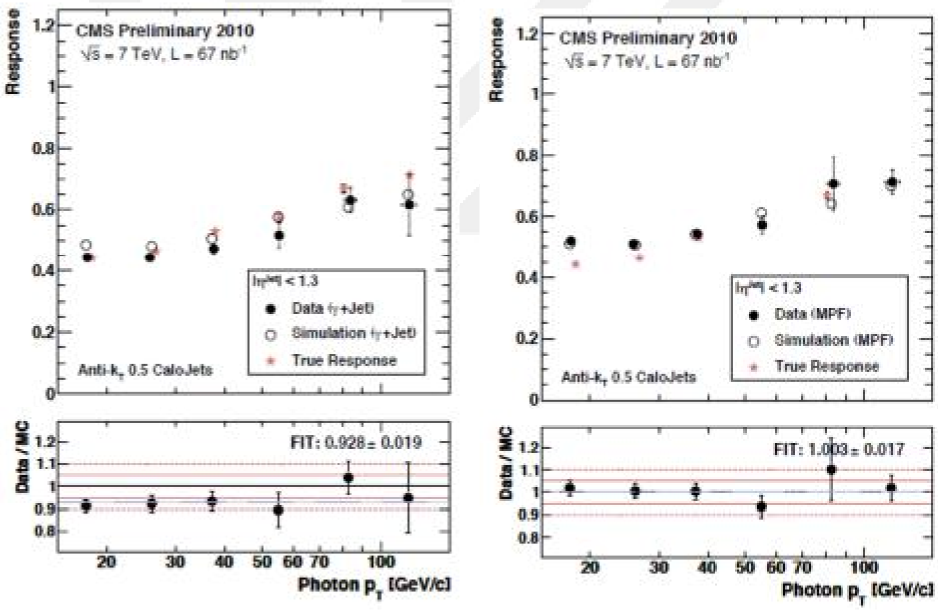

Figure 2.13. The response of the $< p_T / p_\gamma >$ (left) and MPF response (right) as a function of photon p_T from data and MC for PF jets

2.2. Data Sample and Selection Criteria

2.2.1. Dataset and Trigger Selection

In this study, the data collected by the PF scouting streams during 25 ns proton-proton collisions were used. Then scouting triggers were implemented through RunD. In this study three streams of data were used;

- for dijet mass data,
- to obtain the trigger efficiency,
- to compare scouting jets to fully reconstructed jets.

The dataset is splitted according to data taking periods and the dataset names, run ranges, the relative integrated luminosity, and their details are summarized in Table 2.2.

Firstly, H_T > 450 GeV trigger at the HLT was used for the PF scouting stream. When an event passes the scouting trigger the objects reconstructed at the HLT trigger are recorded directly bypassing the normal reconstruction. The objects from the event are stored in special scouting data formats designed to reduce the event size and provide long-term accessibility of the data.

Table 2.2. Scouting sub-dataset and their integrated luminosity

Purpose	Dataset	Run range	Luminosity
Mass data	/ScoutingPFHT/Run2015D-v1/RAW	257968 -260858	1914 pb^{-1}
Trigger efficiency	/ScoutingPFCommissioning/Run2015D-v1/RAW	257968 - 260858	1913 pb^{-1}
HLT–RECO comparison	/ParkingScoutingMonitor/Run2015D-v1/RAW	257933 - 260858	
HLT–RECO comparison	/ParkingScoutingMonitor/Run2015D-PromptReco-v4/MINIAOD	258159 - 260858	

Four-momenta of the AK4 PF jets is stored with other information used for identification (e.g., constituent energies and multiplicities). Any pileup reduction wasn't applied on the scouting jets. The average event sizes for PF scouting, MiniAOD and RAW data are 9 kB, 20 kB and 400 kB, respectively.

The dataset of the commisioning includes only scouting events which have got prescaled triggers to measure the trigger efficiency of the primary dataset. However, the data sets of monitoring include scouting objects in the RAW data set and objects that are completely reconstructed for the same events in the MiniAOD data sets.

The data, which reconstructed at the HLT, analyzed using CMSSW 7_4_X. The good runs and luminosity sections were selected based on silver JSON files[1]. The integrated luminosity of the selected data sample is 1.9 fb^{-1}.

The unprescaled trigger path that collects most of the events at high dijet mass, interesting for this study is the H_T > 450 GeV, based on the scalar sum of the calojets reconstructed at HLT. The HLT trigger turn-on as a function of the reconstructed mass of the dijet system m_{jj}^{Wide} is measured using a loose reference trigger based on H_T calculated at L1. This L1HT path reference trigger threshold varies between 125 GeV to 175 GeV, depending on the LHC luminosity. These trigger paths are shown in Table 2.3. There are two versions of the trigger paths, as it can be seen in the Table 2.3, because of technical reasons: while one does not include the bTag sequence in the PF, the other one does. The bTag sequence fails for a very small fraction of events and this causes rejection of this event. Only a single HT450 path with bTag sequence was active during the first period of data taking (for run numbers < 259636). In order to cover the full run range, in this study we use the OR of all the L1 triggers (called L1HT150) as reference trigger and the OR of all the HLT triggers (called HT450) for the main trigger.

[1] https://cms-service-dqm.web.cern.ch/cms-service-dqm/CAF/certification/Collisions15/13TeV/Cert_246908-260627_13TeV_PromptReco_Collisions15_25ns_JSON_Silver.txt

Table 2.3. Trigger paths for different run periods

Trigger name	Definition	Note
DST_L1HTT125ORHTT150ORHTT175_PFReco_PFBTagCSVReco_PFScouting_v* (257933 ≤ *run* < 259636)	L1caloHT > 125-175 GeV	L1seed for Btag PF scouting path and reference for HLT trigger turn-on
DST_CaloJet40_BTagScouting_v* (*run* ≥ 259636)	L1caloHT > 125-175 GeV	L1seed for Btag PF scouting path and reference for HLT trigger turn-on
DST_L1HTT_CaloScouting_PFScouting_v* (*run* ≥ 259636)	L1caloHT > 125-175 GeV	L1seed for PF scouting paths and reference for HLT trigger turn-on
DST_HT450_PFReco_PFBTagCSVReco_PFScouting_v* (257933 ≤ *run* < 259636)	HLTcaloHT > 450 GeV	unprescaled, Btag sequence
DST_HT450_BTagScouting_v* (*run* ≥ 259636)	HLTcaloHT > 450 GeV	unprescaled, Btag sequence
DST_HT450_PFScouting_v* (*run* ≥ 259636)	HLTcaloHT > 450 GeV	unprescaled

These triggers are basic triggers which were used for many physics researches beyond SM.

The trigger efficiency was generated as a function of m_{jj}^{Wide} using the dijet mass variable binning. The denominators are events firstly passing the full dijet event selection and then passing the L1HT150 trigger. The numerators are events likewise firstly passing the same selection of the denominator and then are required also to pass the HT450 trigger selection. The histograms of the numerator and denominator are illustrated in Fig. 2.14. (Left). The measurement of the trigger turn-on is illustrated in Fig. 2.14. (Right) and it is obtained using the **ROOT 6.02.00** class TEfficiency with the "SetStatisticOption(TEfficiency::kFWilson)" option. The data were fitted with the following parametrization (Eq. 2.21) in the range of 453-890 GeV, using the Fit() method of the TEfficiency class which takes into account the binomial statistics for an efficiency measurement.

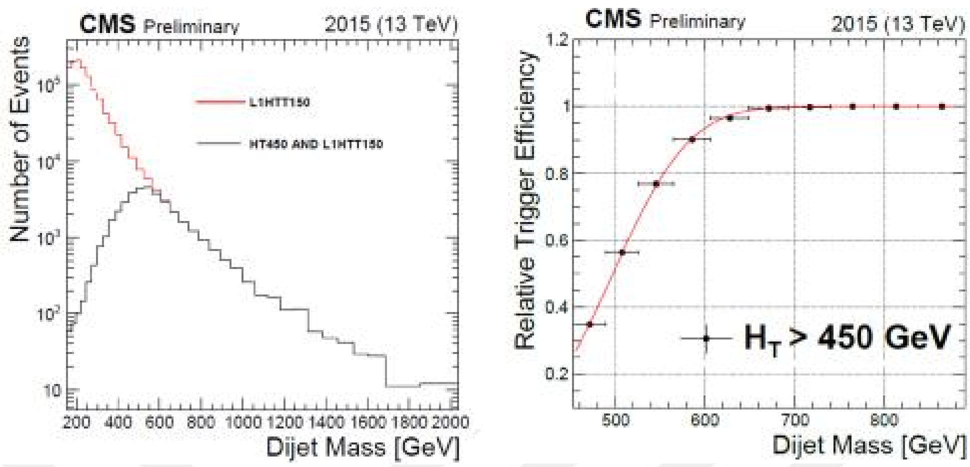

Figure 2.14. Variable binning, Left: The m_{jj}^{Wide} distributions of events in the data passing the full dijet event selection plus the trigger selection (all events are required to pass at least the L1HT150 prescaled, monitoring trigger), Right: Trigger turn-on of HT450 as a function of m_{jj}^{Wide} (The reference trigger used is L1HT150)

$$\epsilon = \frac{1}{2}\left(1 + erf\left(\frac{m_{jj}^{Wide} - m_{eff}}{\sigma_{eff}}\right)\right) \quad (2.21)$$

The fitted parameters are found as σ_{eff} = 95.8 ± 1.2 GeV and m_{eff} = 496.92 ± 0.56 GeV. The same fit was repeated using 1 GeV bins instead of variable binning, and the results are shown in Fig. 2.15. The fitted parameters in case of 1 GeV bins histograms are σ_{eff} = 96.0 ± 1.1 GeV and m_{eff} = 495.66 ± 0.55 GeV and they seem to be consistent with the previous ones.

The turn on curve of the trigger becomes fully efficient when the dijet mass is greater than about 670 GeV and they are shown in Fig. 2.14 and Fig. 2.15 (right figures). Thus the fit to the dijet mass spectrum for background estimate is started around this point and the full efficient mass region is considered. In this study, energy around 670 GeV is effectively the lowest energy used for discovery search for new physics in dijet final state at center-of-mass energy of 13 TeV.

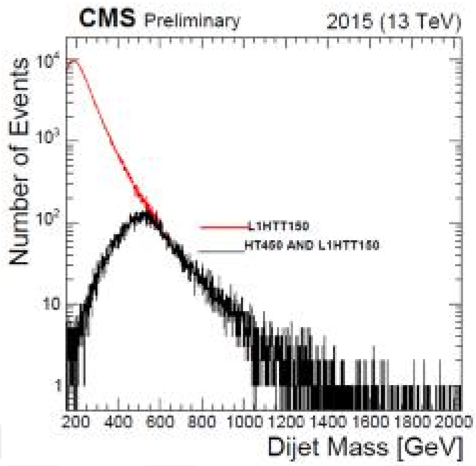

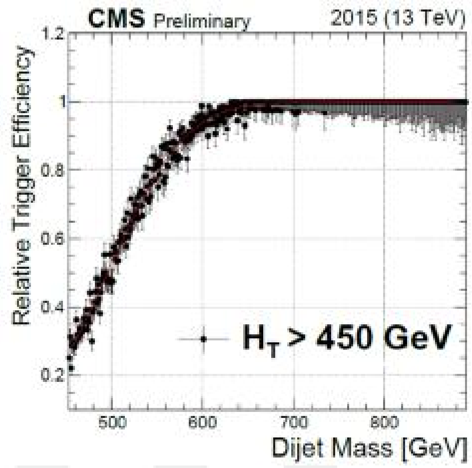

Figure 2.15. 1 GeV binning, Left: The m_{jj}^{Wide} distributions of events in data passing the full dijet event selection plus the trigger selection (all events are required to pass at least the L1HT150 prescaled, monitoring trigger), Right: Trigger turn-on of HT450 as a function of m_{jj}^{Wide} (The reference trigger used is L1HT150)

2.2.2. Monte Carlo Simulation

The MC data, centrally produced for RunIISpring15 campaign, was used in this study. The GEN-SIM and the DIGI-RECO were produced using CMSSW 7_1_ X and CMSSW 7_4_X, respectively. The signal and background samples were generated with PYTHIA 8 (Sjostrand et al., 2008) using CUETP8M1 tune. These samples were produced using 25 ns bunch crossing spacing and average of 20 pile-up interactions. These values are mimics the LHC conditions. All events were passed full simulation of CMS detector which is based on GEANT4.

2.2.2.1. Signal

The signal samples of the MC simulation were generated via PYTHIA 8 (Sjostrand et al., 2008) using CUETP8M1 tune, with the same LHC conditions. However, the shapes are passed through a full simulation of the CMS detector based on GEANT4.

The signal samples are produced with narrow resonances (in other words, the resonance width was adjusted to be smaller than the experimental mass resolution in order to minimize detector effects) (Khachatryan et al., 2010). According to previous researches it is known that the shape of a narrow resonance is essentially determined by the combination of partons in the initial and final states. Possible productions of the signal are consisting of three different decay modes and are given as follows:

- $\mathrm{gg} \rightarrow \mathrm{RS\ Graviton(G)} \rightarrow \mathrm{gg}$
- $\mathrm{qq} \rightarrow \mathrm{RS\ Graviton(G)} \rightarrow \mathrm{qq}$
- $\mathrm{qg} \rightarrow \mathrm{excited\ quark(q^*)} \rightarrow \mathrm{qg}$

where any quark/antiquark is denoted by “q” and gluons are denoted by “g”. For each of these processes, there are eleven samples at eleven different mass points between 500 GeV and 9 TeV, and about 100,000 events per sample. The dataset used in these studies are given in Table 2.4.

2.2.2.2. Background

The MC samples used for the QCD multijet background studies are generated with PYTHIA 8 using CUETP8M1 tune. These samples are binned in transverse momentum (p_T) starting at 50 GeV. The list of MC dataset for QCD background in RunIISpring15 with number of events, corresponding cross section and integrated luminosity are given in Table 2.5.

Table 2.4. The MC dataset for dijet resonances in RunIISpring15 with numbers of events

Dataset	Events
/RSGravitonToGluonGluon_kMpl01_M_500_TuneCUETP8M1_13TeV_pythia8/RunIISpring15MiniAODv2-74X_mcRun2_asymptotic_v2-v1/MINIAODSIM	99 600
/RSGravitonToGluonGluon_kMpl01_M_750_TuneCUETP8M1_13TeV_pythia8/RunIISpring15MiniAODv2-Asympt25ns_74X_mcRun2_asymptotic_v2-v1/MINIAODSIM	100 000
/RSGravitonToGluonGluon_kMpl01_M_1000_TuneCUETP8M1_13TeV_pythia8/RunIISpring15MiniAODv2-74X_mcRun2_asymptotic_v2-v1/MINIAODSIM	91 605
/RSGravitonToGluonGluon_kMpl01_M_2000_TuneCUETP8M1_13TeV_pythia8/RunIISpring15MiniAODv2-74X_mcRun2_asymptotic v2-v1/MINIAODSIM	99 425
/RSGravitonToGluonGluon_kMpl01_M 3000_TuneCUETP8M1_13TeV_pythia8/RunIISpring15MiniAODv2-74X_mcRun2_asymptotic v2-v1/MINIAODSIM	100 000
/RSGravitonToGluonGluon_kMpl01_M 4000_TuneCUETP8M1_13TeV_pythia8/RunIISpring15MiniAODv2-74X_mcRun2_asymptotic v2-v1/MINIAODSIM	100 000
/RSGravitonToGluonGluon_kMpl01_M 5000_TuneCUETP8M1_13TeV_pythia8/RunIISpring15MiniAODv2-74X_mcRun2_asymptotic v2-v1/MINIAODSIM	100 000
/RSGravitonToGluonGluon_kMpl01_M 6000_TuneCUETP8M1_13TeV_pythia8/RunIISpring15MiniAODv2-74X_mcRun2_asymptotic v2-v1/MINIAODSIM	100 000
/RSGravitonToGluonGluon_kMpl01_M 7000_TuneCUETP8M1_13TeV_pythia8/RunIISpring15MiniAODv2-74X_mcRun2_asymptotic v2-v1/MINIAODSIM	100 000
/RSGravitonToGluonGluon_kMpl01_M 8000_TuneCUETP8M1_13TeV_pythia8/RunIISpring15MiniAODv2-74X_mcRun2_asymptotic v2-v1/MINIAODSIM	98670
/RSGravitonToGluonGluon_kMpl01_M 9000_TuneCUETP8M1_13TeV_pythia8/RunIISpring15MiniAODv2-74X_mcRun2_asymptotic v2-v1/MINIAODSIM	99 689
/RSGravitonToQuarkQuark_kMpl01_M_500_TuneCUETP8M1_13TeV_pythia8/RunIISpring15MiniAODv2-74X_mcRun2_asymptotic_v2-v1/MINIAODSIM	100 000
/RSGravitonToQuarkQuark_kMpl01_M_750_TuneCUETP8M1_13TeV_pythia8/RunIISpring15MiniAODv2-Asympt25ns_74X_mcRun2_asymptotic_v2-v1/MINIAODSIM	100 000
/RSGravitonToQuarkQuark_kMpl01_M_1000_TuneCUETP8M1_13TeV_pythia8/RunIISpring15MiniAODv2-74X_mcRun2_asymptotic_v2-v1/MINIAODSIM	95 960
/RSGravitonToQuarkQuark_kMpl01_M_2000_TuneCUETP8M1_13TeV_pythia8/RunIISpring15MiniAODv2-74X_mcRun2_asymptotic_v2-v1/MINIAODSIM	99 728
/RSGravitonToQuarkQuark_kMpl01_M_3000_TuneCUETP8M1_13TeV_pythia8/RunIISpring15MiniAODv2-74X_mcRun2_asymptotic_v2-v1/MINIAODSIM	100 000
/RSGravitonToQuarkQuark_kMpl01_M_4000_TuneCUETP8M1_13TeV_pythia8/RunIISpring15MiniAODv2-74X_mcRun2_asymptotic_v2-v1/MINIAODSIM	95 055
/RSGravitonToQuarkQuark_kMpl01_M_5000_TuneCUETP8M1_13TeV_pythia8/RunIISpring15MiniAODv2-74X_mcRun2_asymptotic_v2-v1/MINIAODSIM	100 000
/RSGravitonToQuarkQuark_kMpl01_M_6000_TuneCUETP8M1_13TeV_pythia8/RunIISpring15MiniAODv2-74X_mcRun2_asymptotic_v2-v1/MINIAODSIM	99 631
/RSGravitonToQuarkQuark_kMpl01_M_7000_TuneCUETP8M1_13TeV_pythia8/RunIISpring15MiniAODv2-74X_mcRun2_asymptotic_v2-v1/MINIAODSIM	99 724
/RSGravitonToQuarkQuark_kMpl01_M_8000_TuneCUETP8M1_13TeV_pythia8/RunIISpring15MiniAODv2-74X_mcRun2_asymptotic_v2-v1/MINIAODSIM	99 956
/RSGravitonToQuarkQuark_kMpl01_M_9000_TuneCUETP8M1_13TeV_pythia8/RunIISpring15MiniAODv2-74X_mcRun2_asymptotic_v2-v1/MINIAODSIM	100 000

Table 2.4. Continue

/QstarToJJ_M_500_TuneCUETP8M1_13TeV_pythia8/RunIISpring15MiniAODv2-74X_mcRun2_asymptotic_v2-v1/MINIAODSIM	99 316
/QstarToJJ_M_750_TuneCUETP8M1_13TeV_pythia8/RunIISpring15MiniAODv2-Asympt25ns_74X_mcRun2_asymptotic_v2-v1/MINIAODSIM	97 790
/QstarToJJ_M_1000_TuneCUETP8M1_13TeV_pythia8/RunIISpring15MiniAODv2-74X_mcRun2_asymptotic_v2-v1/MINIAODSIM	100 000
/QstarToJJ_M_2000_TuneCUETP8M1_13TeV_pythia8/RunIISpring15MiniAODv2-74X_mcRun2_asymptotic_v2-v1/MINIAODSIM	100 000
/QstarToJJ_M_3000_TuneCUETP8M1_13TeV_pythia8/RunIISpring15MiniAODv2-74X_mcRun2_asymptotic_v2-v1/MINIAODSIM	100 000
/QstarToJJ_M_4000_TuneCUETP8M1_13TeV_pythia8/RunIISpring15MiniAODv2-74X_mcRun2_asymptotic_v2-v1/MINIAODSIM	99 676
/QstarToJJ_M_5000_TuneCUETP8M1_13TeV_pythia8/RunIISpring15MiniAODv2-74X_mcRun2_asymptotic_v2-v1/MINIAODSIM	99 915
/QstarToJJ_M_6000_TuneCUETP8M1_13TeV_pythia8/RunIISpring15MiniAODv2-74X_mcRun2_asymptotic_v2-v1/MINIAODSIM	100 000
/QstarToJJ_M_7000_TuneCUETP8M1_13TeV_pythia8/RunIISpring15MiniAODv2-74X_mcRun2_asymptotic_v2-v1/MINIAODSIM	100 000
/QstarToJJ_M_8000_TuneCUETP8M1_13TeV_pythia8/RunIISpring15MiniAODv2-74X_mcRun2_asymptotic_v2-v1/MINIAODSIM	99 799
/QstarToJJ_M_9000_TuneCUETP8M1_13TeV_pythia8/RunIISpring15MiniAODv2-74X_mcRun2_asymptotic_v2-v1/MINIAODSIM	99 762

Table 2.5. The MC data set for QCD multijet background in RunIISpring15 with cross sections, numbers of events, and equivalent integrated luminosities generated with PYTHIA8, tune CUETP8M1

Dataset	Cross section [pb]	Events	Equivalent Luminosity [fb^{-1}]
/QCD_Pt_50to80_TuneCUETP8M1_13TeV_pythia8/RunIISpring15MiniAODv2-74X_mcRun2_asymptotic_v2-v1/MINIAODSIM	19204300	4 983 675	2.595×10^{-4}
/QCD_Pt_80to120_TuneCUETP8M1_13TeV_pythia8/RunIISpring15MiniAODv2-74X_mcRun2_asymptotic_v2-v1/MINIAODSIM	2762530	3 450 293	0.001249
/QCD_Pt_120to170_TuneCUETP8M1_13TeV_pythia8/RunIISpring15MiniAODv2-74X_mcRun2_asymptotic_v2-v1/MINIAODSIM	471100	3 458 385	0.007341
/QCD_Pt_170to300_TuneCUETP8M1_13TeV_pythia8/RunIISpring15MiniAODv2-74X_mcRun2_asymptotic_v2-v1/MINIAODSIM	117276	3 364 368	0.02869
/QCD_Pt_300to470_TuneCUETP8M1_13TeV_pythia8/RunIISpring15MiniAODv2-74X_mcRun2_asymptotic_v2-v1/MINIAODSIM	7823	2 935 633	0.3753
/QCD_Pt_470to600_TuneCUETP8M1_13TeV_pythia8/RunIISpring15MiniAODv2-74X_mcRun2_asymptotic_v2-v1/MINIAODSIM	648.2	1 937 537	2.989
/QCD_Pt_600to800_TuneCUETP8M1_13TeV_pythia8/RunIISpring15MiniAODv2-74X_mcRun2_asymptotic_v2-v1/MINIAODSIM	186.9	1 964 128	10.51
/QCD_Pt_800to1000_TuneCUETP8M1_13TeV_pythia8/RunIISpring15MiniAODv2-74X_mcRun2_asymptotic_v2-v1/MINIAODSIM	32.293	1 937 216	59.99
/QCD_Pt_1000to1400_TuneCUETP8M1_13TeV_pythia8/RunIISpring15MiniAODv2-74X_mcRun2_asymptotic_v2-v1/MINIAODSIM	9.4183	1 487 136	157.9
/QCD_Pt_1400to1800_TuneCUETP8M1_13TeV_pythia8/RunIISpring15MiniAODv2-74X_mcRun2_asymptotic_v2-v1/MINIAODSIM	0.84265	197 959	233.8
/QCD_Pt_1800to2400_TuneCUETP8M1_13TeV_pythia8/RunIISpring15MiniAODv2-74X_mcRun2_asymptotic_v2-v1/MINIAODSIM	0.114943	193 608	1.684×10^{3}
/QCD_Pt_2400to3200_TuneCUETP8M1_13TeV_pythia8/RunIISpring15MiniAODv2-74X_mcRun2_asymptotic_v2-v1/MINIAODSIM	0.00682981	194 456	2.847×10^{4}
/QCD_Pt_3200toInf_TuneCUETP8M1_13TeV_pythia8/RunIISpring15MiniAODv2-74X_mcRun2_asymptotic_v2-v1/MINIAODSIM	0.000165445	192 944	1.166×10^{6}

2.2.3. Selection Criteria

2.2.3.1. Jets Selection and Wide Jet Algorithm

The events with at least two jets were selected in the dijet analysis. These jets were reconstructed at the HLT level using the anti-k_T clustering algorithm (Cacciari, 2008) with cone size parameter $R = \sqrt{(\Delta\eta)^2 + (\Delta\Phi)^2} = 0.4$ (PF ak4 jets) in the y-Φ plane, that have been discussed in detail in Chapter 1. As it is seen, this description satisfies the infrared and collinear safety requirements. Also, the jet energy was corrected using MC and database techniques to take into account the irregularity of the response throughout the detector, the pile-up extra energy and the permanent differences in the exact scale of the energy between the MC and data. The inputs to the anti-k_T algorithm were the Lorentz 4-vectors of the reconstructed PF candidates (CMS Collaboration, 2009). The resulting PF jets were required a small additional jet energy correction (JEC) to account for the neutral hadron component of the jet shower measured by HCAL with non-homogeneous response. For this reason, the following jet energy corrections have been applied for HLT jets in this study.

1. MC truth corrections:
   74X_HLT_mcRun2_asymptotic_fromSpring15DR_v0_MC (L1L2L3)
2. Residual corrections determined from in-situ reco data: Summer15_25nsV7 (L2L3Residual)

Jet quality criteria (Jet ID) was developed by the CMS for the particle flow jets and its benefits are given as follow:

- it is rejecting most fake jets arising from the HCAL and ECAL calorimeters and/or readout electronics noise.
- it preserves the vast majority of real jets in the simulation.

These criterias are examined in pure noise non-collision data samples such as cosmic trigger data or data from triggers on empty bunches during LHC process. Jets used in the study were required to satisfy the "Tight" PF Jet ID selection criteria.

- Neutral Hadron Fraction (NHF) < 0.90
- Neutral Electro-Magnetic Energy Fraction (NEMF) < 0.90
- Number of Constituents (NumConst) >1
- Muon Fraction (MUF) < 0.8

however, for jets in $|\eta| \leq 2.4$ also following criterias that involve the tracks information were required:

- Charged Hadron Fraction (CHF) > 0
- Charged Multiplicity (CHM) > 0
- Charged Electro-Magnetic Fraction (CEMF) < 0.9

These additional criterias are taken from the link[2]. Based on the studies on the early 13 TeV Minimum-Bias dataset, these criterias have a background rejection of 84% and an efficiency of 99%. Events are rejected if one of the following two conditions occurs:

I. If at least one of the leading (in p_T) AK4 jets does not pass the tight jetID.
II. or if at least one of the two leading jets is outside of the tracker acceptance ($|\eta| < 2.5$).

[2]https://twiki.cern.ch/twiki/bin/viewauth/CMS/JetID#Recommendations_for_13_TeV_data

Additionally, if at least one of the two leading jets has a Muon Energy Fraction> 0.8, then the events are rejected again. This cut has been used in run1 analysis to eliminate mis-reconstructed muons identified as jet which cause large non-physical tails in dijet mass distribution. The inefficiency of this cut for our study is found to be negligible.

The leading (second leading) jet is required to have $P_T > 60\ (30)$ GeV and to be within the coverage region of the tracker $|\eta| < 2.5$. The two leading jets are then used as seeds to aggregate the other calibrated particle flow jets with $P_T > 30$ GeV, $|\eta| < 2.5$ and passing the tight PF Jet ID within $\Delta R = \sqrt{(\Delta\eta)^2 + (\Delta\Phi)^2} <$ 1.1. Fig. 2.16 shows an illustration of the wide jet. Detailed information about the wide jet algorithm can be found at (Gouzevitch et al., 2011).

The corrected PF AK4 jets that pass the selection described above are not only clustered in a larger cone but they also used to reconstruct the invariant mass of the dijet system. This provides the energy of the hadrons to be stored better in the presence of the final state radiation (FSR). Therefore allows, by increasing the dijet mass resolution, the resonance peak to be both closer to the nominal mass and narrower.

The wide jets are obtained using PF AK4 jets as inputs by following procedures:

- Two PF AK4 jets with the highest P_T (leading jets) are taken as “seeds” of the wide jets and form two “temporary” wide jets $wj_1$and wj_2;
- For each PF AK4 jet j_i decide whether it is geometrically close to the first wide jet (wj_1) or second wide jet wj_2 by comparing $\Delta R_{i\ 1,2}$ between j_i and $wj_{1,2}$;

in this case following two situations can arise:

1. If $\Delta R_{i1} < \Delta R_{i2}$ and $\Delta R_{i1} < 1.1$ then sum the j_i to the first temporary wide jet wj_1.
2. If the first condition is not satisfied and if $\Delta R_{i2} < \Delta R_{i1}$ and $\Delta R_{i2} < 1.1$ then sum the j_i to the second temporary wide jet wj_2.

This algorithm continues in this way, and eventually the two final wide jets are rearranged in p_T. The resulting wide jets have the proper jet energy correction as main jet. Also, the choice of input jets in p_T behaves like a "pruning" algorithm which reduces the contribution of pile-up and softer jets.

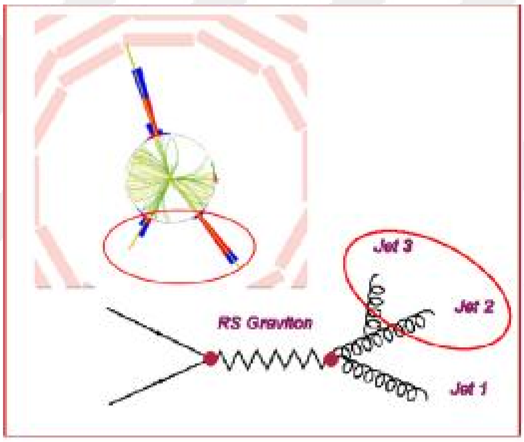

Figure 2.16. Wide jets made by combining PF jets

2.2.3.2. Event Selection

The events are selected requiring at least one reconstructed primary vertex within $|PVz| < 24$ cm from center of the detector along the z direction. This cut ensures that the jets are close to the center of the calorimeter. The number of primary collision vertex required to be $nPV \geq 1$. The number of degrees of freedom must be greater than three ($PVndof > 3$) to correctly select the reconstructed vertices.

Finally, both wide jets were required to satisfy the requirements of the following η cuts: $|\eta_1| < 2.5$, $|\eta_2| < 2.5$ and $\left|\Delta\eta_{jj}^{Wide}\right| = |\eta_1 - \eta_2| < 1.3$. This selection made for following purposes:

- It is the main cut for analysis to reduce the background and enhance the significance of the signal. The cut given as $|cos\theta^*| = |\tanh(\Delta\eta/2)| < 0.57$ (where θ^* is the scattering angle) also suppres the QCD events (*t*-channel production) since these events has angular distribution which peaks at $|cos\theta^*| = 1$. On the other hand resonances (s-channel production) have an angular distribution that is significantly flat in $cos\theta^*$ and not affected much from this cut.
- It defines a fiducial region for our measurement predominantly in the barrel.
- It provide a faster trigger turn-on curve for the jet trigger which uses H_T (scalar sum of jet P_T), allowing us to start the analysis at lower mass.

2.2.4. HLT to Reco Calibration

Since the data in the scouting stream were stored with a reduced event content of approximately 10 kB, only the main objects such as photons, jets and MET were recorded. All of these main objects were reconstructed online with HLT, the raw data was not saved, and so no offline reconstruction was possible. Different clustering algorithms can be used to cluster the partons into jets. The CMS uses the anti-k_T algorithm, with a distance parameter (*R*) of 0.4 for PF AK4 jets. The HLT clustering algorithm had to be faster than in the standard full reconstruction in order to satisfy the tight timing requirements at the trigger level. In this fast process it is possible that the jet energy is not fully reconstructed or the pile-up is not properly taken in account. For this reason it was very important for this analysis to correct the HLT jet energy or equivalently the HLT dijet invariant mass (m_{jj}) and brought it back to true value. For this purpose a specific dataset were used. For this set, both HLT and RECO (full reconstruction) jet were recorded for same events. Details of the data sets used for this study are given in Table 2.6 and Table 2.7.

Table 2.6. Dataset containing HLT jets and RECO jets

Dataset	Objects
/ParkingScoutingMonitor/Run2015D-PromptReco-v4/RAW	HLT Jets
/ParkingScoutingMonitor/Run2015D-PromptReco-v4/MINIAOD	RECO Jets

Table 2.7. The triggers available in the Parking Scouting Monitor dataset

Label	Path
ZeroBias	DST_ZeroBias_PFScouting DST_ZeroBias_BTagScouting
DoubleMu	DST_L1DoubleMu_BTagScouting DST_L1DoubleMu_PFScouting
CaloJet40	DST_CaloJet40_PFReco_PFBTagCSVReco_PFScouting DST_CaloJet40_BTagScouting DST_CaloJet40_CaloScouting_PFScouting
L1HT	DST_L1HTT125ORHTT150ORHTT175_PFReco_PFBTagCSVR eco_PFScouting DST_L1HTT_BTagScouting DST_L1HTT_CaloScouting_PFScouting
HT250	DST_HT250_CaloScouting
HT450	DST_HT450_PFReco_PFBTagCSVReco_PFScouting DST_HT450_BTagScouting DST_HT450_PFScouting

The first set of JEC was applied to cure the effects due to presence of pile-up and non-homogeneity of the detector. The latest RECO JEC was used for the RECO jets. However, for the HLT jets a set of JEC based on the MC simulation and additionally the same residual corrections of the RECO jets were applied. See Table 2.8 for further details.

The events for calculation of HLT-to-Reco corrections were selected according to Table 2.9.

HLT-to-Reco corrections based on the dijet invariant mass were calculated for the initial state of the analysis. The data set was divided into two parts to calculate the corrections using one part and to perform the closure test on the other part. The main variable that has been def ined in Eq. 2.22 used to calculate the differences in invariant mass between the HLT and the RECO jets.

Table 2.8. Jet energy corrections applied on RECO jets and HLT jets

JEC applied on RECO jets
Summer15_25nsV7_DATA_L1FastJet Summer15_25nsV7_DATA_L2Relative Summer15_25nsV7_DATA_L3Absolute Summer15_25nsV7_DATA_L2L3Residual
JEC applied on HLT jets
74X_HLT_mcRun2_asymptotic_fromSpring15DR_v0_L1FastJet 74X_HLT_mcRun2_asymptotic_fromSpring15DR_v0_L2Relative 74X_HLT_mcRun2_asymptotic_fromSpring15DR_v0_L3Absolute Summer15_25nsV7_DATA_L2L3Residual

Table 2.9. Event selection

HLT and Reco jets common cuts	
AK4 jets	P_T (leading jet) > 60 GeV P_T (sub-leading jet)> 30 GeV |η|< 2.5
Widejets	P_T (leading widejet) > 60 GeV P_T (sub-leading widjet)> 30 GeV |η|< 2.5
Additional cuts on HLT quantities	
m(*jj*) > 400 GeV	
$\Delta\eta(jj) < 1.3$	

$$Bias = \frac{m_{jj}(RECO) - m_{jj}(HLT)}{m_{jj}(HLT)} \quad (2.22)$$

In order to avoid any bias due to selection of trigger, this variable was calculated as a function of m_{jj} for different type of triggers. Essentially, distributions are not fully efficient because they have different slope due to the trigger selection cuts. If two triggers give different slopes, then the most reliable trigger is the trigger with the looser selection. On the other hand if they give same slope, then the trigger which have the largest statistics is used. The m_{jj} bias as a function of the dijet invariant mass for the different usable trigger is shown in Fig. 2.17. The ZeroBias is the looser trigger while the HT450 is the tighter. In the low mass region the slopes are very different because of trigger selection. The L1HT trigger for 400 GeV < m_{jj} < 600 GeV and the HT450 triggers for m_{jj} > 600 GeV were chosen to define the m_{jj} regions where the different triggers are fully efficient.

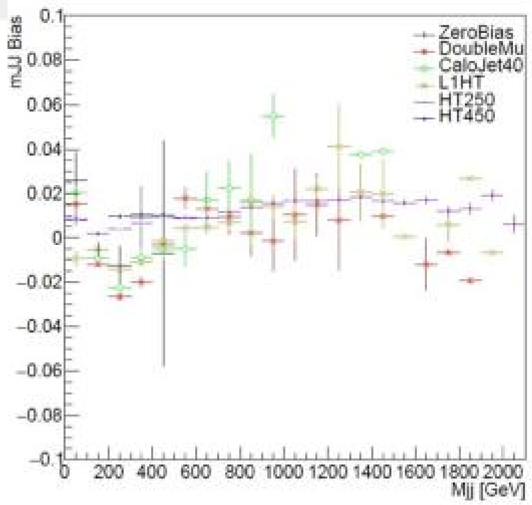

Figure 2.17. m_{jj} bias as a function of m_{jj} for different triggers

If the bias caused by the trigger can prevented, then the only difference between m_{jj}(HLT) and m_{jj}(RECO) would depend on different jet reconstruction.

Thus, the distribution of the m_{jj} bias can be fitted to extract invariant mass corrections. The function which was used for the fit is polynomial logarithmic function with four parameters and is given by Eq. 2.23;

$$f(m_{jj}) = p_0 log^3(m_{jj}) + p_1 log^2(m_{jj}) + p_2 log(m_{jj}) + p_3 \tag{2.23}$$

The m_{jj} bias as a function of the invariant mass is shown in Fig. 2.18 with fit result. A bias up to 2% is observed and Table 2.10 gives the list of the values of the fit parameters.

The closure test was performed in the other half of the events that were applied on top of the others following the implementation of this new level of correction.

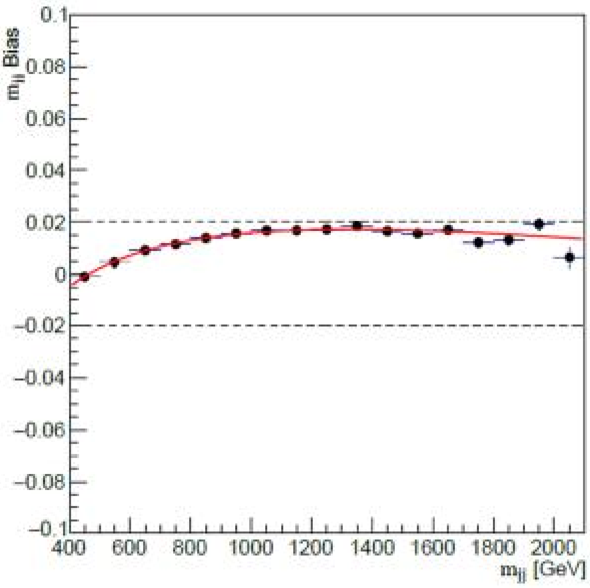

Figure 2.18. Distribution of the invariant mass bias in function of the invariant mass (The polynomial logarithmic fit is shown in red line)

Table 2.10. Parameter values obtained from fit

Parameter	Fit value
p_0	$-0.00119706 \pm 3.68652e^{-06}$
p_1	$0.00910685 \pm 3.01338e^{-05}$
p_2	$0.0547697 \pm 0.000199688$
p_3	-0.402532 ± 0.00110099
$\mathcal{X}^2/NDF$	20.2523/13

In Fig. 2.19. m_{jj} bias as a function of the invariant mass after the residual m_{jj} corrections is shown. As it can be seen from the figure the residual bias is at level of 0.5%.

2.2.5. Data Quality Studies

The QCD multijet production is the main background in this study. Detailed data quality checks were performed for the events that pass the main selection criteria. These checks contain comparation of the data with MC for investigation of the stability of reconstructed quantities as a function of the number of reconstructed vertices and a time.

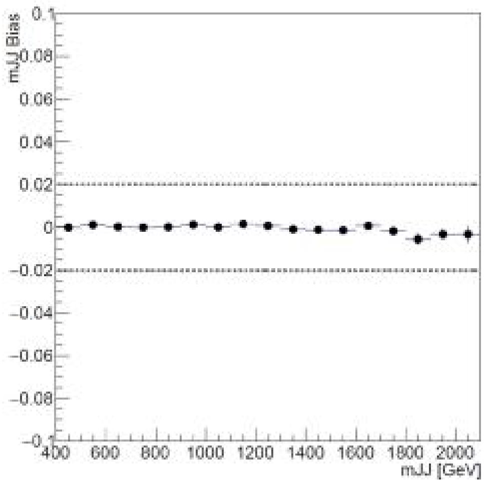

Figure 2.19. m_{jj} bias as a function of the invariant mass after the residual m_{jj} corrections

2.2.5.1. Comparisons between Data and Simulated Events

The QCD events distributions obtained from the simulation were not used to extract the physics results in the analysis, but were used for the comparison and checking the data quality. Jet related quantities were compared using data and MC to check the quality of data, robustness of event, jet selection against beam, detector related noise, detector pathologies and reconstruction catastrophic failures, etc. The event-related distributions can be examined as below:

- The ratio of the missing transverse energy in the event to the total transverse energy, $\frac{E_T^{miss}}{\sum E_T}$;
- The angle between the two leading jets in the transverse plane, $\Delta\Phi = \Phi_1 - \Phi_2$;
- The angle between the colliding and the scattered partons at the center-of-mass frame, $cos(\theta^*) = tanh\left(\frac{\Delta\eta_{jj}}{2}\right) = tanh\left(\frac{y_1-y_2}{2}\right)$;
- The absolute difference in pseudorapidity, $\Delta\eta = |\eta_1 - \eta_2|$, between the two leading wide-jets.

The first variable, $\frac{E_T^{miss}}{\sum E_T}$, is sensitive to the noise that generates a distinct energy imbalance relative to the total energy in the event, and thus fakes the missing energy. For this reason, events related to presence of noise will tend to fill higher values than expected. The second variable, $\Delta\Phi = \Phi_1 - \Phi_2$, is also sensitive to noise and particularly sensitives to noise clustered into jets. Fake jets are distort the event distribution and it takes us away from events populated regions where $\Delta\Phi = \pi$. The third variable, $cos(\theta^*)$, which shows how forward the dijet production, is represents the scattering angle of the final partons in the center-of-mass frame and any deviation from the expectation would be an indication of data pathologies and is also sensitive to noise. Finally, fourth variable, the absolute difference in pseudorapidity between the two leading wide-jets has also been examined.

The comparisons between data and simulated events for the variables discussed above, illustrated in Fig. 2.20 and Fig. 2.21. The trigger is not fully efficient at 565 GeV dijet mass and therefore the difference between the data and MC occurs around $\Delta\eta$ =1.1 and 1.3. Essentially, this inefficiency in the trigger is due to the highest $\Delta\eta$ events corresponding to the lowest jet H_T for a fixed dijet mass.

Furthermore, after the application of all the selection criteria, the agreement between data and simulated events for jet kinematic quantities η and Φ can be examined, as shown in Fig. 2.22. The difference in the jet energy response as a function of η at HLT and RECO leads to difference between data and MC. This is accounted for on average for the whole sample in our jet energy corrections which are as a function of wide jet dijet mass only.

It is clear from the jet and other event related distributions after applying event and jet selection criteria that the signal sample is clean, there is no pathology, and there are no signs of noise.

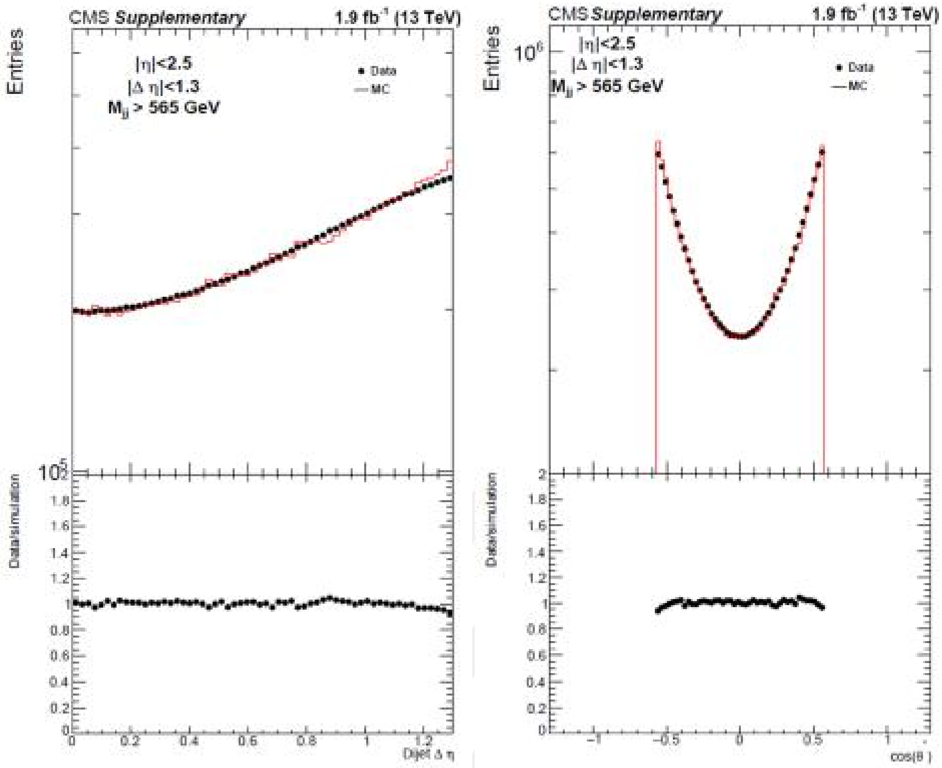

Figure 2.20. Left: The $\Delta\eta$ (difference in pseudorapidity) between the two final wide jets and Right: the $cos(\theta^{*})$ (q is the angle between beam axis and the dijet system) at the center-of-mass frame of the event for data (points) and simulated (continuous histogram) events, along with their ratios (bottom plots) after all selection criteria

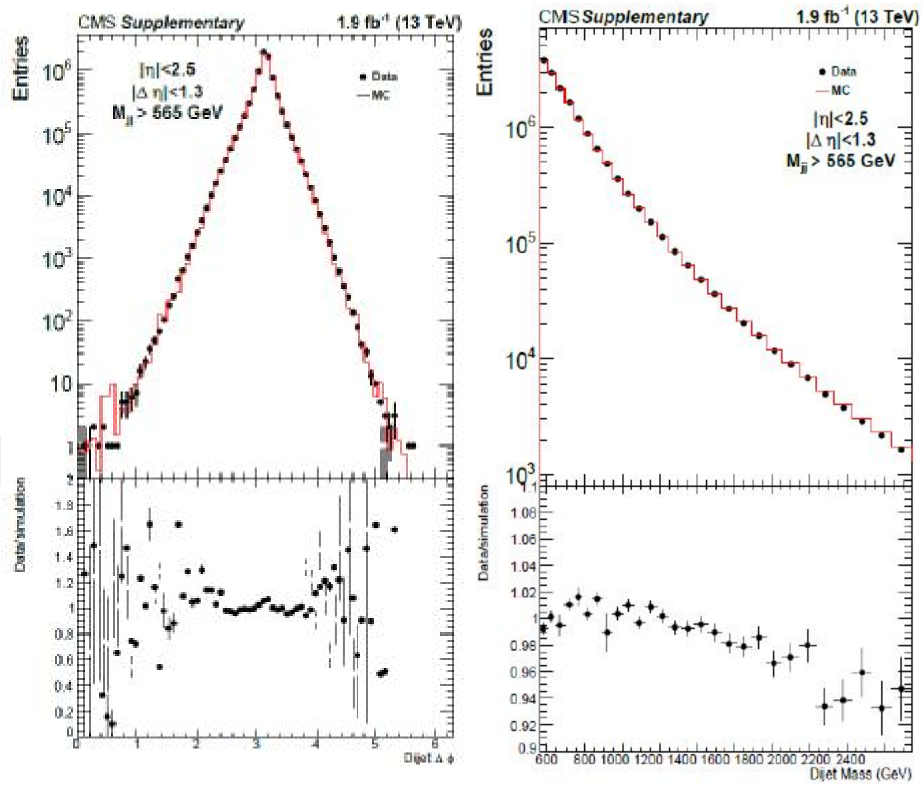

Figure 2.21. Left: The angle between the two final wide-jets of the event, $\Delta\Phi$, Right: The dijet mass of the two final wide-jets of the event, after all applied selection criteria, for data (points) and simulated (continuous histogram) events, along with their ratios (bottom plots)

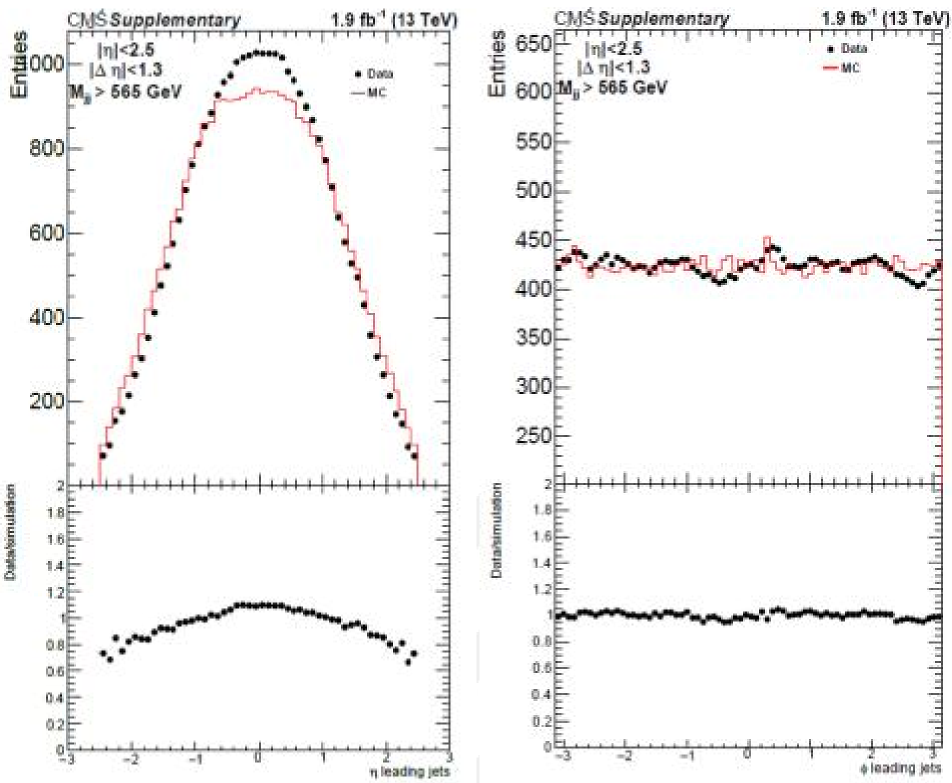

Figure 2.22. The η (left), and Φ (right) of the two leading wide-jets after all applied selection criteria, for data (points) and simulated (continuous histogram) events, along with their ratios (bottom plots)

2.2.5.2. Time and Pile-up Effects

This study examins the behavior of basic data quantities as a function of time and pile-up and is conducted to ensure the quality of the recorded and selected data. In order to quantify the stability of event and jet related characteristics, it has been examined as a function of both run number and the primary vertices in the event.

In Fig. 2.23, the dijet mass, $cos(\theta^*) = tanh\left(\frac{\Delta\eta_{jj}}{2}\right) = tanh\left(\frac{y_1 - y_2}{2}\right)$ and $\Delta\Phi = \Phi_1 - \Phi_2$ are examined as a function of time for stability. Event related quantities are stable as a function of time, as indicated by the absence of any significant slope in the distributions.

Fig. 2.24 and Fig. 2.25 show the jet kinematic and the jet energy fractions distributions as a function of time. Likewise, the absence of any significant slopes indicates that the jet-related quantities are stable as a function of time.

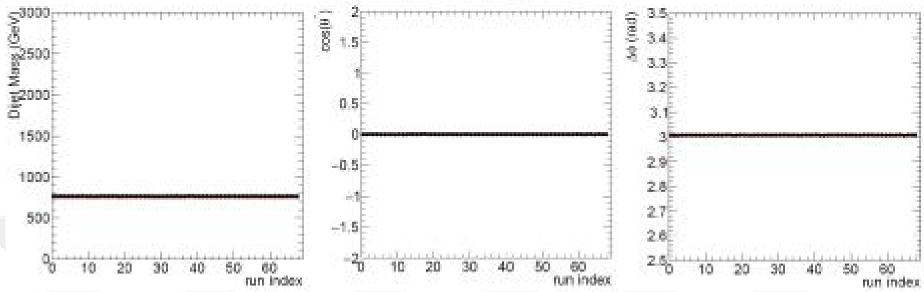

Figure 2.23. The dijet mass (left), $cos(\theta^{*})$ (middle) and $\Delta\Phi$ (right) distributions after all applied selection criteria as a function of time

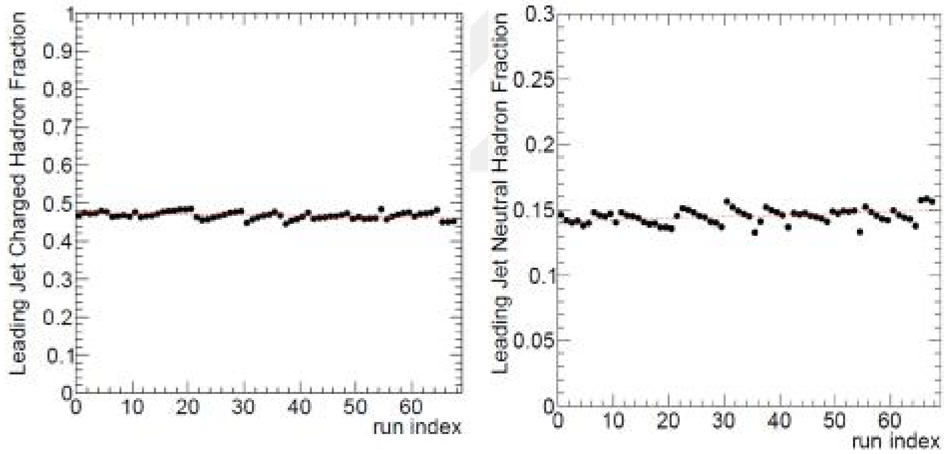

Figure 2.24. The jet charged (left) and neutral hadron (right) energy fractions after all applied selection criteria as a function of time

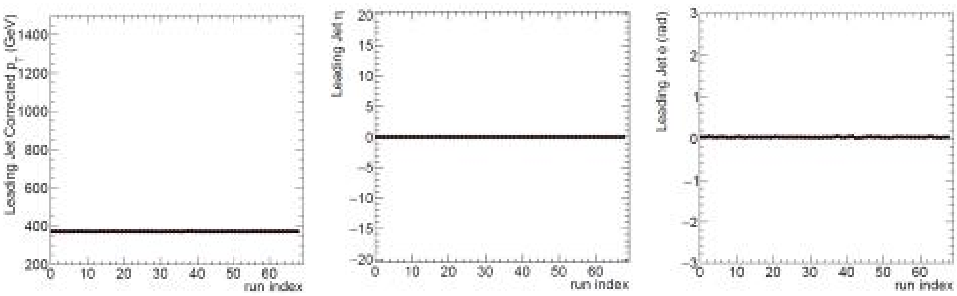

Figure 2.25. The jet p_T (left), η (middle), and Φ (right) energy fractions after all applied selection criteria as a function of time

2.2.5.3. Cross Section Stability

After all selections for this analysis the stability of the dijet cross section as a function of time is given in Fig. 2.26.

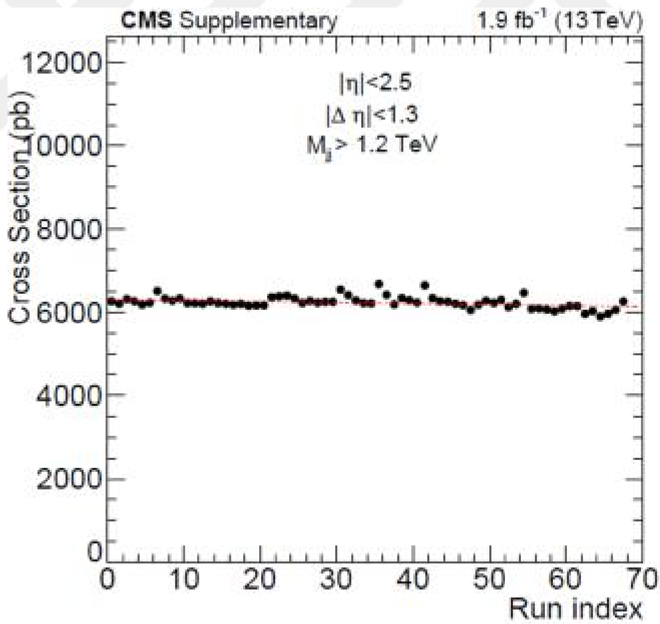

Figure 2.26. Stability of the dijet cross section as a function of time, after all applied selection criteria

3. RESULTS AND DISCUSSIONS

3.1. Search for Dijet Resonances

Searching dijet resonances will be discussed in this section, the likelihood fit method used to test the signal hypotheses for the observed dijet mass spectrum and estimate the smooth background distribution.

3.1.1. Signal and Background Model

The signal resonance shape depends on the type of parton pairs (gluon-gluon, quark-quark, quark-gluon) in the resonance decay. Since we only consider the narrow resonances, where the natural resonance width is much smaller than the experimental dijet mass resolution, the natural width is not affecting the resonance shapes. For three types of decay modes ($gg \to G \to gg$, $qq \to G \to qq$ and $qg \to q^* \to qg$) 11 mass points are produced: 500 GeV, 750 GeV, and 1 TeV to 9 TeV (by 1 TeV intervals). Further details about the samples have been given in section 2.2.2.1. Some of the resonance shapes are illustrated in the Fig. 3.1 and Fig. 3.2.

In order to generate 11 mass point samples, the shape interpolation method is used. This method is the same with the method used for the high-mass analysis. Detailed information about this method can be found at (CMS AN, 2015).

Because of the differences between gluons and quarks, resonance shapes differ according partons in the final states (i.e gg, qq or qg). It is observed that gluons emit more radiation than quarks, therefore the resonance widths increases with the number of gluons in the final state. The low-mass tail of the resonance shape is due to the effect of PDF and the Final State Radiation (FSR) having higher parton luminosity at low mass than at high mass. The high mass tail is smaller and originates from Initial State Radiation (ISR). This means that the low mass tail in the resonance shape originates predominantly from FSR while the high mass tail originates from ISR.

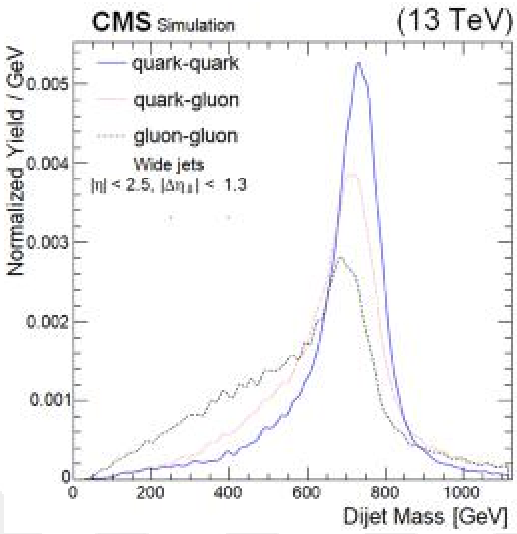

Figure 3.1. Dijet mass shapes for the $gg \rightarrow G \rightarrow gg$, $qq \rightarrow G \rightarrow qq$, $qg \rightarrow q^{*} \rightarrow qg$ resonance models for 750 GeV mass, reconstructed with wide jets (The integral of the shapes has been normalized to unity)

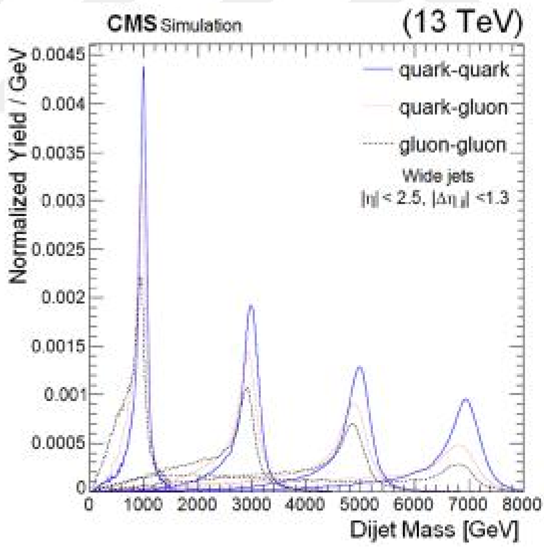

Figure 3.2. Dijet mass shapes for different high mass points for the $gg \rightarrow G \rightarrow gg$, $qq \rightarrow G \rightarrow qq$, $qg \rightarrow q^{*} \rightarrow qg$ models reconstructed with wide jets (The integral of the shapes has been normalized to unity)

Since the CMS detectors have lower response to gluon jets than quark jets, the peak value of the resonance dijet mass decreases with the number of the gluons in the final state. Thus, the gluon-gluon resonance shapes are wider and shifted to lower dijet mass region. An interpolation technique based on vertical interpolation is used to generate the mass points in the intermediate masses (with 100 GeV steps). As a first step, a new parameter, denoted as X, is introduced as X=M_{jj} / M_{Res}, where M_{jj} is dijet mass and M_{Res} is resonance mass. The next step is to generate a new X distribution with any resonance mass. It is generated using neighboring existing MC samples. For example, how to generate the X distribution of resonances with a mass of 4.5 TeV is explained in Eq. 3.1:

$$Prob_{4.5TeV}(x) = Prob_{4\mathrm{TeV}}(x) + [Prob_{5\mathrm{TeV}}(x) - Prob_{4\mathrm{TeV}}(x)].\frac{4.5-4}{5-4} \qquad (3.1)$$

The 4 TeV and 5 TeV MC samples are used as input in this method since they are the neighboring resonance mass points of 4.5 TeV. The generalized formula can be given as:

$$Prob_{M}(x) = Prob_{M1}(x) + [Prob_{M2}(x) - Prob_{M1}(x)].\frac{M-M_1}{M_2-M_1} \qquad (3.2)$$

where M is the desired resonance mass point to be produced and M_1 and M_2 are the neighbor existing MC mass points of M.

In Fig. 3.3 the comparations of the signal shapes for wide jets reconstructed from the AK4 jets, from generator jets and from partons are given. Because of assuming the relative half-width of the model ((Γ/2)/M) is small compared to the dijet mass resolution, they are approximately valid for any resonance model involving these pairs of partons. The integral of all distributions has been normalized to unity and the parton mass distributions were then scaled down by a factor.

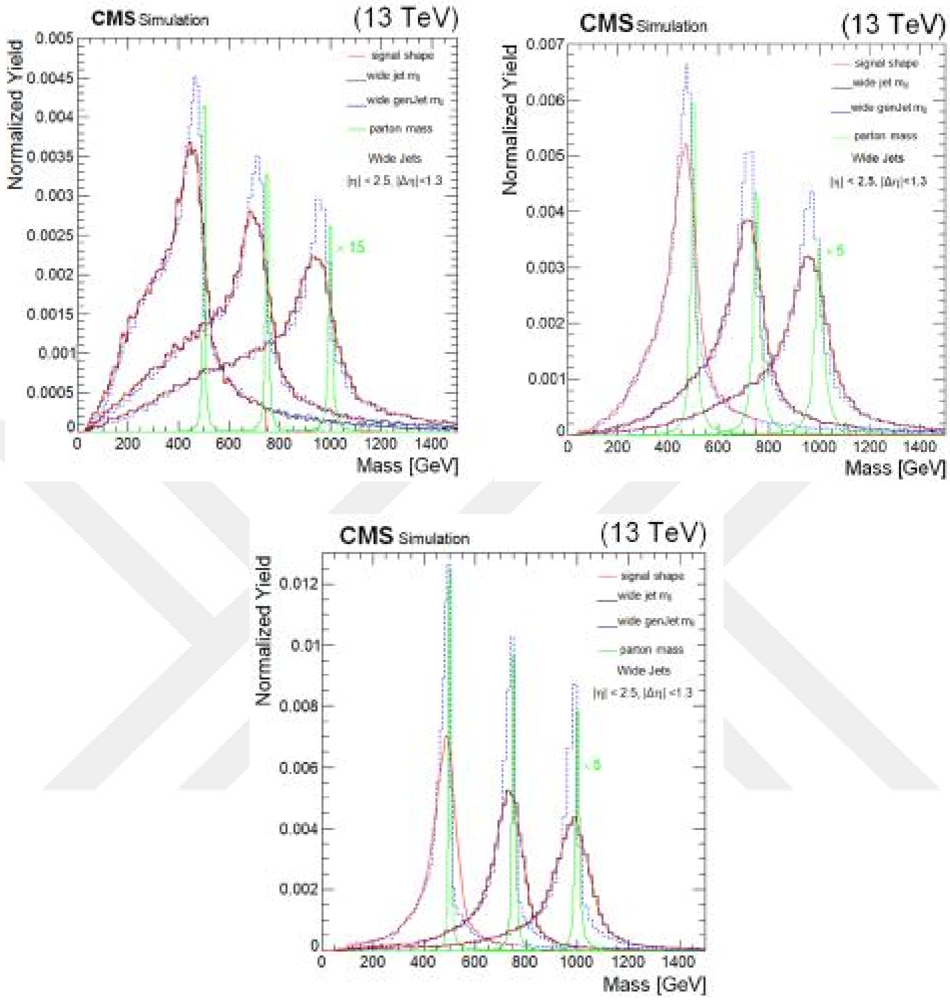

Figure 3.3. Comparison of signal shapes to mass distributions from the wide jets produced from wide generator jets, and partons for gg→G→gg (top left), qg→q*→qg (top right), and qq→G→qq (bottom)

The background estimation which was not based on the MC simulation for dijet analysis was obtained directly from the data. The fit technique was used for this estimation and tested using QCD samples. After fixing the method it is applied to the data. The fit function is given in Eq. 3.3 (where $x = m_{jj}^{wide}/\sqrt{s}$ and m_{jj}^{wide} is measured in GeV and $\sqrt{s}$ = 13 TeV) and has 4-parameters. It is also used in previous dijet searches and details can be found in (Khachatryan et al., 2010, 2013 a, b and 2015).

$$\frac{d\sigma}{dm_{jj}} = \frac{p_{0(1-x)^{p_1}}}{x^{p_2+p_3\ln(x)}} \tag{3.3}$$

The fit to the data for obtaining the background estimate is done by maximizing the likelihood function. The details are given in the next section.

3.1.2. Dijet Mass and Fit

Dijet mass spectrum was compared to the benchmark signal of x → gg with cross-section of 15 pb. This spectrum σ_{dijet}/dM_{jj} fitted with a smooth background function. The signal cross section σ is set to zero in Eq. 3.5 and the four free parameters (p_0, p_1, p_2, p_3) of smooth fit function (in Eq. 3.3) are varied in order to maximize the likelihood.

In the Fig. 3.4, although the mass bin ranges are shown with a horizontal bar, the **x**-axis errors are set to zero to fit the graph. Also, the fit shown as solid red line in the figure is done in the range of 565–2037 GeV which accepted prior to unblinding the data in the region 649–838 GeV. The lower mass limit is driven by the need to have at least two mass bins in the left sideband outside of the blinded region. The higher mass limit depends on the range over which we have sufficient scouting-monitoring data to provide a robust jet energy calibration of HLT data according to RECO data. We also show the fit function, which is extrapolated over the full range of data at 453–6328 GeV, with dotted red line to demonstrate the good stability of the fit. Also, blue dashed line shows the X → gg benchmark signal.

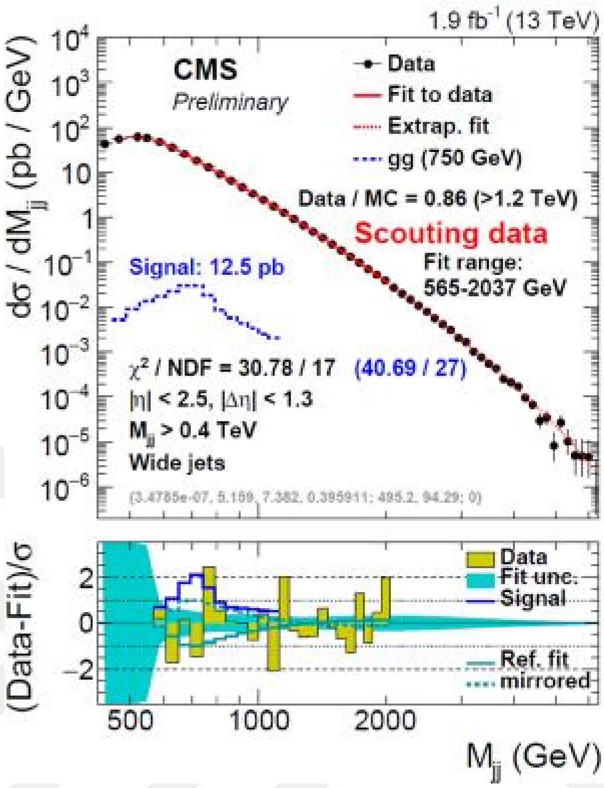

Figure 3.4. Dijet mass cross section

In order to demonstration purposes, the signal histogram is multiplied by the measured trigger efficiency, so that the relative differential cross-section can be directly compared with the data in the turn-on region. The signal cross section of the benchmark $X \rightarrow gg$ is approximately three orders of magnitude lower than data and spans over several mass bins, each of which is roughly the width of the dijet detector mass resolution.

The lower pad in Fig. 3.4 illustrates the fit residuals (Data- fit)/σ as a filled yellow histogram. The $\mathcal{X}^2$ of the residuals, together with the global $\mathcal{X}^2$ from the simultaneous fit are shown in the top pad in black and in blue, respectively. The 30.78/17 $\mathcal{X}^2$value of the fit is on the slightly higher side, but the residuals is randomly scattered without an obvious modulating structure. Before unblinding, a high $\mathcal{X}^2$ was observed and it was concluded that neighboring - 2σ/+2σ structures contributed greatly at 1.1 TeV and 2.1 TeV (only the upper fluctuation is observed for M_{jj} < 2037 GeV). However, these bins contribute about 12 points to the $\mathcal{X}^2$ or 9 of that points are above the normal expectation. When this 9 points are excluded it raise the naive $\mathcal{X}^2$ probability to about 20%: TMath::Prob(30.87 - 9.17)=0.193. Post-unblinding, the largest excess of 2.5 σ is observed at slightly above 750 GeV. This case, a bit higher in mass than the expected peak from our benchmark X → gg signal of σ_{gg}=15 pb, shown in solid blue line for $\sigma_{\text{gg}}/\ \sigma$. To exclude also this bin, the probability of naive $\mathcal{X}^2$ increases to about 50%:TMath::Prob(30.87- 14.25,17)=0.487. However, it will be used as toys for more detailed $\mathcal{X}^2$ probability studies.

In Fig. 3.4 the statistical uncertainty of the fit $\sigma_{\text{fit}}\ /\ \sigma$ is shown for comparison as a cyan band which is calculated using the Minuit fit covariance matrix (CMS AN, 2016).

In proportion to the statistical uncertainty, the low mass extrapolation very quickly diverges outside the range of data used in the fit, while the high mass extrapolation is strongly constrained by the fit. However, this is basically the result of the fact that the statistical uncertainty of the data is very small at low mass. In absolute terms, as in the figure, also the low mass extrapolation is stable in the top pad. The statistical uncertainty of the background fit, to the majority of the fitted range, is either 0.5σ or less. Also, in the figure the fit prior to unblinding, $(Fit_{blind} - Fit)/\sigma$, is shown as a solid cyan line for comparison, labeled "Ref. fit". Although it was consistent within the larger pre-unblinding fit uncertainties, the pre-unblinding fit differs by around $2\sigma_{\text{fit}}$ from the post-unblinding fit in the signal region. And also we show its reflection $(Fit - Fit_{blind})/\sigma$ with dashed cyan line, to compare better the difference in background fits with the benchmark signal shape. This shows that the change in the background fit has a similar shape but smaller size than the benchmark signal.

The fit function for background-only hypothesis describes the data well and any significant excess is not observed in the dijet mass spectrum. In other word, dijet resonance doesn't appear in the dijet mass spectrum as a bump.

As shown in Fig. 3.5 the background fit results are summarized again in the PAS plot. This figure looks same as Fig. 3.4, but rejects some information (Top pad: Data/MC numbers, "Scouting data" label, fit range, signal cross section label, M_{jj} > 0.4 TeV label, gray parameter numbers; bottom pad: fit uncertainty, reference fit and mirrored fit).

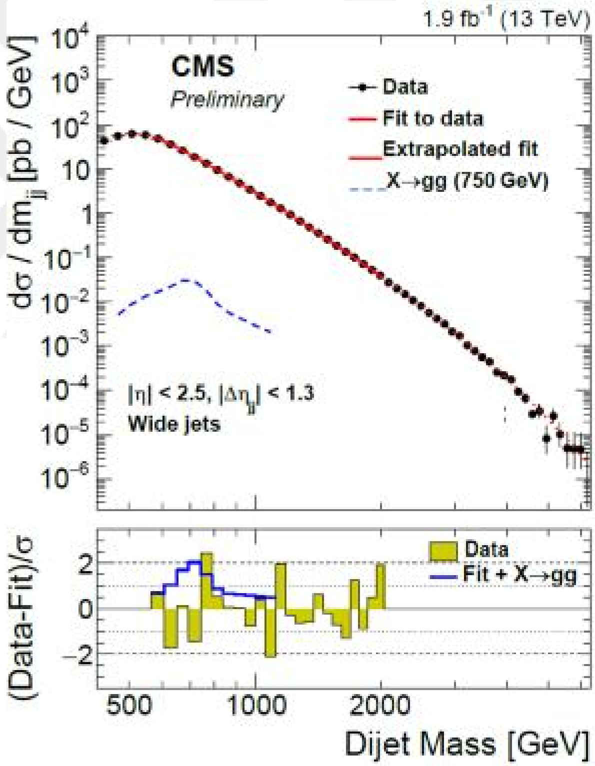

Figure 3.5. Dijet mass cross section plot for the PAS

3.1.3. Results

3.1.3.1. Limit Setting Procedure

The Bayesian formalism was used with flat prior for the cross section when upper limits were set on dijet resonance cross section. The twiki page has instructions to run the code[3].

The binned likelihood, L, as a function of a constant α can be written as:

$$L = \prod_i \frac{\mu_i^{n_i} e^{-\mu_i}}{n_i!} \tag{3.4}$$

where

$$\mu_i = \alpha N_i(S) + N_i(B) \tag{3.5}$$

n_i – measured number of events in the ith dijet mass bin, N_i(S) - number of events from the signal in the ith dijet mass bin, α - constant scaling the signal amplitude, and N_i(B) - number of expected background events in the ith dijet mass bin. This limit code is based on the ROOT TMinuit class. In order to achieve proper coverage for the credibility intervals in the presence of a signal that is not yet strong enough to be evinced, the data are fit to the background function plus a signal line shape with the signal cross section treated as a free parameter. The bin width is approximately the dijet mass resolution, and gradually increases as a function of mass accordingly with the dijet mass resolution. Due to the large number of events present in the mass distribution, this approach (instead of unbinned likelihood fit) is chosen to reduce CPU timing. In each bin, number of expected background events is computed by integrating the function over the bin width. The resulting fit function is used as the background hypothesis and set to zero with signal cross section. It provides the expected number of background

[3] https://twiki.cern.ch/twiki/bin/view/CMS/DijetLimitCode

events N_i (B) in the ith dijet mass bin. The number of signal events N_i(S) in the ith dijet mass bin, comes from the signal histogram templates. The signal range is chosen from 0 to 1.5 TeV. M_{Res} is the nominal resonance mass and is an interval that contains nearly all the resonance line shape. We assume same flat prior in α as in the resonance cross section. With the above assumption the likelihood normalized to unity is equivalent to a posterior probability density, and can be used to set limits.

For resonances with mass from 0.7 TeV to 1.5 TeV in 50 GeV steps we calculate a posterior probability density as a function of signal cross section. The 95% CL upper limit σ_{95} calculated with the posterior probability density PPOST defined as:

$$\frac{\int_0^{\sigma_{95}} P_{POST}(\sigma)d\sigma}{\int_0^{\infty} P_{POST}(\sigma)d\sigma} = 0.95 \tag{3.6}$$

The methodology to determine the expected limits in absence of signal as follows; for each signal hypothesis, background shapes from a signal + background fit to the data (i.e. for each considered mass point) are determined. The resulting fit function is used as the background hypothesis and set to zero with signal cross section. From the background function, the number of events expected in each bin is used to create pseudo-data that include only the background component. All other steps of limit setting procedure are identical to the case of observed limit. For each mass point, we generate 1000 background samples and produce a distribution of the upper limits on cross section. At a given mass point, the expected limit is derived from the median of each distribution. By using four quantiles corresponding to 1σ down and up (cumulative probabilities equal to 0.159 and 0.841) and 2σ down and up (cumulative probabilities equal to 0.021 and 0.979), the expected limit bands are obtained.

By introducing nuisance parameters in the likelihood function, systematic uncertainties are incorporated in the limit calculation and marginalizing the posterior likelihood over the nuisance parameters using their priors. Using Markov chain MC integration implemented in the Bayesian Analysis Toolkit (Caldwell, 2009), the marginalization over the nuisance parameters is performed. Additional information on the sources of systematic uncertainties considered in this analysis and their treatments can be found in section 3.1.3.3.

3.1.3.2. Significance of Local Excesses in Data

A method used to estimate the significance of local excesses in data is presented in this section. The one described in the reference (Guichardant et al., 2012) is very similar to the general approach. Following method is used with a likelihood-based significance estimator defined as:

$$Sig = sgn(S)\sqrt{-2ln\left(\frac{L_B}{L_{S+B}}\right)} \tag{3.7}$$

where, L_B is the maximum likelihoods from the background-only, and L_{S+B} is the signal + background (S+B) fits to the data. The likelihood function is same as defined in Eq. 3.4. Since the S+B fit allows the signal strength to be negative, the significance estimator is signed accordingly. However, the significance values will only be reported for upward fluctuations (positive signal strengths). The technical difference with respect to (Guichardant et al., 2012) is the significance calculation implemented in the limit setting code. Beside that the same background parametrization, pseudo-experiment generation procedure, signal shapes, likelihood function, etc. was used. It should also be noted that the results presented in this section do not include systematic uncertainties.

The results for significance scan as a function of the resonance mass for the three resonance type hypotheses (qq, qg, and gg) are shown in Fig. 3.6. At a mass of 0.8 TeV, for the gg resonance hypothesis the most significant excess (~2σ) occurs. It can be emphasized that the upward fluctuation trend in the significance plots closely follows a similar trend in the limit plots in Fig. 3.8.

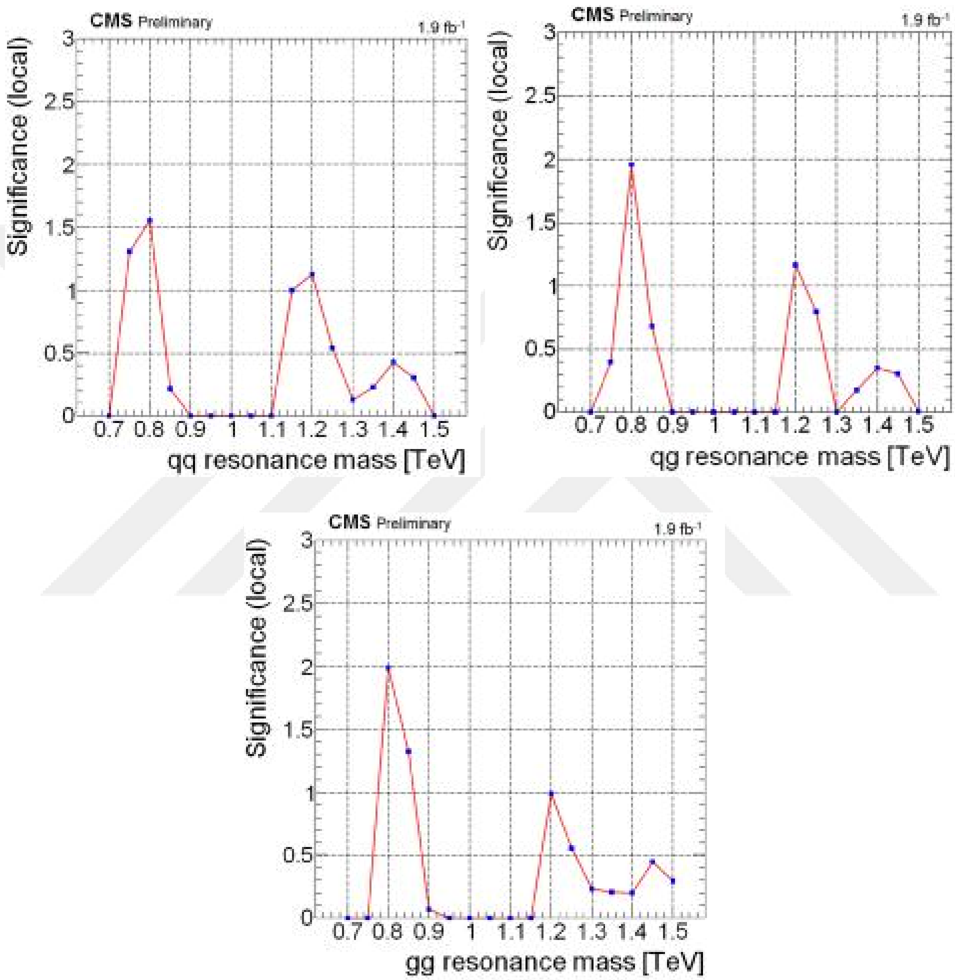

Figure 3.6. Significance scan as a function of the resonance mass for qq (top left), qg (top right) and gg (bottom) resonances

3.1.3.3. Systematic Uncertainties

Systematic uncertainties sources relevant for this study are as folows:

- Jet Energy Scale (JES)
- Jet Energy Resolution (JER)
- Background Parametrization
- Trigger Turn-on
- Luminosity

The background shape is derived from the data itself for this study. Because of that only uncertainties on the JES, JER, and luminosity are considered for the resonance signal. In the limit calculation, the above-mentioned systematic uncertainties are included as nuisance parameters with log-normal priors (details are given in Gouzevitch, 2012). Different method applied for background shape and trigger turn-on uncertainties as described below.

3.1.3.3.(1). Jet Energy Scale

As the background component comes directly from the data via the S+B fit, the JES uncertainty is only considered for the simulation of resonance signals and therefore JES is same as data. The background shape is well defined and derived from data, hence shifting of the resonance dijet mass to lower values by the jet energy scale uncertainty gives more SM background from QCD in a window around the resonance mass, and therefore an increase in upper limit on the resonance cross section happens.

The uncertainties from Summer15_25nsV7 which is recommended by the JetMET group are used. These uncertainties propagate almost linearly to the dijet mass on the jet p_T.

3.1.3.3.(2). Jet Energy Resolution

The uncertainty on the JER translates into 10% of uncertainty on the resolution of the dijet mass (The CMS Collaboration, 2011) and used for Run 1 searches recommended by the JetMET group. By changing the width of the resonance shape by ±10%, this uncertainty is propagated to the search, results in slight stretching or shrinking of the resonance shape.

3.1.3.3.(3). Background Parametrization

The background parameters, by following the Bayesian approach, should be integrated over the entire space of parameters values to extract the posterior distribution of the signal cross section. Also, these parameters are all considered as nuisance parameters. Technically, to identify a reasonable starting point for the parameter values, firstly S+B fit to the data is performed. Covariance matrix of the background parameters have diagonal symmetry and along the eigen-vectors of this matrix, the variations of the original parameters are introduced as nuisance parameters, i.e., nuisance parameters are the set of de-correlated parameters defined as linear combination of the original parameters. The uncertainty in the background is finally incorporated through marginalization, i.e., by using flat priors we integrates the likelihood over the background parameters. Such integration is performed for each background nuisance parameters in a range around the best-fit values, instead log-normal priors and $\pm1\sigma$ integration range.

CMS Statistics Committee suggested a procedure after the ICHEP2012 analysis. A detailed description on this procedure is available in the talk given at CMS Statistics Committee meeting[4].

[4]https://indico.cern.ch/event/225689/contributions/1532166/attachments/371140/516452/Bump hunting 20130110.pdf

3.1.3.3.(4). Trigger Turn-on

While the previous dijet resonance searches performed in a portion of the dijet mass spectrum with fully efficient triggers at CMS did not take into account the trigger turns-on, it is taken into account in this analysis. But this causes an additional source of systematic uncertainty. To handle this extra systematic uncertainty a covariance matrix obtained from the trigger turn-on fit and these decorrelated parameters treated as nuisance parameters (CMS AN, 2016).

3.1.3.3.(5). Luminosity

The beam-beam scans utilizing the methods referred in (CMS Collaboration, 2013b) being used to estimate the luminosity and its uncertainty. An uncertainty of 2.7% is set for the integrated luminosity, and it is propagated to the normalization of the signal.

3.1.3.4. Limits

Regarding the background prediction, no significant excess is observed in the data. For the gg resonance hypothesis, the largest observed excess in data occurs at a mass of 0.8 TeV and has a local significance of ~2σ (see 3.1.3.2. for more details). On the cross section of new resonances, we proceed to set upper limits.

There is an observed model-independent upper limit at the 95% Confidence Level (CL) on $\sigma\ B\ A$ (where σ is cross section, B is the branching fraction, and A is the acceptance) for the kinematic requirements described in Section 2. The results are shown in Fig. 3.7 as well as in Table 3.1 for narrow qq, qg, and gg resonances. For the mass interval starting from 0.7 to 1.5 TeV in RS graviton model where 60% (40%) cross section contributed from the sub-proceses with quarks (gluons) only, the cross section limits are shown in Fig. 3.7. The cross section limits are obtained as a weighted average of the upper limits in the quark - quark and gluon - gluon final states.

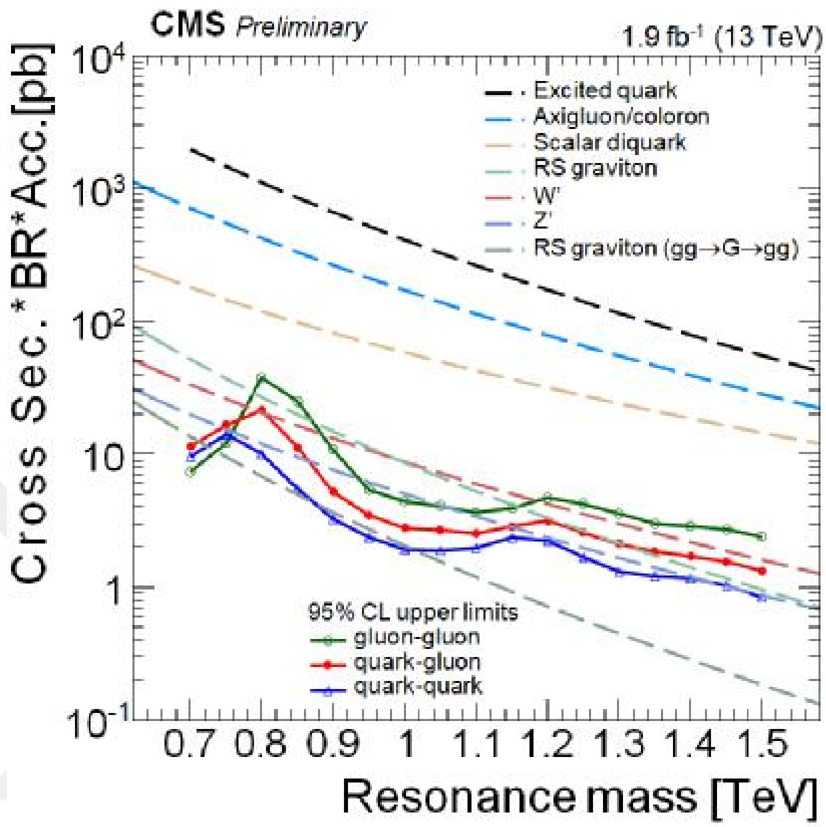

Figure 3.7. The observed 95% CL upper limits on $\sigma\ B\ A$ for dijet resonances of the gluon-gluon, quark-gluon, and quark-quark, compared to theoretical predictions for string resonances, scalar diquarks, excited quarks, axigluons, colorons, color octet scalars S8, new gauge bosons W' and Z' and RS gravitons

In order to determine mass limits on new particles without any detector simulation, the observed upper limits can be compared to parton level predictions of $\sigma\ B\ A$. The results presented are obtained using CTEQ6L1 parton distributions (Pumplin et al., 2002).

As described in Section 3.1.3.1. S+B fits to data are used to obtain background shapes which helps in generating the expected limits on cross section which are estimated with pseudo-experiments. As shown in Fig. 3.8, the both observed limits and model predictions are compared to the expected limits and their 1 and 2σ standard deviations for qq, qg, and gg resonances.

Appendix C includes the discussion on the impact of the systematic uncertainties on the limits.

The theory curve lies above the observed upper limit for the appropriate final state and with due effect new particles are excluded at the 95% CL in mass regions. We exclude at 95% CL models of RS gravitons for mass range 700 and 1200 GeV and scalar diquarks, excited quarks, colorons, axigluons, W' and Z' bosons for masses range 700 and 1500 GeV.

Table 3.1. Observed upper limits at the 95% CL on $\sigma\, B\, A$ for resonances decaying to qq, qg, and gg final states as a function of the resonance mass

Mass (TeV)	**Upper limit (pb)**		
	qq	**qg**	**gg**
0.70	9.655	1.148	7.432
0.75	1.415	1.655	1.216
0.80	1.014	2.147	3.794
0.85	5.537	1.136	2.505
0.90	3.247	5.217	1.081
0.95	2.376	3.469	5.367
1.00	1.927	2.787	4.430
1.05	1.892	2.687	4.067
1.10	1.974	2.540	3.651
1.15	2.380	2.867	3.929
1.20	2.244	3.177	4.713
1.25	1.695	2.563	4.234
1.30	1.315	2.107	3.583
1.35	1.209	1.862	2.999
1.40	1.169	1.714	2.863
1.45	1.034	1.561	2.733
1.50	8.466	1.339	2.397

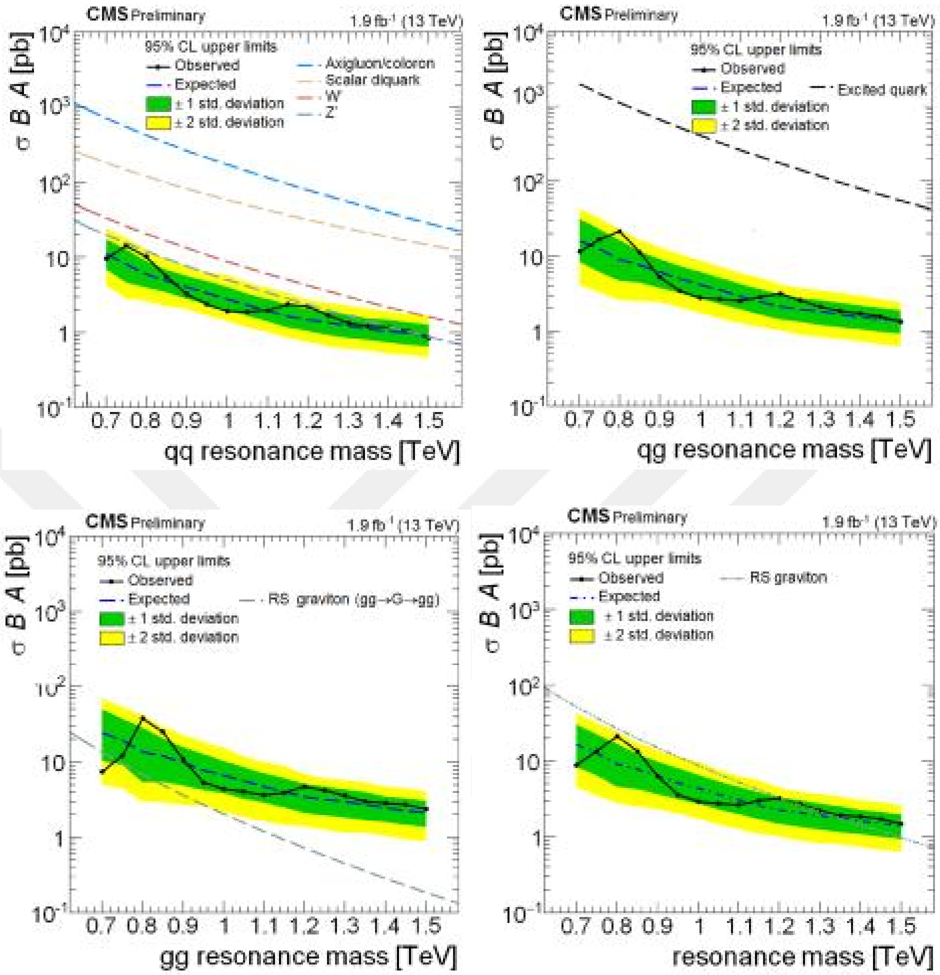

Figure 3.8. The observed 95% CL upper limits on σ B A for resonances decaying into quark quark (top left), quark gluon (top right), and gluon gluon (bottom left) final states and for RS Gravitons (bottom right) (The limits are shown as points connected by solid curves. The expected limits (dot-dashed blue curves) and their 1 and 2σ standard deviations (shaded bands), predicted cross sections for various resonance models are also shown)

4. CONCLUSIONS

For dijet resonance in qq and gg final states, upper limits on cross section were presented in section 3.1.3.4. $\sigma\ B\ A$ values greater than 12.2 pb for a g-g resonance, and greater than 14.2 pb for a q-q resonance were exluded at 95% CL when a resonance mass of 750 GeV is considered. By using a particular model cross section, these limits could be compared to the Run 1 limits (CMS Collaboration, 2016) at $\sqrt{s}$ = 8 TeV. Let consider the Randall-Sundrum graviton sub-process gg → G → gg. This sub-process has a $\sigma\, A$ of 9.6 pb at $\sqrt{s}$ = 13 TeV and it is not excluded by our Run 2 limit of 12.2 pb. But gg → G → gg has a $\sigma\, A$ of 1.9 pb at $\sqrt{s}$ = 8 TeV and it is excluded by the Run 1 upper limit of 1.8 pb. When compared to Run 1, our constraint on the g-g decays of a narrow resonance at 750 GeV is not so stringent. A similar result has been obtained for a narrow 750 GeV resonance that decays into quarks also.

At mass of 750 GeV at diphoton channel, for dijet resonance this search was conducted primarily to establish our observed constraints in Run2, despite the fact that it was expected that our sensitivity would be less than Run 1 based on the parton luminosity ratio alone. Despite of lower sensitivity, it was observed a more significant effect at 750 GeV in Run 2 by both CMS and ATLAS than in Run 1 in the diphoton channel. As clearly shown in Fig 6.8, we found a significance including statistical uncertainties of 1.3 standard deviations in the q-q channel and a negative significance is obtained in the gluon-gluon channel at 750 GeV, while roughly zero significance was observed in both channels in Run 1(Isildak et al., 2015). Although it was not found in Run 2 a significantly larger effect at 750 GeV compered to Run 1 unlike diphotons, this analysis will be a base for analyzing 2016 data.

Using a data sample of pp collisions at $\sqrt{s}$ = 13 TeV, a search for narrow resonances decaying into a pair of jets has been performed. The integrated luminosity is 1.9 fb^{-1} which is collected with the particle flow data scouting technique. The dijet mass spectrum has been measured and no evidence is found for resonans particle production in the analyzed data sample. Generic upper limits are presented on the product $\sigma\ B\ A$ that is applicable to any model of narrow dijet resonance production. We exclude at 95% CL models of colorons, scalar diquarks, axigluons, excited quarks, W' and Z' bosons for masses between 700 and 1500 GeV and RS gravitons for masses between 700 and 1200 GeV. When we consider a resonance mass of 750 GeV, excluding at 95% CL $\sigma\ B\ A$ values comparably greater than 12.2 pb for a g-g resonance, and greater than 14.2 pb for a q-q resonance, where the acceptance is approximately 0.6 for isotropic decays. The constraints on the dijet decays of a narrow resonance compared to those previously presented in Run 1 are not stringent. If we compare the constraints on the dijet decays of a narrow resonance with those previously presented in Run 1 (CMS Collaboration, 2016), then we found that these constraints are not as stringent as they were in Run1.

REFERENCES

Aad, G., et al., 2008, "The ATLAS Experiment at the CERN Large Hadron Collider". Journal of Instrumentation 3, 08, p. S08003.

Aamodt, K., et al., 2008, "The ALICE experiment at the CERN LHC". Journal of Instrumentation 3, 08, p. S08002.

Abdullin, S et al., 2009, CMS ECAL/HCAL Collaboration, "The CMS barrel calorimeter response to particle beams from 2 to 350 GeV/c", The European Physical Journal C - Particles and Fields 60, 359–373.

Anchordoqui, L. A., Goldberg, H., Lüst, D., Nawata, S., Stieberger, S., and Taylor, T. R., 2008, "Dijet signals for low mass strings at the large hadron collider", *Phys. Rev. Lett.*, vol. 101, p. 241803, Dec.

Angelopoulos, V. D., Ellis, J., Kowalski, H., Nanopoulos, D.V., Tracas, N.D., and Zwirner, F. 1986., "198702214.pdf".

Augusto Alves, J. R., A., et al., 2008, "The LHCb Detector at the LHC", Journal of Instrumentation 3, 08, p. S08005.

Azzurri, P., et al., 2010, "Commissioning of TrackJets in pp Collisions at 7 TeV", The CMS Collaboration CMS-PAS-JME-10-006.

Bagger, J., Schmidt, C., and King, S., 1988. "Axigluon Production in Hadronic Collisions", *Physical Review D* 37(5): 1188–96.

Baur, U., 1990, "E Fermi National Accelerator Laboratory", 1991(February).

Bawa, H. S., 2007, "Some Aspects of High ET jets in p-p collisions at LHC", CERN-THESIS-2009-022

Bayatian, G. L., et al., 1997a, CMS Electromagnetic Calorimeter Project Technical Design Report, CERN/LHCC-97-33.

Bayatian, G. L., et al., 1997b, CMS Hadronic Calorimeter Project Technical Design Report, Technical Report 97-31, CERN/LHCC.

Bayatian, G. L., et al., 1997c, CMS Magnet Technical Design Report, CERN/LHCC-97-10

Bayatian, G. L., et al., 2000, CMS TriDAS Project Technical Design Report Volume I: The Trigger Systems, CMS TDR 6.1, CERN/LHCC 2000–38.

Bayatian, G. L., et al., 2005, CMS Computing Technical Design Report 2005-023 CERN/LHCC.

Bayatian, G. L., et al., 2006, CMS Physics, “Tehcnical Design Report, Volume I: Detector Performance and Software”, 2006-001, CMS TDR 8.1, CERN/LHCC.

Baur, U., Hinchliffe, I. and Zeppenfeld, D., 1987, “Excited quark production at hadron colliders”, Int. J. Mod. Phys. A **2** 1285.

Baur, U., Spira, M., and Zerwas, P. M., 1990, “Excited quark and lepton production at hadron colliders”, Phys. Rev. D 42 (1990) 815.

Beringer, J., et al., 2012, “Review of Particle Physics”. Phys. Rev. D. 86, 010001.

Bijnens, J., Eerola, P., Maul, M., Mansson, A., and Sjostrand, T., 2001, “QCD signatures of narrow graviton resonances in hadron colliders”, *Phys. Lett.*, vol. B503, pp. 341–348.

Bruning, O., et al., 2004, LHC Design Report. Vol. I: The LHC Main Ring, 10.5170/CERN-2004-003-V-1.

Cacciari, M., Salam, G. P. and Soyez, G., 2008, “The anti-k_T jet clustering algorithm”, JHEP 0804, 063.

Caldwell, A., Kollar, D., and Kroninger, K., 2009, “BAT: The Bayesian analysis toolkit”, Comput. Phys. Commun. 180, 2197.

Candelas, P., Horowitz, G. T., Strominger, A., and Witten, E., 1985, “Vacuum configurations for superstrings”, *Nuclear Physics B*, vol. 258, pp. 46 – 74.

Chatrchyan, S., et al., 2008a, “The CMS experiment at the CERN LHC”, The CMS Collaboration JINST 3 S08004.

Chatrchyan, S., et al., 2008b, The CERN Large Hadron Collider: Accelerator and Experiments Volume2, The CMS Collabration JINST 3 S08004.

Chatrchyan, S., et al., 2010, CMS Collaboration, “Jet Energy Corrections determination at sqrts = 7TeV”, CMS PAS JME-10/010.

Chatrchyan, S., et al., 2011, “Determination of jet energy calibration and transverse momentum resolution in CMS”, *JINST*, vol. 6, p. P11002.

Chatrchyan, S., et al., 2013a “Search for narrow resonances using the dijet mass spectrum in pp collisions at $\sqrt{s}$ = 8 TeV”, ***Phys. Rev. D***, vol. 87, p. 114015.

Chatrchyan, S., et al., 2013b “Search for narrow resonances and quantum black holes in inclusive and ***b***-tagged dijet mass spectra from pp collisions at $\sqrt{s}$ = 7 TeV”, ***JHEP***, vol. 01, p. 013, 2013.

Chivukula, R. S., Farzinnia, A., Ren, J., and Simmons, E. H., 2013, “Hadron Collider Production of Massive Color-Octet Vector Bosons at Next-to-Leading Order”, Phys.Rev. D87**,** no. 9, 094011.

Chivukula, R. S., Cohen A. G., and Simmons, E. H., 1986, Phys. Lett. B 380, 92.

CMS AN., 2015/063, 2015, “Search for narrow resonances using the dijet mass spectrum in proton-proton collisions at $\sqrt{s}$ = 13 TeV (Phys14 MC analysis)”.

CMS AN., 2016/145, 2016, “Search for dijet resonances from data scouting at $\sqrt{s}$=13 TeV using 1.9 fb^{-1} collected in 2015”.

CMS Collaboration, 2009, “Particle-Flow Event Reconstruction in CMS and Performance for Jets, Taus, and E_T^{miss} ”, CMS PAS PFT-09-001

CMS Collaboration, 2010, “Jets Performances in *pp* Collisions at $\sqrt{s} = 7TeV$”, CMS PAS JME-10-003.

CMS Collaboration, 2012, “Performance of CMS muon reconstruction in pp collisions events at $\sqrt{s} = 7TeV$ ”, CMS-MUO-10-004.

CMS Collaboration, 2013a, CMS Luminosity Based on Pixel Cluster Counting - Summer 2013 Update.

CMS Collaboration, 2013b, "CMS Luminosity Based on Pixel Cluster Counting - Summer 2013 741 Update", CMS Physics Analysis Summary CMS-PAS-LUM-13-001.

CMS Collaboration, 2016, "Search for narrow resonances in dijet final states at sqrt(s)=8 TeV with the novel CMS technique of data scouting".

CMS Physics Analysis Summary CMS-PASLUM-13-001, 2013, URL: http://cdsweb.cern.ch/record/1598864

Cullen, S., Perelstein, M., and Peskin, M. E., 2000, "TeV strings and collider probes of large extra dimensions", Phys. Rev. D 62**,** 055012.

Davoudiasl, H., Hewett, J. L., and Rizzo, T. G., 2000, "Phenomenology of the randallsundrum gauge hierarchy model", ***Phys. Rev. Lett.***, vol. 84, pp. 2080–2083, Mar.

Dokshitzer, Y. L., Leder, G., Moretti, S. and Webber, B. R., 1997, "Better jet clustering algorithms", Journal of High Energy Physics, Vol. 1997, No. 08, pp. 001.

D'Imperio, G., 2016, "Search for narrow resonances in dijet final states at the LHC with $\sqrt{s}$= 13 TeV", CERN-THESIS-2016-182.

Duarte, J., 2017, "Naturalness confronts nature: searches for supersymmetry with the CMS detector in pp collisions at √s=8 and 13 TeV", Thesis ORCID: 0000-0002-5076-7096

Eichten, E., Hinchliffe, I., Lane, K., and Quigg, C., 1984, "Supercollider physics", ***Rev. Mod. Phys.***, vol. 56, pp. 579–707, Oct.

Ellis, R. K., 1996, "QCD and Collider Physics" Cambridge University Press.

Ellis, S. D., and Soper, E. D., 1993, "Successive combination jet algorithm for hadron collisions", Physical Review D, Vol. 48, No.7, pp. 3160-3166.

Evans, L., and Bryant, P., 2008, "LHC Machine". In: Journal of Instrumentation 3.08, S08001. URL: http://stacks.iop.org/1748-0221/3/i=08/a=S08001.

Paola, F., and Rodrigo, G., 2009, "Constraining Heavy Colored Resonances from

Top- Antitop Quark Events”, *Physical Review D - Particles, Fields, Gravitation and Cosmology* 80(5).

Francisco, O. N., 2007, “Inclusive Jet Production Studies at the Tevatron using CDF Detector”, FERMILAB-THESIS-2007-08.

Frampton, P. H., and Glashow, S. L., 1987, “Chiral color: An alternative to the standard model”, Phys. Lett. B 190 157.

Gouzevitch, M., et al., 2011 “Search for Heavy Particles Decaying to Hadronic Final States with FatJetReconstruction”, CMS AN 2011/242.

Gouzevitch, M., Santanastasio, F. et al., 2012, “Search for Narrow Resonances using the Dijet Mass Spectrum in pp Collisions at $\sqrt{s}$ = 7 TeV”, CMS AN 2012/012.

Green, M. B., Schwarz, J. H., and Witten, E., 1987, “Superstring” Theory (Cambridge University Press, Cambridge, England).

Guichardant C., et al., 2012, “Significance estimation for the dijet resonance search using 8 TeV pp collision data”, CMS AN 2012/325.

Halzen, F., Martin, D., 1984, “Quarks and Leptons: An Introductory Course in Modern Particle Physics”. John Wiley & Sons, Inc.

Han, T., Lewis, I., and Liu, Z., 2010, “Colored resonant signals at the lhc: largest rate and simplest topology”, JHEP 12**,** 085.

Harris, R.M., et al., 2007, “Plans for Jet Energy Corrections at CMS”, The CMS Collaboration CMS-PAS-JME-07-002.

Harris, R. M., and Kousouris, K., 2011. “Searches for Dijet Resonances at Hadron Colliders”http://arxiv.org/abs/1110.5302%0Ahttp://dx.doi.org/10.1142/S0217751X11054905.

Hewett, J., Anne L., and Rizzo, T. G., 1989. “Low-Energy Phenomenology of Superstring- Inspired E6 Models” *Physics Reports* 183(5–6): 193–381.

Hinchliffe, I., and Manohar, A. V., 2000, “The QCD Coupling Constant” *Annual Review of Nuclear and Particle Science* 50: 56.

Isildak, B., Santanastasio, F., Pierini, M., and Ozturk, S., 2015, “Search for dijet resonances at $\sqrt{s}$ = 8 TeV with data scouting”, CMS Analysis Note AN-14-104.

Katsilieris, G., Korakianitis, O., and Vlassopulos, S.D.P., 1992, “Two-jet rates affected by exotic particles at hadron colliders”, Physics Letters B, Volume 288, Issues 1-2, Pages 221-226

Khachatryan V., *et al.*, 2010, “Search for Dijet Resonances in 7 TeV pp Collisions at CMS,” *Phys. Rev. Lett.*, vol. 105, p. 211801.

Khachatryan V., *et al.*, 2015, “Search for resonances and quantum black holes using dijet mass spectra in proton-proton collisions at $\sqrt{s}$ = 8 TeV,” *Phys. Rev. D*, vol. 91, p. 052009.

Kirschenmann, H., 2010, “Exploitation of Jet Properties for Energy Scale Corrections for the CMS Calorimeters”, DESY-THESIS-2011-006, CERN-THESIS-2010-293 CMS-TS-2011-002.

Lazaridis, C., 2011, “Jets Produced in Association with z Bosons in CMS at the LHC”, CERN-THESIS-2011-105, CMS-TS-2011-044.

Martelli, A., 2012, “First Measurement of the WZ Production cross section with the CMS Detector at the LHC”, CERN-THESIS-2012-014.

Moortgat, F., 2004 “Discovery potential of MSSM Higgs bosons using supersymmetric decay with the CMS detector, Antwerpen”

Narrison, S., 2004, “QCD as a Theory of Hadrons: From Partons to Confinement,” Cambridge University Press.

Nikitenko, A., et al., 2009, “The Jet Plus Tracks Algorithm”, The CMS Collaboration CMS-PAS-JME-09-002

Ozturk, S., 2011, “Search for new particles decaying to dijet in 7 TeV proton-proton collisions at CMS”, CERN-THESIS-2011-007

Pati, J. C., and Salam, A., 1985, Phys. Lett. B 58, 333 (1975). Hall L. J. and Nelson, A. E., Phys. Lett. B 153, 430.

Petrukhin, A., 2010, “Structure Function Measurements at HERA”, arXiv-hepex: 1005.5612v1.

Pumplin, J., et al., 2002, “New generation of parton distributions with uncertainties from global QCD analysis”, JHEP **07,** 012, arXiv:hep-ph/0201195.

Randall, L., and Sundrum, R., 1999a, “A Large mass hierarchy from a small extra dimension”, *Phys. Rev. Lett.*, vol. 83, no. MIT-CTP-2860, PUPT-1860, BUHEP-99-9, pp. 3370–3373.

Randall, L., and Sundrum, R., 1999b, “An alternative to compactification”, *Phys. Rev. Lett.*, vol. 83, pp. 4690–4693, Dec.

Salam, G.P., et al., 2006, “Dispelling N^3 the Myth for the k_T Jet Finder”Phys.Lett.B641:57-61.

Salam, G.P., et al., 2007, “A Practical Seedless Infrared Safe Cone jet Algorithm”, arXiv-hepph: 0705.2696v1.

Salam, G.P., et al., 2010, “Towards Jetography”, arXiv-hep-ph:0906.1833.

Salam, G.P., et al., 2011, “Elements for QCD for hadron colliders”, CERN Yellow Report CERN-2010-002, pp 45-100.

Scheurer, A., 2008, “Algorithms for the identification of b- Quarks Jets with First Data at CMS”, CERN-THESIS-2008-133, CMS-TS-2008-019.

Schieferdecker, P., 2008, “Performance of Jet Algorithms in CMS”, The CMS Collaboration CMS-PAS-JME-07-003.

Simmons, E. H., 1997, Phys. Rev. D 55, 1678.

Sjostrand, T., Mrenna S., and Skands, P. Z., 2008, “A Brief Introduction to PYTHIA 8.1” *Comput. Phys. Commun.*, vol. 178, pp. 852–867.

Smith, W., 2008, Hadron Collider Physics Summer School at Fermilab, August 12-22.

Sterman, G., Brook, S., and York, N., 2005, “The Background of QCD.” 3: 1–23.

The CMS Collaboration, 1997a, “The Compact Muon Solenoid. Muon technical design report CMS”.

The CMS Collaboration, 1997b, “*The CMS electromagnetic calorimeter project:*

Technical Design Report CMS", Geneva, CERN.

The CMS Collaboration, 2009, "Particle-Flow Event Reconstruction in CMS and Performance for Jets, Taus, and MET" Tech. Rep. CMS-PAS-PFT-09-001, CERN, 2009. Geneva, Apr.

The CMS Collaboration, 2011, "Determination of jet energy calibration and transverse momentum resolution in CMS" Journal of Instrumentation 6 (November, 2011) 11002.

The CMS Collaboration, 2017, "Jet energy scale and resolution in the CMS experiment in pp collisions at 8 TeV," arXiv:1607.03663v2 [hep-ex] 26 Feb 2017

Zielinski, M., et al., 2010, "Jet Performance in *pp* Collisions at 7 TeV" CMS-PAS-JME-10-003.

https://github.com/miquork/dijet/tree/april29-refit

http://cerncourier.com/cws/article/cern/29723

https://twiki.cern.ch/twiki/bin/viewauth/CMS/JetID#Recommendations_for_13_TeV_data

https://cms-service-dqm.web.cern.ch/cms-service-dqm/CAF/certification/Collisions15/13TeV/Cert_246908-260627_13TeV_PromptReco_Collisions15_25ns_JSON_Silver.txt

CURRICULUM VITAE

Serdal DAMARSEÇKİN was born in 1982 in Van, Turkey. He graduated from high school in Van, 1998. He graduated from Physics Department at Yüzüncü Yıl University by receiving 2nd ranked in his department in 2003. He graduated from M.Sc. in Physics Department at Yüzüncü Yıl University in 2009. He started his Ph.D. education at Çukurova University in 2011. At the same time, he joined CMS experiments to pursue his Ph.D. dissertation research at CERN in Geneva, Switzerland. He has studied in several research projects supported by Turkey Atomic Energy Agency. He has been worked at Çukurova University as a Research Assistant between 2013 and 2017. He has been working at Şırnak University as a Research Assistant since 2017. He is married and has two daughters.

APPENDICES

APPENDIX A

Dijet Mass Binning

During run 1, in all previous dijet searches and at 8 TeV dijet SMP measurements, the following dijet mass binning is used;

const int nMassBins = 103;

double massBoundaries[nMassBins+1] = {1, 3, 6, 10, 16, 23, 31, 40, 50, 61, 74, 88, 103, 119, 137, 156, 176, 197, 220, 244, 270, 296, 325, 354, 386, 419, 453, 489, 526, 565, 606, 649, 693, 740, 788, 838, 890, 944, 1000, 1058, 1118, 1181, 1246, 1313, 1383, 1455, 1530, 1607, 1687, 1770, 1856, 1945, 2037, 2132, 2231, 2332, 2438, 2546, 2659, 2775, 2895, 3019, 3147, 3279, 3416, 3558, 3704, 3854, 4010, 4171, 4337, 4509, 4686, 4869, 5058, 5253, 5455, 5663, 5877, 6099, 6328, 6564, 6808, 7060, 7320, 7589, 7866, 8152, 8447, 8752, 9067, 9391, 9726, 10072, 10430, 10798, 11179, 11571, 11977, 12395, 12827, 13272, 13732, 14000};

APPENDIX B

Fit Studies

In Fig B.1, it is shown the variation of the blinded simultaneous fit and blinded separate fit for the mass and trigger efficiency relative to the unblinded simultaneous fit. The fit parameters are given in Table B.1.

Table B.1. Parameters of fits in Fig. B.1.

Fit	m_{eff}	σ_{eff}	p_0	p_1	p_2	p_3
Unblinded simultaneous fit	495.5	93.73	1.0727X10^{-7}	3.1932	8.0554	0.494224
Blinded simultaneous fit	495.8	92.4	3.7406X10^{-7}	5.2043	7.3825	0.397342
Blinded separate fit	495.7	96.0	6.0217X10^{-7}	5.8587	7.0764	0.3480

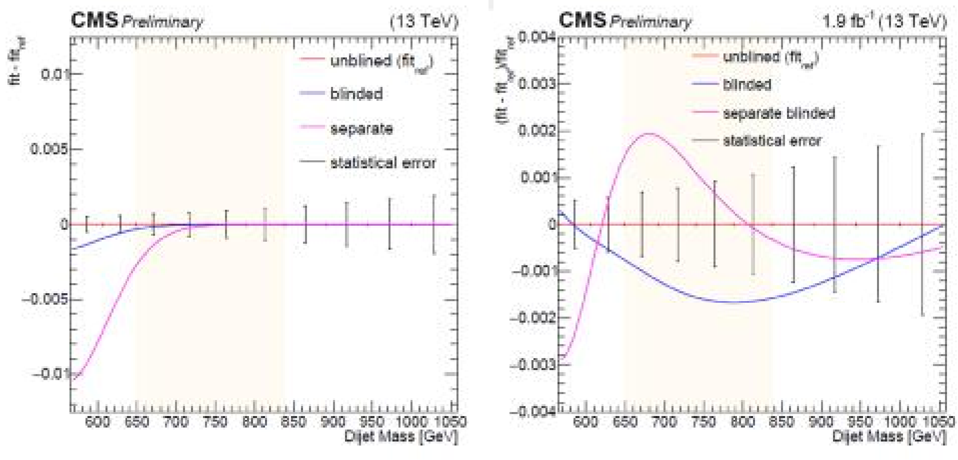

Figure B.1. Variation between unblinded simultaneous fit, blinded simultaneous fit, and blinded separate fit for the trigger efficiency (left) and mass spectrum (right). The shaded region was blinded in the mass spectrum for the blinded fits. The errors are the relative statistical errors from the mass spectrum data.

Fig. B.2 shows a simultaneous fit for the mass spectrum and trigger efficiency similar to that in Sec. 3.1.2 but using a likelihood fit.

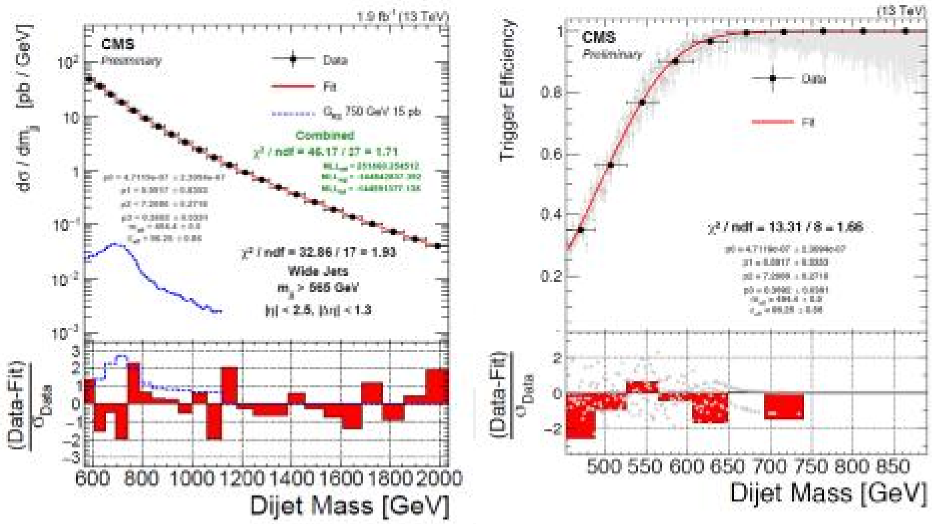

Figure B.2. Simultaneous likelihood fit for trigger efficiency (left) and mass spectrum (right).

APPENDIX C

Impact of Systematic Uncertainties on the Limits

We discuss the impact of systematic uncertainties on the cross section upper limits. Limit plots are shown in Fig. C.1 are the same as Fig. 3.8, without any systematic uncertainties. In Fig. C.2, ratios of the observed and expected cross section upper limits with and without the systematic uncertainties are shown. With decreasing resonance mass, the ratio for observed limits additionally susceptible to fluctuations in data increases.

In Fig. C.3 for individual sources of uncertainty limit ratios for qg resonances as well as combinations of some of them are shown for better understanding of the size of contribution from different sources of systematic uncertainties. The ratio is produced for observed limits for practical reasons where running a large number of pseudo-experiments are not necessary. It can be seen, the dominant source of systematic uncertainty is the background uncertainty. The background shape is less constrained in the signal+background fit is the fact which consequences the rising trend with decreasing resonance mass.

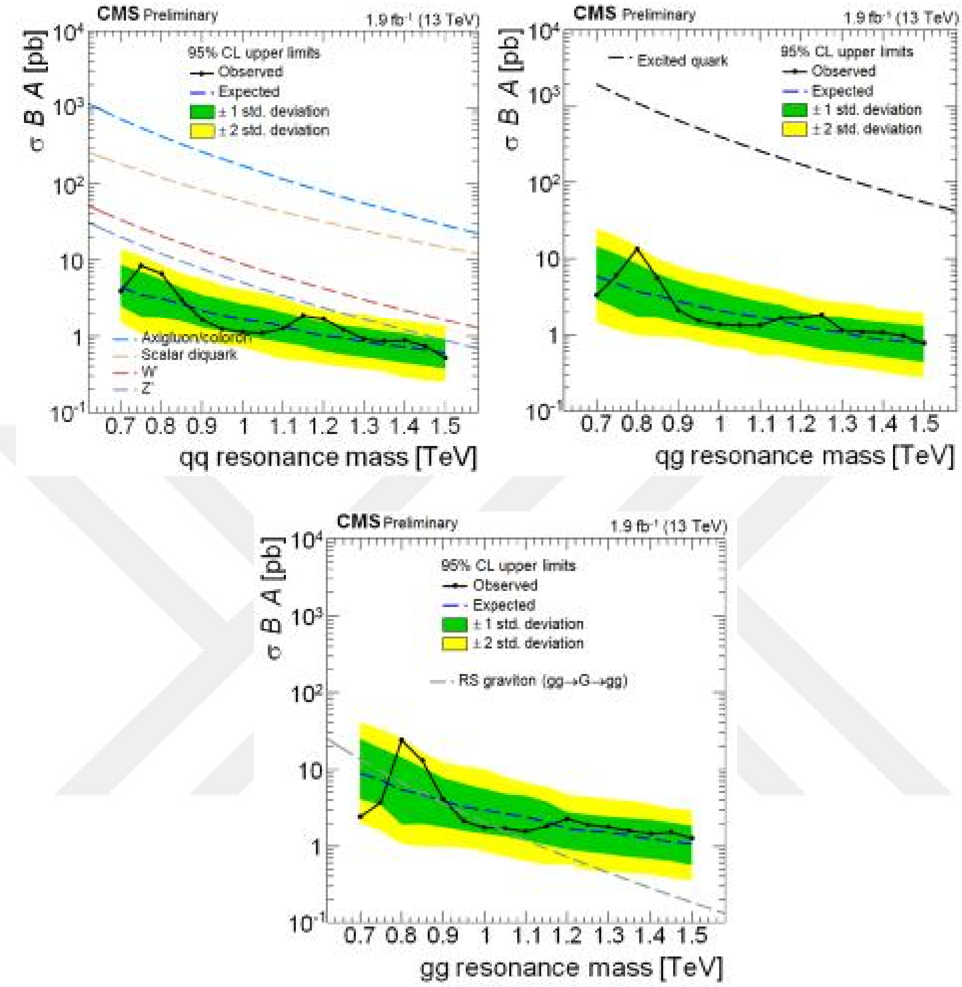

Figure C.1. The observed 95% CL upper limits on σ B A for narrow resonances decaying into qq (top left), qg (top right) and gg (bottom) final states. The limits are shown as points and solid lines. Also shown are the expected limits (dot-dashed blue lines) and their 1 and 2σ Standard deviations (shaded bands). Predicted cross sections calculated for various narrow resonances are also shown. For the limits shown here systematic uncertainties were not included in their calculation.

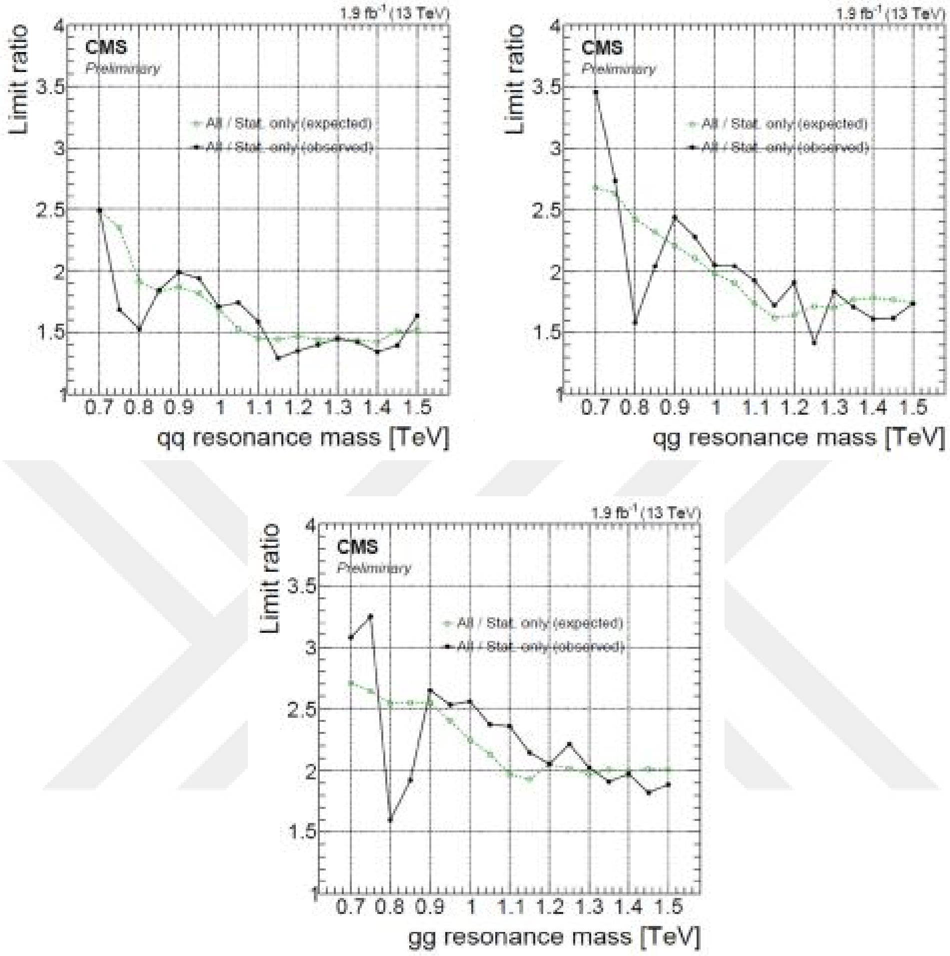

Figure C.2. Ratios of the observed and expected cross section upper limits with and without the systematic uncertainties included as a function of the resonance mass for narrow resonances decaying into qq (top left), qg (top right), and gg (bottom) final states.

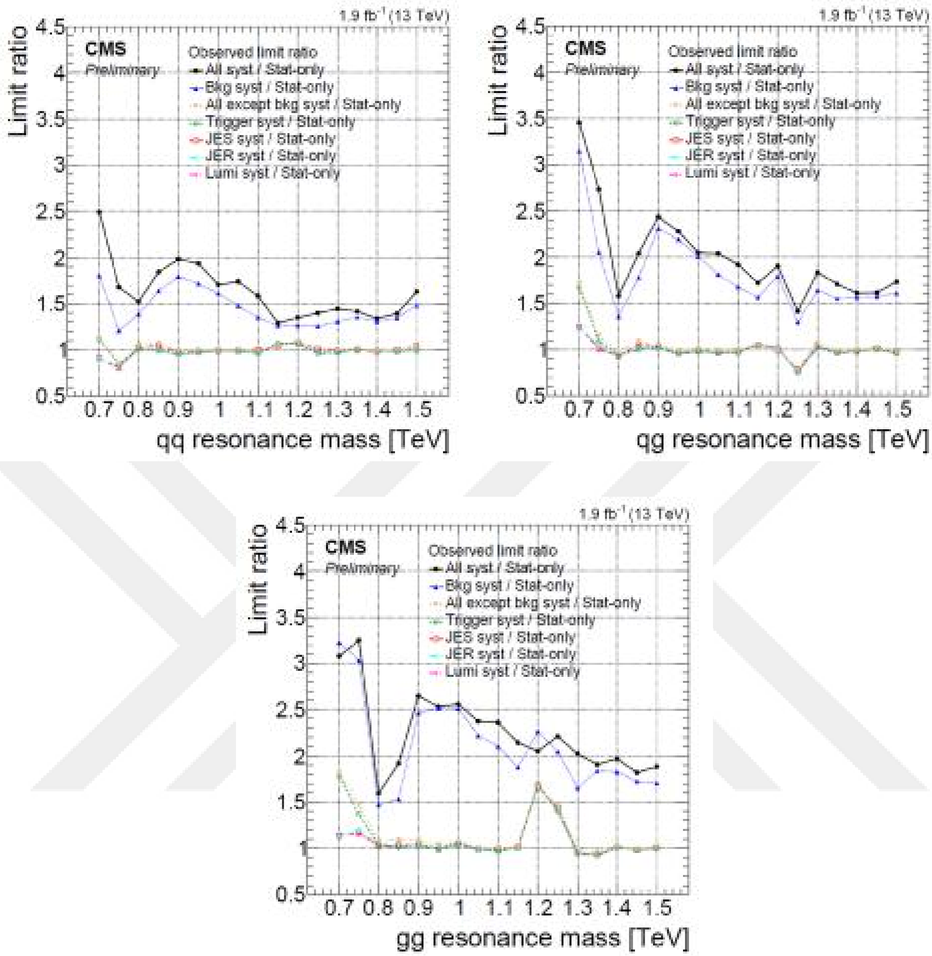

Figure C.3. Ratios of the observed cross section upper limits with and without the systematic uncertainties included for different sources of systematic uncertainties as a function of the resonance mass for narrow resonances decaying into qq (top left), qg (top right), and gg (bottom) final states.

APPENDIX D

Extracted Best-fit Signal Cross Sections

The extracted best-fit signal cross sections and associated errors for qq, qg, and gg resonances are shown in the Fig. D.1. As it shows only positive values while at a point zero negative values for extracted cross sections is plotted with the fit error, which is displayed as a one-sided error bar starting at zero and this error bar is extending to the value of the extracted signal cross section error. Table D.1 includes a full list of the extracted signal cross sections for positive, negative, and associated errors with different resonance types.

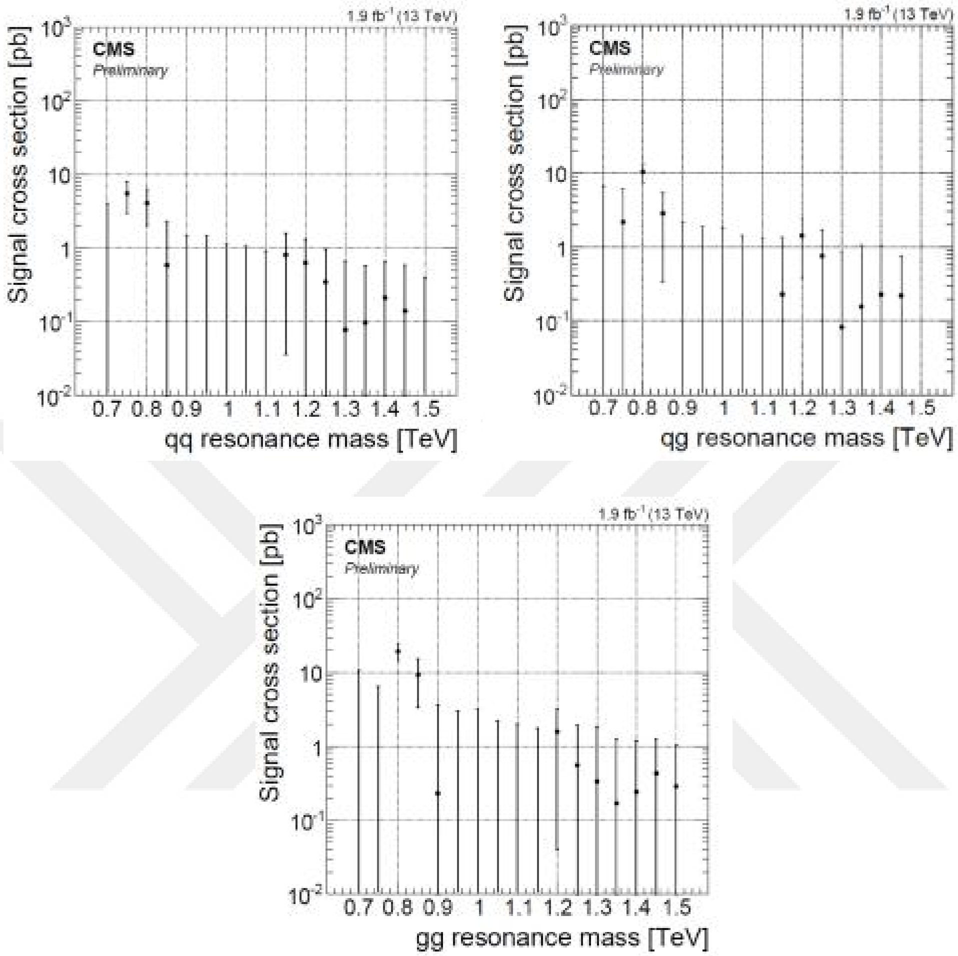

Figure D.1. Scan of the extracted best-fit signal cross sections as a function of the resonance mass for qq (top left), qg (top right), and gg (bottom) resonances.

Table D.1: Extracted best-fit signal cross sections as a function of the resonance mass for qq, qg, and gg resonances

mass [TeV]	cross section [pb]		
	qq	qg	gg
0.70	-1.019e+00±3.944e+00	-4.251e+00±6.781e+00	-1.633e+01±1.062e+01
0.75	5.522e+00±2.540e+00	2.164e+00±3.931e+00	-4.936e+00±6.514e+00
0.80	4.086e+00±2.050e+00	1.045e+01±3.042e+00	1.931e+01±4.929e+00
0.85	5.917e-01±1.721e+00	2.830e+00±2.498e+00	9.245e+00±5.884e+00
0.90	-1.222e+00±1.481e+00	-1.184e+00±2.153e+00	2.352e-01±3.461e+00
0.95	-1.464e+00±1.465e+00	-1.982e+00±1.861e+00	-2.635e+00±3.008e+00
1.00	-1.103e+00±1.126e+00	-1.564e+00±1.787e+00	-2.674e+00±3.181e+00
1.05	-7.761e-01±1.068e+00	-1.143e+00±1.434e+00	-1.866e+00±2.234e+00
1.10	-1.965e-01±9.100e-01	-6.895e-01±1.288e+00	-1.656e+00±2.020e+00
1.15	8.148e-01±7.788e-01	2.282e-01±1.116e+00	-4.590e-01±1.785e+00
1.20	6.318e-01±6.906e-01	1.429e+00±1.051e+00	1.599e+00±1.559e+00
1.25	3.499e-01±6.196e-01	7.590e-01±9.498e-01	5.622e-01±1.383e+00
1.30	7.767e-02±5.897e-01	8.098e-02±7.693e-01	3.372e-01±1.527e+00
1.35	9.718e-02±4.887e-01	1.551e-01±8.924e-01	1.717e-01±1.109e+00
1.40	2.139e-01±4.360e-01	2.270e-01±8.028e-01	2.460e-01±9.691e-01
1.45	1.394e-01±4.498e-01	2.191e-01±5.348e-01	4.378e-01±8.362e-01
1.50	-1.007e-01±3.992e-01	8.827e-03±4.807e-01	2.909e-01±7.438e-01

APPENDIX E

HLT Jet Energy Resolution

Using the dijet p_T balancing, we measure jet energy resolution for HLT and RECO jets. The main variable is the asymmetry (A) between the transverse momentums of the jets defined as:

$$A = \frac{p_T^{j1} - p_T^{j2}}{p_T^{j1} + p_T^{j2}} \tag{E.1}$$

where p_T^{j1} and p_T^{j2} refers to the randomly ordered transverse momenta of the two leading jets. The variance of asymmetry can be expressed as:

$$\sigma_A^2 = \left|\frac{\partial A}{\partial p_T^{j1}}\right|^2 \sigma^2\left(p_T^{j1}\right) + \left|\frac{\partial A}{\partial p_T^{j2}}\right|^2 \sigma^2\left(p_T^{j2}\right) \tag{E.2}$$

If the two jets lie in the same η region, it will be

$< p_T^{j1} >=< p_T^{j2} >\equiv p_T$ and $\sigma(p_T^{j1}) = s(p_T^{j2})\equiv\sigma(p_T)$

The jet p_T resolution therefore is related to the width of asymmetry by the Eq. (E.3).

$$\frac{\sigma(p_T)}{p_T} = \sqrt{2}\sigma(A) \tag{E.3}$$

The asymmetry is calculate in bins of $|\eta|$ and average p_T defined as:

$$p_{Tave} = \frac{p_T^{j1} + p_T^{j2}}{2} \tag{E.4}$$

An approximation of the true resolution in the case of no extra jet activity in the event that modifies the p_T balance of the two leading jets is shown in the Eq. (E.3). With the additional request of a third possible jet with small transverse momentum with respect to the average p_T ($p_T^{j3} < 0.1\, p_{Tave}$) the asymmetry has been calculated.

This method has been applied to the RECO jets and to the HLT ones in order to compare their resolutions.Two examples of the asymmetry variable are shown in Fig. E.1.

These distributions have been fitted with a function composed by a Gaussian core and two exponential tails. For each bin of |η| and average p_T, the variance of the asymmetry has been extracted from the fits. For the first η bin, the width of the asymmetry in function of the average transverse momentum is reported as an example in Fig. E.2. The HLT jets have comparable p_T resolution to the RECO jets.

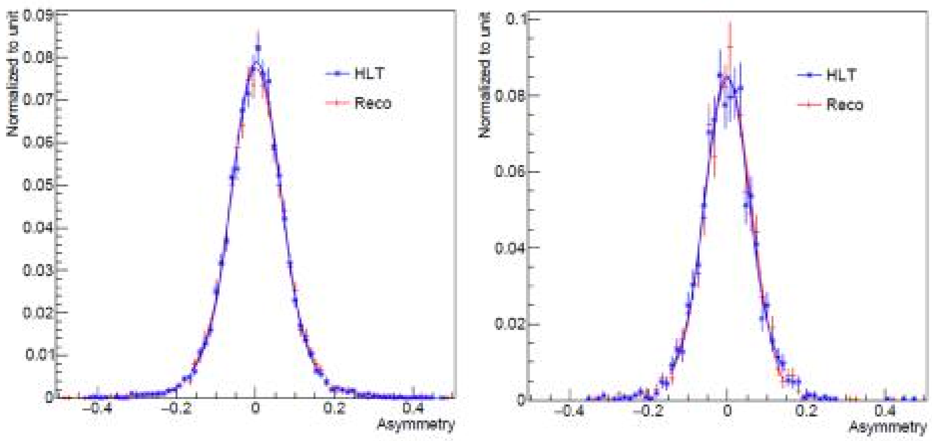

Figure E.1. The asymmetry of RECO jets (in red) and HLT jets (in blue). The distributions refer to the same central region |η| < 0.5 but to different p_T bins: on the left $300 < p_T < 400$ GeV and on the right $400 < p_T < 500$ GeV

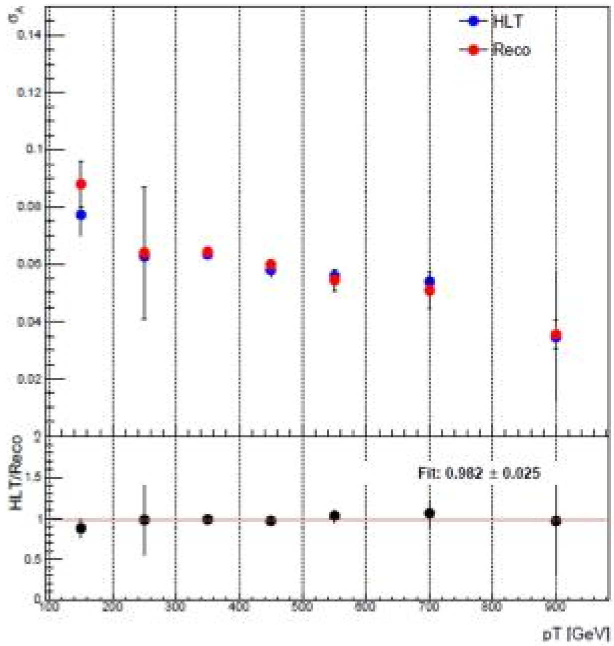

Figure E.2. The asymmetry for the RECO jets (in red) and for the HLT jets (in blue) in function of the average transverse momentum for the central η bin. On the bottom panel is reported the ratio between HLT and RECO which shows that the HLT jets have the same p_T resolution than RECO jets.